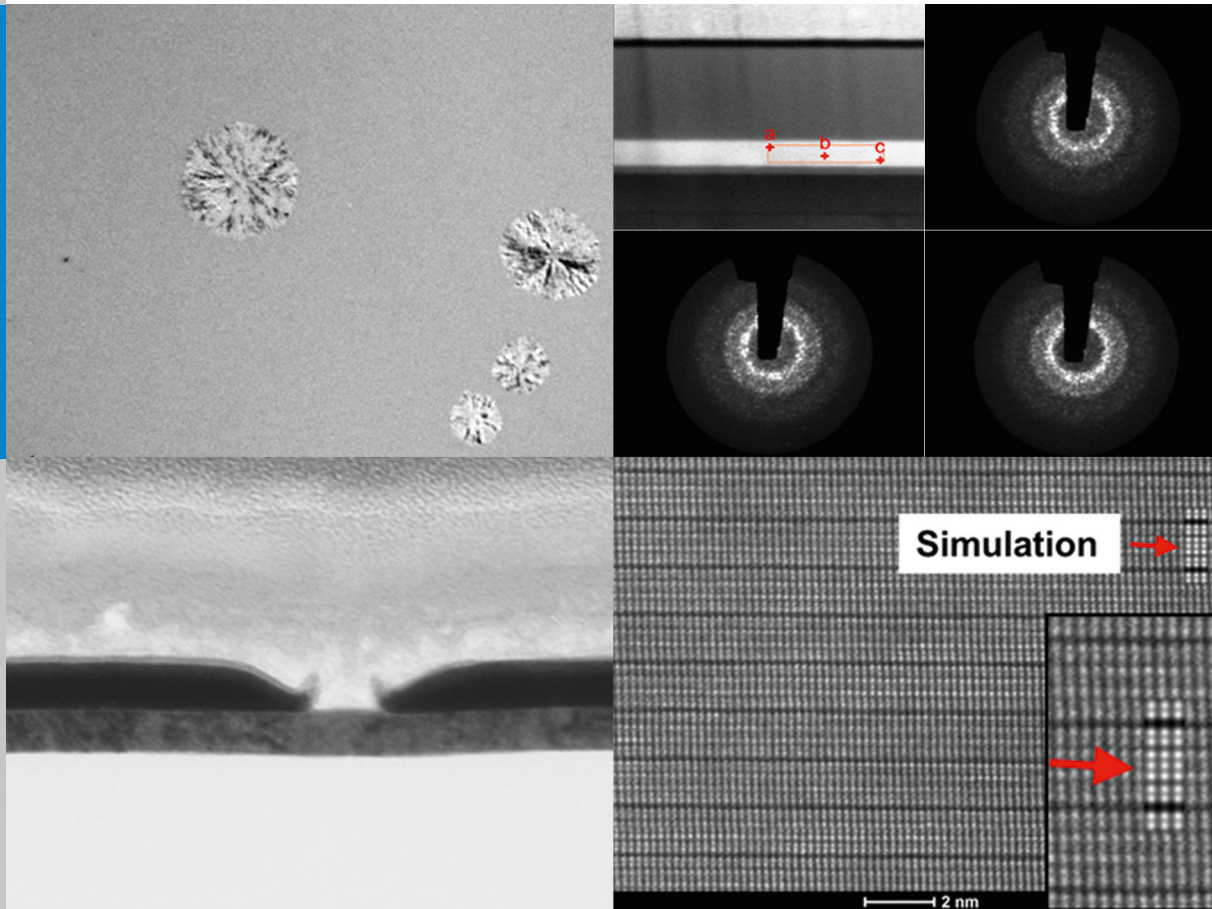


TEM/STEM Investigations of Phase Change Materials for Non-volatile Memory Applications

Manuel Bornhöfft



Information
Band/ Volume 47
ISBN 978-3-95806-221-4

Forschungszentrum Jülich GmbH
Peter Grünberg Institute (PGI)
Microstructure Research (PGI-5)

TEM/STEM Investigations of Phase Change Materials for Non-volatile Memory Applications

Manuel Bornhöfft

Schriften des Forschungszentrums Jülich
Reihe Information / Information

Band / Volume 47

ISSN 1866-1777

ISBN 978-3-95806-221-4

Bibliographic information published by the Deutsche Nationalbibliothek.
The Deutsche Nationalbibliothek lists this publication in the Deutsche
Nationalbibliografie; detailed bibliographic data are available in the
Internet at <http://dnb.d-nb.de>.

Publisher and
Distributor: Forschungszentrum Jülich GmbH
Zentralbibliothek
52425 Jülich
Tel: +49 2461 61-5368
Fax: +49 2461 61-6103
Email: zb-publikation@fz-juelich.de
www.fz-juelich.de/zb

Cover Design: Grafische Medien, Forschungszentrum Jülich GmbH

Printer: Grafische Medien, Forschungszentrum Jülich GmbH

Copyright: Forschungszentrum Jülich 2017

Schriften des Forschungszentrums Jülich
Reihe Information / Information, Band / Volume 47

D 82 (Diss. RWTH Aachen University, 2017)

ISSN 1866-1777
ISBN 978-3-95806-221-4

Vollständig frei verfügbar über das Publikationsportal des Forschungszentrums Jülich (JuSER)
unter www.fz-juelich.de/zb/openaccess.



This is an Open Access publication distributed under the terms of the [Creative Commons Attribution License 4.0](https://creativecommons.org/licenses/by/4.0/),
which permits unrestricted use, distribution, and reproduction in any medium, provided the original work is properly cited.

Abstract

Phase change materials are very interesting for future information technology because of their possibility to encode information in the readable difference of physical properties between the crystalline and the amorphous phase. Phase change materials are the dominant non-volatile memory material used in rewritable optical memory. This includes the current state of the art Blue-ray disc. Mobile computer platforms like smart mobile phones, tablets and netbooks are in need of energy and space efficient memory. Optical or magnetic recording media do not meet these needs anymore. Phase change materials used as non-volatile electronic memories are promising candidates as competition for flash memory. Flash memory is the current state of the art electronic non-volatile memory. In addition, non-volatile electronic applications as competition to Dynamic Random Access Memory (DRAM) are possible because of the high switching speeds of phase change materials. The key to the successful application of phase change materials as electronic non-volatile memory is the understanding of their physical properties and especially their switching kinetics. In the present work, transmission electron microscopy (TEM) and scanning transmission electron microscopy (STEM) were used in a systematic manner to investigate the properties of a variety of phase change materials.

The crystal growth velocities of grains growing in 30 nm thick amorphous layers of the phase change materials $\text{Ag}_4\text{In}_3\text{Sb}_{67}\text{Te}_{26}$ (AIST) and GeTe were measured directly by TEM bright field imaging. Grains of the measured materials were grown in a matrix of the amorphous phase by ex situ heating. This is done for sputtered as deposited material and material molten by laser which is quenched to room temperature. Furthermore we investigated lamellas of as deposited and melt quenched AIST and GeTe by fluctuation electron microscopy (FEM). The comparison of growth velocity and FEM data reveals that increasing medium range order (MRO) leads to a decrease in growth velocity. This is also related to different glassy states of the phase change materials.

The switching behaviour of electronic phase change material memory devices based on the material AIST was investigated by TEM bright field imaging. Cross section lamellas were prepared by a combined focused ion beam and scanning electron microscope procedure. The investigation of the amorphous state of a switched device showed the occurrence of the Thompson-Seebeck effect, leading to an

inhomogeneous heat distribution and an inhomogeneous amorphization of the phase change material device.

In further studies, the intermediates of the reaction path of a solvothermal synthesis of single crystalline hexagonal Sb_2Te_3 platelets were investigated. The chosen methods were STEM annular dark field (ADF) imaging and nano area electron diffraction (NAED). These platelets can be used as a model system for phase change materials. NAED has revealed surprising results on the structure and shape of the intermediate states during synthesis.

The stable phases of the Ge, Sb and Te (GST) alloys have highly ordered layered structures similar to the structures of interfacial phase change materials (IPCM) but without an artificial super lattice design. Therefore the stable phases of GST are very interesting materials to understand the switching processes of IPCM or phase change materials of similar structure. $\text{Ge}_1\text{Sb}_2\text{Te}_4$ (GST 124) in the stable phase was directly deposited on a Si (111) substrate by metal organic vapor phase epitaxy (MOVPE). In the present work GST 124 deposited by MOVPE was investigated by TEM and high resolution STEM (HRSTEM). The atomic structure of GST 124 in the stable phase was resolved and the high quality of the MOVPE deposited layers was demonstrated. Furthermore the adaption zone of the GST 124 to grow perfectly on the Si (111) substrate is imaged with atomic resolution.

Kurzfassung

Phasenwechselmaterialien sind aufgrund der Möglichkeit, Informationen in auslesbaren Unterschieden zwischen der amorphen Phase und der kristallinen Phase zu speichern, von großem Interesse für die zukünftige Informationstechnologie. Phasenwechselmaterialien haben den größten Anteil am Erfolg wiederbeschreibbarer optischer Speichermedien, von denen heute die Blu-ray disc den Stand der Technik darstellt. Mobile Computerplattformen wie Smartphones, Tablets und Netbooks brauchen energie- und platzsparende Speicherlösungen. Optische oder magnetische Speichermedien entsprechen nicht mehr diesen Anforderungen. Phasenwechselmaterialien, in Form elektronischer nicht flüchtiger Speicher, stellen vielversprechende Kandidaten als Konkurrenz zu etablierten elektronischen nicht flüchtigen Flash-Speichern dar. Die hohen möglichen Schaltgeschwindigkeiten, die mit Phasenwechselmaterialien erreichbar sind, machen diese sogar als nicht flüchtige Speicher Konkurrenz zu Dynamic-Random-Access-Memory (DRAM) interessant. Der Schlüssel zur erfolgreichen Etablierung von Phasenwechselmaterialien als elektronische nicht flüchtige Speicher liegt im Verständnis ihrer physikalischen Eigenschaften und im ins Besonderen im Verständnis der Schaltkinetik. In dieser Arbeit werden Transmissionselektronenmikroskopie- (TEM) und Rastertransmissionselektronenmikroskopie- (STEM) Methoden genutzt, um die Eigenschaften von Phasenwechselmaterialien systematisch zu untersuchen.

Die Kristallwachstumsgeschwindigkeiten von wachsenden Körnern in 30 nm dicken amorphen Dünnschichten der Phasenwechselmaterialien $\text{Ag}_4\text{In}_3\text{Sb}_{67}\text{Te}_{26}$ (AIST) und GeTe wurden durch direktes Abbilden im TEM Hellfeld bestimmt. Hierfür wurden Körner durch ex situ-Heizen in einer amorphen Matrix gewachsen. Als Ausgangslage wurden der amorphe Zustand nach dem Abscheiden mittels Sputtern und der amorphe, auf Raumtemperatur abgeschreckte, Zustand aus der Schmelze gewählt. Es wurde weiterführend Fluktuationselektronenmikroskopie (FEM) an abgeschiedenen und abgeschreckten TEM-Lamellen beider Phasenwechselmaterialien durchgeführt. Ein Zusammenhang zwischen ansteigender mittlerer Reichweitenordnung (MRO) und abnehmender Wachstumsgeschwindigkeit konnte gefunden werden. Dies konnte außerdem mit verschiedenen Glaszuständen in Verbindung gebracht werden.

Das Schaltverhalten von elektronischen Phasenwechselmaterialspeicherzellen aus dem Phasenwechselmaterial AIST wurde mittels TEM-Hellfeld untersucht. Querschnitts-TEM-Lamellen dieser vertikalen Phasenwechselmaterial-Linien-Zellen wurden mit Hilfe des kombinierten Geräteaufbaus eines fokussierten Ionenstrahls (FIB) und eines Rasterelektronenmikroskops (SEM) präpariert. Die Untersuchung der geschalteten Linien-Zellen zeigt den Einfluss des Thompson-Seebeck-Effekts auf das Schalten, welcher zu einer inhomogenen Wärmeverteilung und inhomogener Amorphisierung der Phasenwechselmaterialspeicherzelle führt.

In weiterführenden Untersuchungen wurden die Zwischenstufen des Reaktionswegs einer Solvothermalsynthese zur Erzeugung einkristalliner hexagonaler Sb_2Te_3 -Plättchen im STEM-Dunkelfeld mit einem Ringdetektor abgebildet und mit Nanobereichselektronenbeugung (NAED) untersucht. Die hexagonalen Plättchen können als Modellsysteme für Phasenwechselmaterialien dienen. Die Untersuchung der Reaktionszwischenstufen mittels NAED hat interessante Ergebnisse über die Struktur und Form der Zwischenstufen der Synthese hervorgebracht.

Die stabilen Phasen von Ge, Sb und Te (GST)-Legierungen sind hoch geordnete Lagenstrukturen. Diese sind sehr ähnlich zu den Strukturen von Interface-Phasenwechselmaterialien (IPCM), allerdings ohne eine künstlich erzeugte Überstruktur. Daher sind die stabilen Phasen von GST von großem Interesse, um das Schaltverhalten von IPCM oder ähnlich strukturierten Phasenwechselmaterialien zu verstehen. $\text{Ge}_1\text{Sb}_2\text{Te}_4$ (GST 124) in der stabilen Phase wurde auf einem Si (111)-Substrat mittels metallorganischer Gasphasenepitaxie (MOVPE) abgeschieden. Die Schicht wurde mittels TEM und hochaufgelöstem STEM (HRSTEM) untersucht. Die atomare Struktur der stabilen GST 124 Phase wurde abgebildet und eine hohe Güte der mit MOVPE abgeschiedenen Schichten demonstriert. Weiterführend konnte die Region in atomarer Auflösung abgebildet werden, die die GST-124-Schichten benötigen, um das Schichtwachstum an das Si (111)-Substrat anzupassen.

Acknowledgements

This thesis would not have been possible without the tremendous support of my colleagues in the GFE, ER-C and in the SFB 917. Therefore this chapter is devoted to the acknowledgement of these wonderful people.

First of all, I would like to thank my supervisor, Prof. Joachim Mayer. Prof. Mayer always trusted in my abilities to organize my own research, while he always supported me, when I was in need of guidance. In my opinion it is one of the greatest values to be independent as a scientist and as a professional. Furthermore, I was always astonished by the experience and knowledge of Prof. Mayer and that he always was willing to share his wisdom with me.

Secondly, I would like to thank Prof. Matthias Wuttig for giving me the opportunity to use his facilities and resources. The shared work on several topics resulted in a wonderful cooperation between me and his staff. The students of Prof. Wuttig were my closest project partners and I always felt very welcome and accepted on any visit in his institute.

I also would like to thank all the principal investigators of the SFB 917 for their fruitful cooperation. My special gratitude goes to Prof. Regina Dittmann, Dr. Hilde Hardtdegen, Prof. Ulrich Simon and Prof. Thomas Taubner. Together we tackled many questions and I hope I could help to answer some of them. I also want to thank Prof. Carsten Honerkamp for being my fourth examiner in the defence of my thesis.

I am very grateful for my project partners in the SFB 917, who were great colleagues and great people. Without their cooperation and work this thesis would not have been possible. Special thanks go to J. Benke, J. Pries, S. Riess and T. Saltzmann. Our shared challenges led to the results of most parts of this thesis. I could not have been happier with the outcomes and that I have met you.

I also would like to thank all the people working in the ER-C, who provided guidance and help, when I was using their impressive collection of state of the art transmission electron microscopes.

I cannot thank enough all colleagues in the GFE. Their help was tremendous and more importantly they also made working in the GFE worthwhile. In M. Müller und T. Caumanns I found two office mates to disguise work as fun and producing successful results at the same time. H. Du supported me in my HRSTEM investigations. R.

Iskandar, K. Ran and N. Wirch calmly endured even loud office chaos with a warm smile, were always extremely kind, helpful and open to any scientific discussion. C. Herwartz and G. Nitzinger supported my preparation of TEM specimens and kept me entertained in countless hours of dimple grinding. S. Zischke was my contact for any challenge our TEM encountered. M. Keil, U. Godzinski and R. Harscheidt helped me with all my laboratory needs. M. Spähn has provided tools and has fixed anything that was broken. F. Mariano conducted additional SEM investigations of the iron particle contaminations. I could go on forever thanking all the other great people in the GFE. Thank you for the great time!

I also want to acknowledge the funding of this thesis by the collaborative research centre “Nanoswitches” (SFB 917) by the German Science Foundation (DFG).

Contents

| | |
|-------------------------------------------------------------------------------------------------|----|
| 1 Introduction | 3 |
| 2 Main objectives of this thesis | 11 |
| 2.1 Crystallization kinetics of AIST and GeTe thin films | 11 |
| 2.2 TEM investigations of AIST line-cell cross sections | 12 |
| 2.3 Nano area diffraction of Sb_2Te_3 platelet intermediates | 12 |
| 2.4 TEM/STEM investigations of a $\text{Ge}_1\text{Sb}_2\text{Te}_4$ layer grown by MOVPE | 12 |
| 3 Crystallization kinetics of phase change materials | 13 |
| 3.1 Nucleation | 17 |
| 3.1.1 Homogeneous crystal nucleation | 17 |
| 3.1.2 Heterogeneous crystal nucleation | 22 |
| 3.2 Growth | 24 |
| 3.3 The role of the amorphous phase in phase change materials | 25 |
| 4 Electrically switched phase change devices | 29 |
| 5 Interfacial phase change materials | 32 |
| 6 Experimental | 33 |
| 6.1 Electron microscopy | 33 |
| 6.1.1 Electron interaction with matter | 36 |
| 6.1.2 Scanning electron microscopes | 38 |
| 6.1.3 Focused ion beam and dual-beam FIB | 40 |
| 6.1.4 Transmission electron microscopes | 43 |
| 6.1.4.1 TEM bright field imaging | 45 |
| 6.1.4.2 High resolution transmission electron microscopy | 47 |
| 6.1.5 Scanning transmission electron microscopes | 48 |
| 6.1.5.1 STEM annular dark field imaging | 50 |
| 6.1.5.2 Nano area electron diffraction in STEM | 51 |
| 6.1.5.3 Fluctuation electron microscopy in STEM | 56 |
| 6.2 Energy filtering to improve image quality in TEM and NAED | 62 |
| 6.3 Sample and TEM specimen preparation | 63 |
| 6.3.1 Phase change material multilayer stack sputter deposition on silicon substrate | 64 |
| 6.3.2 AIST line cell on silicon substrate | 65 |
| 6.3.3 Wet solvothermal synthesis of Sb_2Te_3 hexagon platelets | 65 |
| 6.3.4 MOVPE of GST 124 on silicon substrate | 66 |
| 6.3.5 Plan view TEM specimen preparation | 66 |

| | |
|-------------------------------------------------------------------------------------------|-----|
| 6.3.6 Ex situ heating of plan view TEM window specimens..... | 69 |
| 6.3.7 Cross section TEM lamella preparation..... | 70 |
| 7 Results..... | 74 |
| 7.1 Crystallization kinetics of AIST and GeTe thin films | 74 |
| 7.1.1 TEM measurements of grain growth velocities of AIST and GeTe | 74 |
| 7.1.1.1 Growth velocities of as deposited AIST | 76 |
| 7.1.1.2 Growth velocities of melt quenched AIST | 78 |
| 7.1.1.3 Growth velocities of as deposited AIST and melt quenched AIST in comparison | 80 |
| 7.1.1.4 Growth velocities of as deposited GeTe | 80 |
| 7.1.1.5 Growth velocities of melt quenched GeTe | 82 |
| 7.1.1.6 Growth velocities of as deposited GeTe and melt quenched GeTe in comparison | 84 |
| 7.1.2 FEM of phase change thin film cross sections | 85 |
| 7.1.2.1 FEM of AIST cross sections..... | 86 |
| 7.1.2.2 FEM of GeTe cross sections..... | 88 |
| 7.2 TEM investigations of AIST line-cell cross sections | 90 |
| 7.3 Nano area electron diffraction of Sb_2Te_3 platelet intermediates | 94 |
| 7.4 TEM/STEM investigations of a $Ge_1Sb_2Te_4$ layer grown by MOVPE..... | 99 |
| 7.4.1 TEM investigations of a $Ge_1Sb_2Te_4$ layer | 100 |
| 7.4.2 HAADF HRSTEM investigations of a $Ge_1Sb_2Te_4$ layer..... | 102 |
| 8 Discussion | 106 |
| 8.1 Crystallization kinetics of AIST and GeTe thin films | 106 |
| 8.2 TEM investigations of AIST line-cell cross sections | 115 |
| 8.3 Nano area electron diffraction of Sb_2Te_3 platelet intermediates | 116 |
| 8.4 TEM/STEM investigations of a $Ge_1Sb_2Te_4$ layer grown by MOVPE..... | 119 |
| 9 Outlook | 123 |
| 10 List of abbreviations..... | 125 |
| 11 Bibliography..... | 129 |

1 Introduction

Today's world relies on the capabilities of modern computer technology. Low-priced, fast and reliable memories are a main factor of modern information technology. Phase change materials are the basis of most rewritable optical memory media (Yamada, 1996; Meinders et al., 2006; Raoux et al., 2010). The applied phase change materials are chalcogenides that show a big change in resistivity and reflectivity related to their phase being switched back and forth thermally between the crystalline and the amorphous phase (Ovshinsky, 1968; Yamada, 1996; Raoux et al., 2010). This change of physical properties is used as 0 and 1 in binary code. To create the amorphous phase, the material is melted by a short high heat pulse (reset pulse) heating the material above the melting temperature T_m . The melted material is then frozen in the amorphous state by rapid cooling. Amorphous material can be crystallized by a longer heat pulse with lower power (set pulse). This pulse heats the material to a temperature between the glass transition temperature T_g and T_m . In this temperature region the material crystallizes rapidly. The thermal switching can be induced optically by laser (Feinleib et al., 1971; Yamada et al., 1987; Yamada et al., 1991) or by joule heating (Ovshinsky, 1968; Karpov & Kostylev, 2006) as shown in **Figure 1**. The readout of the saved data is realized by reading out the reflectivity or resistivity by a laser pulse or electric current too small in power to heat the phase change material above the glass transition temperature T_g . The optical switching of phase change material layers was used in all generations of rewritable optical media including the state of the art Blue-ray discs (Mijiritskii et al., 2003; Wuttig & Yamada, 2007). However optical media do not meet the need for future non-volatile memories. Optical memories are still used as data carriers for music, games, software and movies sold by retail sale (Amazon, 2016), software, which is distributed on optical media, gets less and less used. The reason is the increasing relevance of upcoming streaming and downloads on demand services (Apple, 2016; Netflix, 2016). These services are supported by the mass spread of transportable devices like smart mobile phones, tablets and netbooks. These devices are saving space and energy by abandoning magnetic and optical disc drives used in desktop computers (Gross, 2012). The most probable future of memories is electronic non-volatile memory. Phase change materials are interesting candidates to become the future main electronic non-volatile memory. Be it in the form of USB-Sticks (universal serial bus) or in the form of SSD-Drives (solid state disc). If phase change materials prove to be

fast enough, they could also lead to a complete replacement of up to date volatile dynamic random access memory (DRAM).

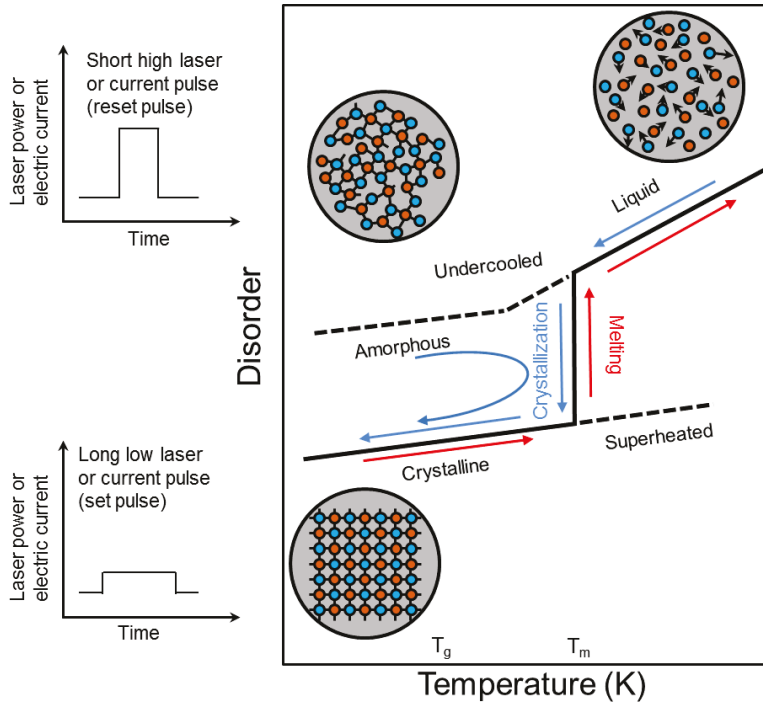


Figure 1: A phase change material is melted by a short high power laser or high electric current pulse (reset pulse; top left) which heats the phase change material above the melting temperature T_m . After the heating pulse rapid cooling freezes the phase change material in the amorphous phase. The amorphous phase change material is crystallized by a longer pulse (set pulse; bottom left). This pulse is lower in laser power or lower in electric current. The set pulse heats the phase change material to a temperature between the glass transition temperature T_g and T_m where rapid crystallization can occur (Wuttig & Yamada, 2007).

The leader in the field of electronic non-volatile memory to this date is flash memory (Bez et al., 2003; Lowe, 2015). Future phase change memories need to scale smaller and have to be more energy efficient as flash to compete as memory in the mentioned transportable computer devices. They also should be fast and reliable enough to be competitors to established volatile DRAM memory or bridge a gap between flash memory and DRAM. Also they need high scalabilities to meet even the needs of future memory demands. This would make phase change memories interesting for the industry to invest money in expensive facilities for their mass production.

Phase change materials were first mentioned by Ovshinsky in 1968, who demonstrated that switching between the phases is possible by electric current (Ovshinsky, 1968). First optical switching was demonstrated by Feinleib and co-workers in 1971 (Feinleib et al., 1971). The phase change material compositions of this time were unfortunately too slow and energy insufficient for industrial purposes as memories (Smith, 1974). The revival of phase change materials as memory came with fast switching compositions found by Yamada and co-workers in 1991 (Yamada et al., 1991). These are used in optical media including the Blue-ray disc (Mijiritskii et al., 2003). The invention of fast switching compositions also revived the research on phase change materials as electronic memory. The approach to build efficient electronic memories based on this phase change material compositions brought them back to the roots of Ovshinsky's invention. Today electronic non-volatile phase change memories are also developed and build by industry (Samsung Electronics Co. Ltd., 2006). Even after their success as optical media and after a lot of ongoing research in the field of phase change materials, there are a lot of open questions related to their properties. These questions need to be tackled to use them to full potential in electronic non-volatile memories.

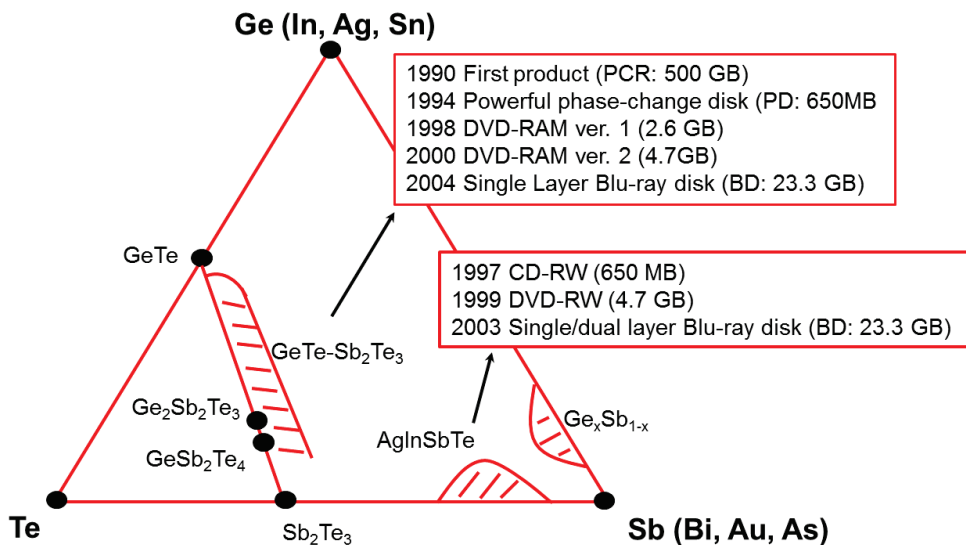


Figure 2: Shown is the ternary phase diagram of Ge, Sb and Te. The most common phase change material compositions are located in this system. Additional phase change material compositions are created by doping or by interchanging Ge or Sb by other elements. Compositions on the pseudo binary line of GeTe-Sb₂Te₃ and variations of AgInSbTe compounds are used for optical memory applications. (Wuttig & Yamada, 2007)

The compositions of the most common and investigated phase change materials are located on the pseudo binary line between GeTe and Sb_2Te_3 . Other phase change materials are located in the ternary phase diagram of Ge, Te and Sb. Doped variations or interchanging or adding of different elements substituting for Ge or Sb are also possible (Wuttig & Yamada, 2007). **Figure 2** shows the schematic ternary phase diagram. Examples of phase change material compositions and some of their applications are also shown.

Resonant bonding of the crystalline state of phase change materials is the explanation for the big change in properties between the crystalline phase and the amorphous phase and a finger print of phase change materials. Instead of building a covalent bond, in resonant bonding the valence electrons are shared between the lattice atoms (Shportko et al., 2008). The increase in delocalization of the valence electrons increases the electronic polarizability. **Figure 3** shows a simplified scheme of the resonant bonding in Sb.

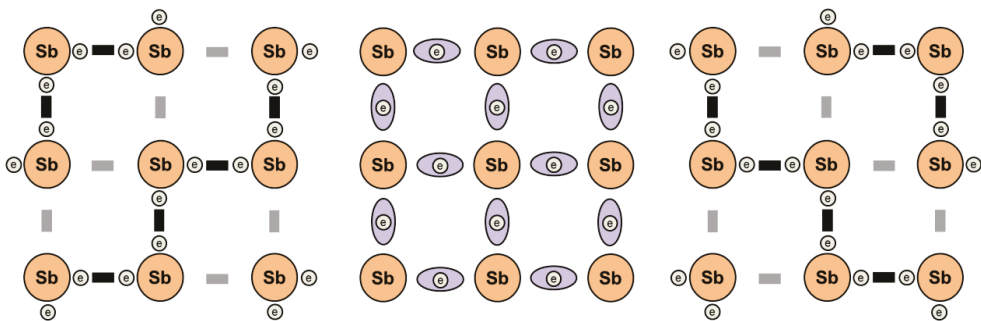


Figure 3: Simplified drawing of a hypothetical cubic Sb structure as an example of resonant bonding. Instead of forming covalent bonds and creating one of their possible structures (left and right) resonant bonding occurs. The Sb atoms are sharing one valence electron to build a bond. The case of resonant bonding is illustrated in the middle. Resonant bonding increases the electronic polarizability through an increase in electron delocalization. (Shportko et al., 2008)

An approach to systematically sort materials in relation to their qualification as phase change materials is the so-called treasure map by Lencer and co-workers (Lencer et al., 2008). The treasure map plots the materials hybridization against their ionicity. Phase change materials are found on the map where both properties are low and are not interfering with resonant bonding. High hybridization leads to larger distortions. Through the distortions, a smaller number of saturated covalent bonds are favored over resonant bonding. High ionicity localizes the valence electrons too close to the ion cores, from where they cannot participate in resonant bonding anymore. The

treasure map and a simple scheme of the resonant bonding destroying effects of hybridization and ionicity are shown in **Figure 4**.

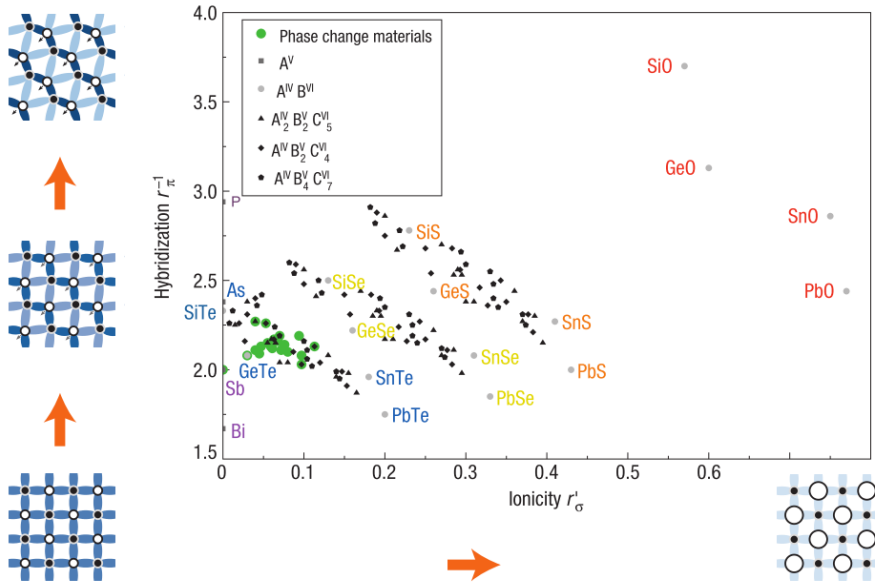


Figure 4: The treasure map of Lencer and co-workers is shown. Phase change materials are located at low values of hybridization and ionicity. A smaller number of saturated covalent bonds are favored by high hybridization (left). High ionicity localizes the valence electrons, from where they cannot participate in resonant bonding (bottom). Image reprinted with permission from the publication of Lencer and co-workers (Lencer et al., 2008).

The crystalline structure of phase change materials was in focus of many research topics (Agaev & Semiletov, 1965; Shelimova et al., 1998; Matsunaga et al., 2001). In the process of crystallizing phase change materials it is important to be aware of possible metastable phases. This is of further importance because in working condition as optical or electronic memories, phase change materials tend to crystallize in the metastable phase (Matsunaga & Yamada, 2004). The recent development of interfacial phase change memories (IPCM) by Simpson and co-workers sparks new interest in the research of the specific layered crystalline structures of the IPCM. IPCM are layered super lattice structures of alternating different phase change materials. Best known is the alternation between few nanometer thin GeTe and Sb_2Te_3 layers. The IPCM found by Simpson and co-workers switches between different resistive states by using lower power while

switching at higher speeds. Therefore they are very interesting materials for future memory applications (Simpson et al., 2011).

The structure of the amorphous phase of phase change materials is still in great debate. The properties of the amorphous phase also depend on the deposition method or the thermal conditions of the quenching from the melt. It was observed that the crystallization kinetics of the as deposited amorphous phase shows different properties than the amorphous phase obtained after quenching the material from the melt (Coombs et al., 1995; Weidenhof et al., 2001; Lee et al., 2009b; Salinga et al., 2013). This is important to know, because the crystallization is the main speed limiting factor of the switching speed of phase change memory devices. A lot of research on phase change materials focuses on the as deposited amorphous phase. The reason behind this is the less demanding synthesis of the as deposited amorphous phase. For the as deposited state, no quenching with high cooling rates is required. This makes it more difficult to relate the research results on as deposited material to real applications which are dealing with the melt quenched amorphous phase. The glassy or super cooled liquid state and the role of relaxation of the amorphous phase is also a topic of recent research. For example, Salinga and co-worker have demonstrated that $\text{Ag}_4\text{In}_3\text{Sb}_{67}\text{Te}_{26}$ (AIST) in the melt quenched phase shows an Arrhenius behavior of a glass for its crystal growth velocity over eight orders of magnitude and has a surprisingly high fragility (Salinga et al., 2013).

To tackle the challenges to find and optimize new forms of computer memories the “Deutsche Forschungsgemeinschaft” (DFG) has funded the “Sonderforschungsbereich 917 Nanoswitches” (SFB 917) for four years. The SFB 917 is a project including many institutes of the RWTH Aachen University and the “Forschungszentrum Jülich” of the Helmholtz Association to research the properties of resistive switching materials. These materials are possible candidates for future electronic non-volatile memory technologies. The two main areas of research in the SFB are phase change materials and oxides. The present thesis is focused on the research on phase change materials and is part of ongoing work in the Central Facility for Electron Microscopy (GFE) and in the Ernst Ruska Centre (ER-C) at the “Forschungszentrum Jülich”, funded by the SFB 917. The different groups of the SFB 917 are working on various topics related to phase change materials and oxides. The GFE and the ER-C is specialized in transmission electron microscopy (TEM; also used as synonym for transmission electron microscope) and its related techniques.

Therefore TEM methods build the basis of this work dealing with the investigation of phase change materials.

Abbe proposed in 1873 that the wavelength and the numerical aperture are the limiting factor of resolution of a microscope (Abbe, 1873). Therefore light microscopes are limited to resolutions in the region of a few hundred nanometers. TEMs are using the small wavelength of accelerated electrons, which amounts to a wavelength of 1.97 pm at an acceleration voltage of 300 kV (Williams & Carter, 2009). The theoretical foundation for TEMs were proposed by Knoll and Ruska in 1932 (Knoll & Ruska, 1932). The company Siemens and Halske was the first producer of commercially successful TEMs. Conventional TEMs at 200 kV have a resolution up to 0.2 nm (Jeol, 2016), which made them already very useful analytical instruments. Aberrations of the magnetic lenses prevented TEMs to reach better resolutions (Hawkes, 2009). In 1998 Haider and co-workers published the first high resolution images of a commercial TEM that was aberration corrected by a multipole lens design (Haider et al., 1998). This was the foundation of the state of the art multipole corrected TEMs and STEMs (scanning electron microscopy / microscope) of today. Up to date spherical aberration corrected TEMs at 200 kV reach a resolution of better than 0.1 nm (Heggen et al., 2016; Jeol, 2016).

The magnetic lenses used in the TEM hold also additional advantages. The strength of the lenses can be controlled continuously by changing the electrical current. This makes the complex lens setups of TEMs highly flexible. In addition there is a variety of different detectors mountable in a TEM. Depending on the construction of the actual microscope with the available lenses and detectors, many different experimental techniques and methods are possible. Especially diffraction methods which give information about the structure of materials were always a feature of TEM with valuable scientific applications. Additional scanning coils allow STEM imaging and analysis which use a small electron beam probe to scan a specimen to generate images or spectroscopy data sets digitally pixel by pixel. Also mixtures of methods are possible. For example nano area electron diffraction (NAED) which uses the scanning ability of a STEM and a small almost parallel coherent probe to record diffraction patterns of a sample scanned point by point on a CCD-Chip (charged-coupled device) (Reimer & Kohl, 2008; Williams & Carter, 2009; Pennycook & Nellist, 2011).

All TEM related techniques require electron transparent specimens. Specimen thicknesses of below 100 nm are needed for TEM analysis. This makes specimen preparation for every new material and geometry a new challenge. TEM specimen preparation is in most cases a destructive process for at least a part of the original sample. There is a variety of methods to get thin TEM specimens. They are thinning methods that get finer and more difficult by approaching smaller and smaller specimen thicknesses (Anderson & Walck, 1997). State of the art is the focused ion beam (FIB) technique, especially in combination with a build in scanning electron microscope (SEM) (dual beam FIB/SEM). The FIB revolutionized TEM sample preparation. FIB makes it possible to cut out very thin lamellas out of many different materials often in less than a day. Most other TEM specimen preparation methods starting with a bulk sample cannot compete with that preparation speed or fail at preparation of certain materials. It is also probably one of the best methods to produce very clean and very thin samples required for several TEM methods (Giannuzzi, 2005; Schmidt & Wetzig, 2013; Cox, 2015).

The diffraction of the electron beam by the specimen of the investigated material makes it possible to distinguish the amorphous from the crystalline phase in TEM specimens. The contrast in the images is related to the diffraction processes in the different phases. The contrast of crystalline specimens is also related to the specimen orientation. This is very useful for the investigation of phase change materials (Salinga et al., 2013; Oosthoek, 2014a). Also diffraction methods in the TEM and STEM are especially useful for phase characterization. Methods like NAED can probe a phase change material on the nanometer scale while gathering the information from diffraction patterns (Meister et al., 2006; Saltzmann et al., 2015). Fluctuation electron microscopy (FEM) uses a statistically significant amount of NAED patterns taken from the amorphous phase to get information about the structure of the medium range order (MRO) of the amorphous phase. This information can be used to relate the structure of the amorphous phase to the crystallization kinetics (Voyles & Muller, 2002; Lee et al., 2009a; Benke, 2017). High resolution imaging techniques in TEM or STEM make it possible to investigate structures of epitaxially grown phase change materials at atomic resolution (Kuypers et al., 1988; Kooi & De Hosson, 2002; Thelanger, 2015).

2 Main objectives of this thesis

This thesis is a collection of work as a doctoral student in the SFB 917. In the SFB 917 various research questions related to phase change materials were tackled. My work has the goal to help to answer these questions by the use of TEM and related techniques. In the following a short overview is given about the four research topics of this thesis.

2.1 Crystallization kinetics of AIST and GeTe thin films

The crystallization kinetics of phase change materials influences important properties of possible phase change memories. These include switching speed, retention time and scalability. The I. Institute of Physics (IA) has built an optical laser testing setup to measure the speed of the crystallization from the melt quenched phase of growth dominated phase change materials over a wide range of temperatures. The setup can even measure in the high temperature regime (Kaldenbach, 2012; Salinga et al., 2013; Benke, 2017). The high temperature regime is the most relevant for industrially applied phase change memory devices, because only at high temperatures fast switching occurs. The mentioned setup was used for growth velocity measurements of AIST (Salinga et al., 2013). In this work the growth velocities of AIST and GeTe are measured directly by TEM bright field imaging of grains grown in a matrix of the amorphous phase. This is done for sputtered as deposited material and material molten by laser and then quenched to room temperature. Our TEM measurements are important as reference for comparison with the optical laser setup, because the optical laser setup measures the crystallization growth velocity indirectly by measuring the change in reflectivity of a recrystallized small amorphous area (Kaldenbach, 2012; Benke, 2017). Furthermore, it is not possible for the optical laser setup to measure as deposited materials, which is done in this work by TEM in the lower temperature regime. In addition, we have investigated lamellas of as deposited and melt quenched AIST and GeTe by FEM. FEM gives information about the structure of the MRO of a material which influences the crystallization kinetics of phase change materials (Lee et al., 2009b; Lee et al., 2014). Therefore also the relation of the growth velocity measurements and the FEM results will be investigated. The presented results are part of the dissertation of J. Benke (Benke, 2017), and the bachelor and master thesis of J. Pries (Pries, 2013; Pries, 2015).

2.2 TEM investigations of AIST line-cell cross sections

To investigate the behavior of electronic switching of phase change materials close to the conditions of real electronic memory devices, the I. Institute of Physics (IA) developed vertical phase change line cells (Wimmer, 2015). In this work, FIB cross section TEM lamellae of AIST line cells were prepared by dual beam FIB/SEM and investigated by TEM bright field imaging.

2.3 Nano area diffraction of Sb_2Te_3 platelet intermediates

The Institute of Inorganic Chemistry has produced single crystalline hexagonal Sb_2Te_3 platelets by a wet chemical solvothermal synthesis applied by T. Saltzmann. These platelets can be a model system for phase change materials. The intermediates of the reaction path of the synthesis were investigated by annular dark field (ADF) STEM and NAED. The presented results are part of a publication in cooperation with T. Saltzmann and co-workers (Saltzmann et al., 2015) and the dissertation of T. Saltzmann (Saltzmann, 2014).

2.4 TEM/STEM investigations of a $\text{Ge}_1\text{Sb}_2\text{Te}_4$ layer grown by MOVPE

In IPCM, the switching part of the crystalline material is limited in volume by introducing a super lattice structure. This decreases energy consumption, switching time and increases the memory retention. The best known example is an alternation of few nanometer thin layers of cubic GeTe and hexagonal Sb_2Te_3 layers (Simpson et al., 2011). Their actual switching mechanism is not yet completely understood. The stable phases of Ge, Sb and Te (GST) alloys have highly ordered layered structures similar to the structures of IPCM but without an artificial super lattice design (Matsunaga et al., 2004; Da Silva et al., 2008). Therefore the stable phases of GST are very interesting materials to understand the switching process of IPCM or similar layered materials in detail. S. Riess of the Peter Grünberg Institute 9 (PGI-9) deposited $\text{Ge}_1\text{Sb}_2\text{Te}_4$ (GST 124) in the stable phase directly on a Si (111) substrate by metal organic vapor phase epitaxy (MOVPE) (Schuck et al., 2015; Hardtdegen et al., 2016; Riess, 2017). In this work, GST 124 deposited by MOVPE will be investigated by TEM and high resolution STEM (HRSTEM). The results are also part of the dissertation of S. Riess (Riess, 2017) and a publication with H. Hardtdegen and co-workers (Hardtdegen et al., 2016).

3 Crystallization kinetics of phase change materials

The understanding of crystallization kinetics of phase change materials is one of the major keys to optimize phase change materials as memory devices. The crystallization of an amorphous area of phase change memory is the most time consuming step if used as data storage element. The research on phase change materials has the goal to reduce the time of crystallization while contrary related properties like retention times have to be considered. Crystallization kinetics has to be understood to optimize phase change materials for the various challenges of memory applications.

The crystalline phase is the stable phase of solid materials at room temperature and at atmospheric pressure. A stable phase is the phase with the lowest Gibbs free energy at a given temperature and pressure. The difference between the Gibbs free energy of a given phase and the Gibbs free energy of a phase lower in energy produces a driving force supporting the phase transformation into the lower energy phase (Gibbs, 1906; Porter & Easterling, 1992; Ziegler, 2005).

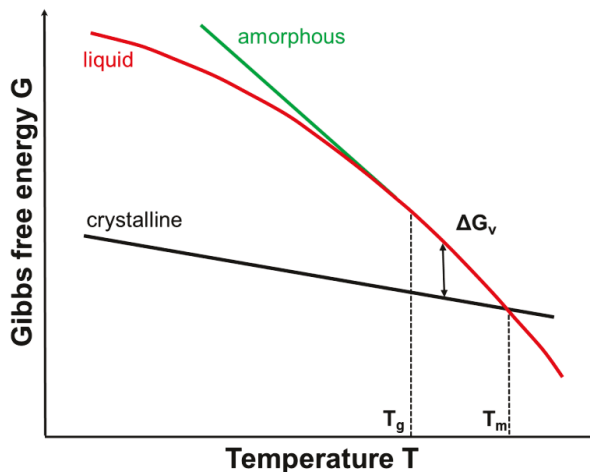


Figure 5: Diagram of the Gibbs free energy G in relation to the temperature T of the liquid, amorphous and crystalline state at atmospheric pressure. ΔG_v is the driving force of phase transformation (Ziegler, 2005).

In **Figure 5** the Gibbs free energy G is shown in relation to temperature T . The liquid, amorphous and crystalline states are schematically compared at atmospheric pressure. Above the melting temperature T_m , it is energetically favorable to form the liquid phase. At T_m the Gibbs free energy is the same for the liquid and the crystalline

phase. Below T_m it is energetically favorable to form the crystalline phase. If a material is cooled fast enough below the glass transition temperature T_g the mobility of the atoms decreases so rapidly that the atoms cannot build the energetically favored crystal lattices. The material is frozen in the metastable amorphous state. The transformation to the energetically favorable phase gives an energy gain equal to the difference in Gibbs free energy ΔG_v , but first an energetical barrier called the activation energy E_a has to be overcome (Gibbs, 1906; Porter & Easterling, 1992; Ziegler, 2005). This is illustrated in **Figure 5** and **Figure 6**.

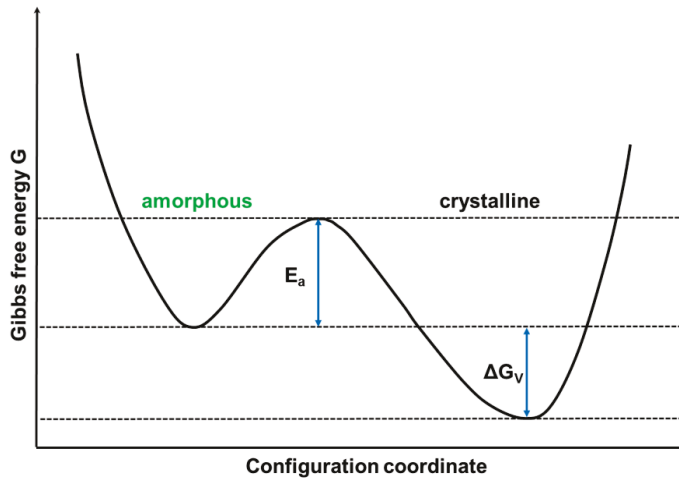


Figure 6: Diagram of the Gibbs free energy G in relation to the configuration coordinate at a temperature below the melting temperature T_m . The phase transformation from the amorphous to the crystalline phase gives an energy gain of the amount of the difference of the Gibbs free energy ΔG_v , but first the barrier of the activation energy E_a has to be overcome (Ziegler, 2005).

Some phase change materials, like the different alloys of GST, have metastable crystalline phases below the melting temperature. Their Gibbs free energies are located between the liquid phase and the energetically most favourable crystalline stable phase (Matsunaga et al., 2004; Meinders et al., 2006; Herlach, 2007).

Crystallization is a process which consists of two main processes. These processes are nucleation and grain growth. Nucleation is the statistical manifestation of the smallest stable crystalline grains, so called nuclei, in an amorphous material. Growth means the growth of these crystalline grains by consuming their surrounding amorphous phase. A description of the classical theory is given for nucleation in **Chapter 3.1** and for growth in **Chapter 3.2**. The speed of crystallization is depending on temperature. At high temperatures close to T_m the mobility of atoms is high,

therefore it is easy for them to reach the location of crystallization and rearrange to form crystalline lattices.

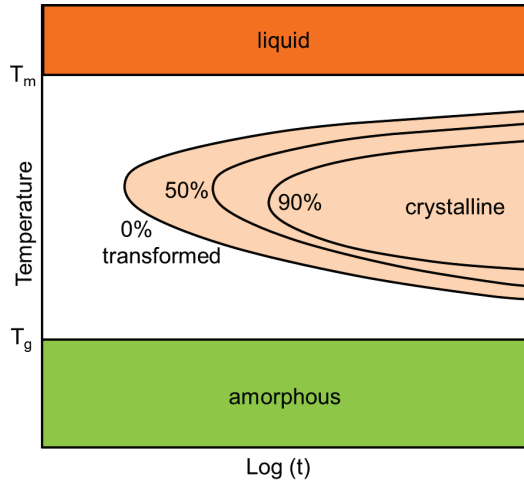


Figure 7: TTT-Diagram which shows the amount of phase transformation at a given temperature and time t . If cooling from the liquid phase is fast enough crystallization can be completely avoided and the material is frozen in the amorphous phase (Wuttig & Yamada, 2007; Cavagna, 2009).

On the other hand the gain of energy by building a crystal at high temperature is low, which results in a low driving force of crystallization. At low temperature close to T_g there is a high driving force but a low mobility of the atoms. The result is an ideal temperature between T_m and T_g where crystallization is fastest. To freeze the material in the amorphous phase the cooling rate has to be high enough to avoid any phase transformation into one of the crystalline phases. A visualization of this is given by time-temperature-transformation (TTT) diagrams. They show the amount of material that has crystallized after different times at different temperatures (Wuttig & Yamada, 2007; Cavagna, 2009). **Figure 7** shows the nose shaped maximum of crystallization speed in a schematic TTT diagram.

Phase change materials can be categorized as nucleation dominated or growth dominated materials (Zhou, 2001; Meinders et al., 2006). **Figure 8** gives a schematic explanation of nucleation and growth dominated transformation in the crystalline state.

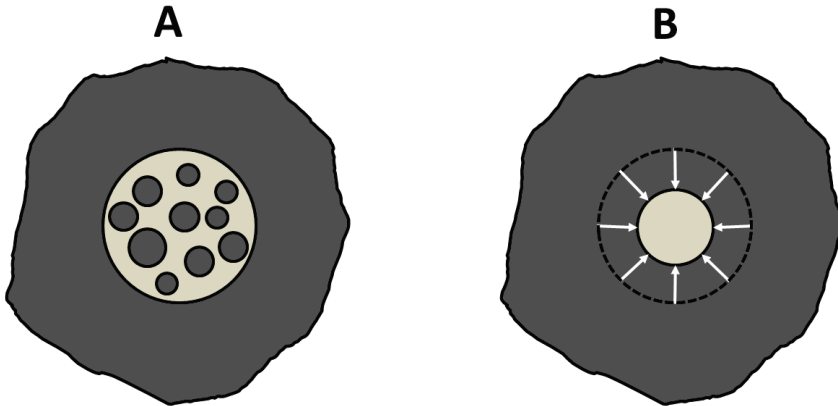


Figure 8: Schematic drawing of the two crystallization mechanisms of nucleation dominated phase change materials and growth dominated phase change materials. (A) Nucleation dominated phase change materials transform a given amorphous area by nucleation and followed growth of the nuclei. (B) Growth dominated phase change materials transform this amorphous area by crystal growth of the crystalline rim into the centre before significant nucleation can occur (Zhou, 2001).

Nucleation dominated materials transform a given amorphous volume in a matrix of crystalline surrounding by statistically appearing and growing nuclei. Growth dominated materials deplete the amorphous volume by growth of the crystalline surrounding to the centre of the area, before significant amount of nucleation can occur. This categorization is straightforward, but the size of the amorphous area or volume and its dependency on temperature has to be taken into account. The temperature is an important parameter, because nucleation rate and growth rate depend on temperature (Cavagna, 2009). Bigger areas or volumes favour the nucleation dominated category, because nucleation is more likely to happen before the crystalline matrix transforms the amorphous area by growth. Scaling to smaller amorphous regions favours fast growth and therefore growth dominated materials over nucleation, thus, if an area gets small enough, every phase change material is growth dominated (Zhou, 2001; Meinders et al., 2006). Growth dominated phase change materials are probably better suited for applications of future small scale dimensions, even if they are falling behind crystallization speed of nucleation dominated phase change materials at recent bigger scaling sizes.

3.1 Nucleation

3.1.1 Homogeneous crystal nucleation

The change in Gibbs free energy is the driving force of phase transformation. The change of the Gibbs free energy per unit volume ΔG_V can be written as the change in enthalpy per unit volume ΔH_V and the change in entropy per unit volume ΔS_V multiplied by temperature T (Gibbs, 1906; Porter & Easterling, 1992; Friedrich, 2000):

$$\Delta G_V = \Delta H_V - T \cdot \Delta S_V \quad (1).$$

ΔG_V is zero at the melting temperature T_m so ΔS_V can be written as:

$$\Delta S_V = \frac{\Delta H_V}{T_m} \quad (2).$$

If ΔS_V in **Equation 1** is substituted by **Equation 2** it can be written as:

$$\Delta G_V = \Delta H_V \cdot \frac{(T_m - T)}{T_m} \quad (3).$$

The super cooling of the melt is expressed by $(T_m - T)$ and the enthalpy ΔH_V is a synonym for the latent heat of the system. ΔG_V is negative for metastable systems. In the case of homogeneous nucleation, in addition to a driving force in form of ΔG_V , nuclei of the energetically favoured phase have to manifest to start crystallization. A nucleus is an agglomeration of atoms in the configuration of the new energetic more favourable phase. Nuclei are formed by thermal fluctuations. The surface area of the volume of a nucleus forms a phase boundary to the surrounding amorphous phase. The energy of the phase boundary is the result of the multiplication of the specific surface energy γ multiplied by the surface area A . The total change of the Gibbs free energy ΔG for the simplified case of a symmetric spherical nucleus with the surface area A , the volume V and the radius r is then defined as (Gibbs, 1906; Christian, 1965; Kelton, 1991; Porter & Easterling, 1992; Friedrich, 2000; Gottstein, 2007; Raoux, 2009):

$$\Delta G = \gamma \cdot A + \Delta G_V \cdot V = \gamma \cdot 4\pi r^2 + \Delta G_V \cdot \frac{4}{3}\pi r^3 \quad (4).$$

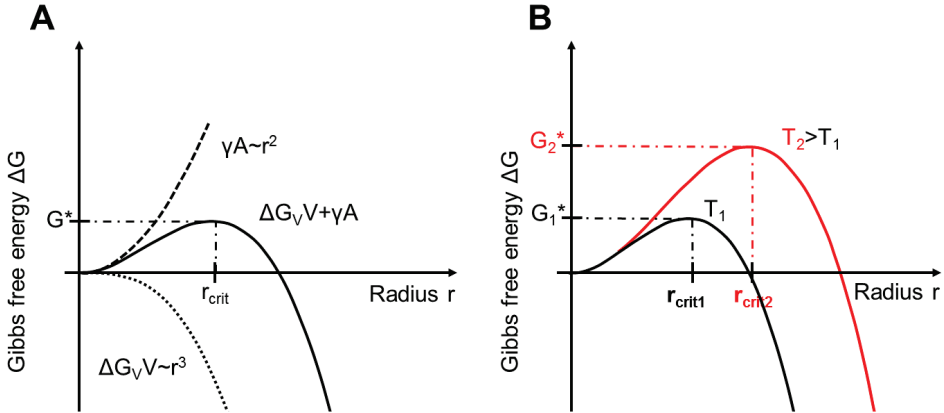


Figure 9: Graphs of the relation of the Gibbs free energy ΔG and the radius r of an agglomeration of atoms with crystalline order. (A) If the radius of a nucleus is smaller than the critical radius r_{crit} it is energetically more favorable for the sub critical nucleus to decay. If the radius of the nucleus is larger than the critical radius r_{crit} it is energetically more favorable for the nucleus to grow. (B) The critical radius r_{crit} increases with increasing temperature T (Gibbs, 1906; Christian, 1965; Kelton, 1991; Friedrich, 2000; Raoux, 2009).

Figure 9 shows the radius of the nucleus r in relation to ΔG . **Equation 4** has a maximum of the Gibbs free energy G^* at the critical radius r_{crit} . With increasing radius, there is an increase of ΔG caused by the increasing surface area of the nucleus. This increases the energy of the phase boundary. On the other hand there is a decrease of ΔG caused by the increasing volume of the lower energy phase of the nucleus. Randomly formed nuclei, with a radius smaller than r_{crit} , decay again, because the shrinking of the nuclei decreases ΔG . On the other hand nuclei bigger than r_{crit} grow, because then the growth decreases ΔG (Gibbs, 1906; Porter & Easterling, 1992; Friedrich, 2000; Gottstein, 2007). The slope of ΔG is zero if the radius of the nuclei is equal to r_{crit} :

$$\frac{d(\Delta G(r_{crit}))}{dr} = 0 \quad (5).$$

From **Equation 4** and the information of **Equation 5** r_{crit} can be derived:

$$r_{crit} = \frac{2\gamma}{\Delta G_V} = -\frac{2\gamma}{\Delta H_V} \cdot \frac{T_m}{(T_m - T)} \quad (6).$$

Then G^* can be calculated by inserting **Equation 6** into **Equation 4**:

$$G^* = \frac{16\pi}{3} \cdot \frac{\gamma^3}{(\Delta G_V)^2} = \frac{16\pi}{3} \cdot \frac{\gamma^3}{(\Delta H_V)^2} \cdot \frac{T_m^2}{(T_m - T)^2} \quad (7).$$

From **Equation 6** and **Equation 7** it is clear that r_{crit} and G^* are increasing with temperature. This means that it will be more and more unlikely to form nuclei bigger than r_{crit} at higher temperatures (**Figure 9**). G^* can be seen as an energy barrier of the nucleation at the given temperature. This energy barrier makes the undercooling of liquids possible. Even if the new phase is energetically more favourable, nuclei with bigger radii than the critical radius r_{crit} have to form first. (Gibbs, 1906; Christian, 1965; Kelton, 1991; Porter & Easterling, 1992; Friedrich, 2000; Raoux, 2009).

The first kinetic model for nucleation was introduced by Volmer and Weber (Volmer & Weber, 1926; Raoux, 2009). They used the Boltzmann distribution to calculate the amount of clusters at G^* . The number of nuclei with the critical radius $N(r_{crit})$ were defined at the equilibrium between decay and growth by:

$$N(r_{crit}) = N_0 \cdot \exp\left(-\frac{G^*}{k_B T}\right) \quad (8),$$

where N_0 is the total amount of atoms in the liquid and k_B is the Boltzmann constant. They assumed that after addition of one additional atom to a critical nucleus, the nucleation event takes place and the nucleus starts to grow. They defined the nucleation rate at the equilibrium I_{equ} by:

$$I_{equ} = s_{crit} \cdot k \cdot N(r_{crit}) = s_{crit} \cdot k \cdot N_0 \cdot \exp\left(-\frac{G^*}{k_B T}\right) \quad (9),$$

where s_{crit} is the number of surface atoms of the critical nucleus and k is the arrival rate of an atom from the amorphous parent phase adding to the crystalline cluster. The drawback of the model of Volmer and Weber is that the value for the amount of nuclei forming following the Boltzmann distribution $N(r)$ grows with increasing radii of nuclei bigger than the critical radius r_{crit} . This is physically not plausible. As a solution Volmer and Weber defined that the amount of nuclei $N(r)$ forming with radii bigger than r_{crit} is zero (Volmer & Weber, 1926; Raoux, 2009). Becker and Döring took another approach with their steady state model also based on the Boltzmann distribution. They did not neglect the fact that nuclei with radii bigger than r_{crit} could still decay and that critical nuclei with the radius r_{crit} have the equal possibility to shrink or grow. They defined that the number of nuclei with the radius r_{crit} in the steady state model $N_{ss}(r_{crit})$ is equal to half of the number of nuclei with the critical

radius $N(r_{crit})$ from the model of Volmer and Weber. Furthermore, the distribution of nuclei in steady state $N_{ss(r)}$ decreases gradually and not abruptly for nuclei with radii bigger than r_{crit} (Becker & Döring, 1935; Raoux, 2009). The steady state nucleation rate I_{ss} of Becker and Döring is defined by:

$$I_{ss} = s_{crit} \cdot k \cdot N_0 \cdot Z \cdot \exp\left(-\frac{G^*}{k_B T}\right) \quad (10),$$

with

$$Z = \frac{1}{i_{crit}} \left(\frac{G^*}{3\pi k_B T} \right)^{\frac{1}{2}} \quad (11),$$

where Z is the Zeldovich factor, that describes the probability of an atom on top of the energy barrier to nucleate and not to dissolve and i_{crit} is the number of atoms in the critical nucleus. The Zeldovich factor Z is the main difference between the model of Volmer and Weber and the steady state model of Becker and Döring (Volmer & Weber, 1926; Becker & Döring, 1935; Raoux, 2009). **Figure 10** shows schematically the number of nuclei related to their radii for both models. For practical purposes, both models give very similar results, because the main factor of change are variations in the value of G^* , but the steady state model of Becker and Döring is physically more probable (Volmer & Weber, 1926; Becker & Döring, 1935; Raoux, 2009). Turnbull and Fischer were the first who evaluated the preexponential factor of **Equation 10** for an undercooled liquid or an amorphous phase. They describe two cases, the diffusion-limited and the collision limited case. Both cases have a different arrival rate of atoms k in **Equation 10**. In the diffusion limited case crystallization happens by changes of atom positions by diffusive jumps of atoms through the phase boundary (Turnbull & Fisher, 1949; Raoux, 2009). They defined the arrival rate k for the diffusion limited case by:

$$k = \frac{6D}{\lambda^2} \quad (12),$$

where D is the diffusivity in the undercooled liquid or amorphous phase and λ the average interatomic distance.

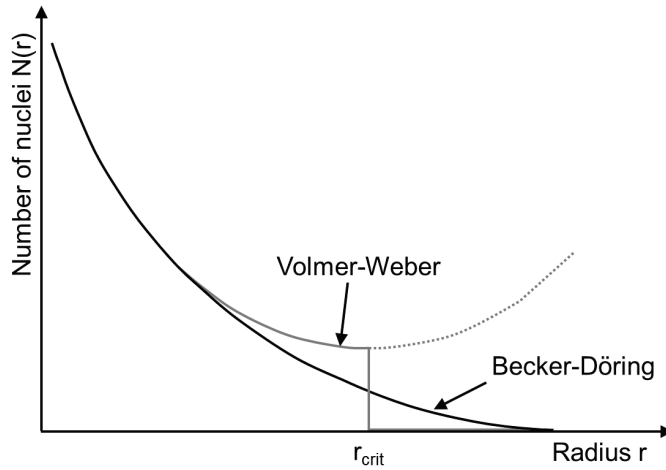


Figure 10: Graphs of the number of nuclei forming by thermal fluctuations related to their radii. The number of nuclei decreases abruptly to 0 for radii bigger than the critical radius r_{crit} in the Model of Volmer and Weber. In the steady state model of Becker and Döring the number of nuclei is decreasing gradually to zero. Furthermore the amount of critical nuclei is half the amount of critical nuclei in the model of Volmer and Weber (Volmer & Weber, 1926; Becker & Döring, 1935; Raoux, 2009).

By inserting **Equation 12** into **Equation 10** we get the nucleation rate for the diffusion limited case:

$$I_{ss} = s_{crit} \cdot \frac{6D}{\lambda^2} \cdot N_0 \cdot Z \cdot \exp\left(-\frac{G^*}{k_B T}\right) \quad (13).$$

By using the Stokes-Einstein equation the diffusivity is related to the viscosity η (Raoux, 2009):

$$\eta D = \frac{k_b T}{3\pi\lambda} \quad (14).$$

By inserting **Equation 14** into **Equation 13** the nucleation rate for the diffusion limited case is also related to the experimental more accessible viscosity (Raoux, 2009):

$$I_{ss} = s_{crit} \cdot \frac{k_b T}{\eta\pi\lambda^3} \cdot N_0 \cdot Z \cdot \exp\left(-\frac{G^*}{k_B T}\right) \quad (15).$$

The collision limited case assumes that crystallization does not need diffusive rearrangements of the atom positions. In the collision limited model the crystallization occurs through the motion of thermal vibrations of the atoms (Turnbull & Fisher,

1949; Raoux, 2009). Turnbull and Fischer defined the arrival factor for the collision limited case as:

$$k = \frac{u_{\text{sound}}}{\lambda} \quad (16),$$

where u_{sound} is the velocity of sound in the undercooled liquid or the amorphous phase. **Equation 16** inserted into **Equation 10** defines the nucleation rate of the collision limited case as (Turnbull & Fisher, 1949; Raoux, 2009):

$$I_{\text{ss}} = s_{\text{crit}} \cdot \frac{u_{\text{sound}}}{\lambda} \cdot N_0 \cdot Z \cdot \exp\left(-\frac{G^*}{k_B T}\right) \quad (17).$$

In the diffusion limited case I_{ss} close to T_m is negligibly small, because there is no more driving force of crystallization. Also at T_g there is a strong increase in viscosity and therefore I_{ss} gets small. This means I_{ss} has a maximum between T_m and T_g . I_{ss} for the collision limited case increases continuously. Only the behavior of I_{ss} for the diffusion limited case has been observed for phase change materials (Raoux, 2009).

3.1.2 Heterogeneous crystal nucleation

In addition to the homogeneous nucleation described above, there is also the case of heterogeneous nucleation. In this case, the nucleation is located at a preexisting boundary. This can for example be the substrate, preexisting particles or the walls of the reaction vessel. ΔG of a nucleus formed that way is decreased. Thus it is easier to form a stable nucleus. The decrease in ΔG is caused by a reduction of the surface and the volume of the nucleus. The smaller the contact angle θ is between the forming nucleus and the boundary interface, the smaller is the surface and the volume of the nucleus, which has to transform to reach r_{crit} . θ is connected to the interfacial energies. The contact angle θ is defined by the young equation:

$$\gamma_{\text{cs}} - \gamma_{\text{as}} = \gamma_{\text{ac}} \cdot \cos\theta \quad (18),$$

where γ_{cs} is the interfacial energy of the crystal to substrate interface, γ_{as} is the interfacial energy of the amorphous to substrate interface and γ_{ac} is the interfacial energy of the amorphous to crystalline interface (Young, 1805; Christian, 1965; Gottstein, 2007; Salinga, 2008; Raoux, 2009; Benke, 2017). The scheme of heterogeneous nucleation for Volmers spherical cap model is shown in **Figure 11**. With assumed isotropic phases, the curvatures of the interface between the

crystalline phase and the amorphous phase have to be equal everywhere. Therefore the crystalline phase creates a spherical cap on the wetted substrate.

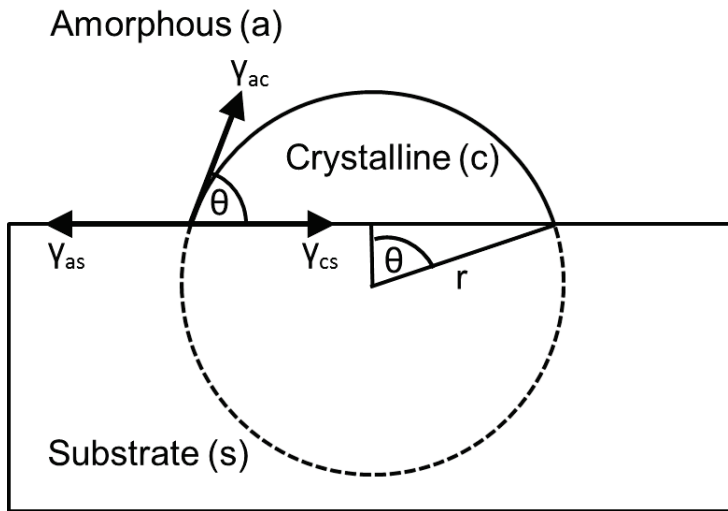


Figure 11: Schematic drawing of heterogeneous nucleation of spherical nucleus cap shows that with decreasing contact angle θ it is easier for a nucleus to reach the critical radius r_{crit} . θ is connected to the interfacial energies of the three shown phases by the Young equation (Young, 1805; Volmer, 1929; Salinga, 2008; Raoux, 2009).

The volume fraction $0 \leq f(\theta) \leq 1$ of the cap of a sphere with radius r depends on the contact angle θ and is defined by (Salinga, 2008; Raoux, 2009):

$$f(\theta) = \frac{(2 + \cos\theta)(1 - \cos\theta)^2}{4} \quad (19).$$

For heterogeneous nucleation the maximum of the Gibbs free energy G_{het}^* is equal to the maximum of the Gibbs free energy of homogeneous nucleation G_{hom}^* multiplied by the volume fraction $f(\theta)$ (Raoux, 2009):

$$G_{het}^* = G_{hom}^* \cdot f(\theta) = \frac{16\pi}{3} \cdot \frac{\gamma^3}{(\Delta G_V)^2} \cdot f(\theta) \quad (20).$$

The volume and number of atoms of the critical nuclei decreases in the case of heterogeneous nucleation, but r_{crit} is equal in homogenous and heterogeneous nucleation. Therefore it is energetically more favorable to nucleate heterogeneously. The steady state nucleation rate for diffusion limited heterogeneous nucleation $I_{ss,het}$ is then defined as (Raoux, 2009):

$$I_{ss,het} = \varepsilon \cdot s_{crit} \cdot \frac{6D}{\lambda^2} \cdot N_0 \cdot Z \cdot \exp\left(-\frac{G_{het}^*}{k_B T}\right) \quad (21),$$

where ε is the amount of atoms of the amorphous phase in contact with the substrate. In practical cases heterogeneous nucleation is more common. In most cases impurities or boundaries give possibilities for heterogeneous nucleation (Raoux, 2009).

3.2 Growth

It is energetically more favorable to grow for a crystalline nucleus with a radius bigger than r_{crit} . The crystal growth velocity is a combination of the velocity of atoms attaching to a nucleus and the velocity of atoms detaching from the nucleus. Below T_m it is energetically more favorable for atoms to attach. The growth is either interface controlled or diffusion controlled. In the case of interface controlled growth there is no phase separation at crystallization of the material. The composition of the amorphous and the crystalline material stays the same. Only the interface controlled growth will be discussed in this work, because a phase separation was not observed for our materials. The phase transition is happening at the amorphous to crystalline interface by rearrangement of atoms through diffusive jumps or atom collisions. The arrival rate k is in both cases independent from the position in the interface. The time independent growth velocity u can be defined as (Christian, 1965; Raoux, 2009):

$$u = \zeta_s \cdot \lambda \cdot k \cdot \left[1 - \exp\left(-\frac{\Delta G_{ac,atom}(T)}{k_B T}\right)\right] \quad (T \leq T_m) \quad (22),$$

where $0 \leq \zeta_s \leq 1$ is the amount of possible sites at which an atom can attach to the nucleus, λ is the average interatomic distance and $\Delta G_{ac,atom} \geq 0$ is the energy difference between the amorphous parent phase and crystalline phase per atom. The thermally activated transfer of atoms across the interface in both directions is described by the term in **Equation 22** in square brackets. The arrival rate k is equal to the analogous of the diffusion limited case (**Equation 12**) or collision limited case (**Equation 16**) of the nucleation theory (**Chapter 3.1.1**). For phase change materials the more relevant case is the diffusion limited growth. The growth velocity u of the diffusion limited case is defined as (Christian, 1965; Raoux, 2009):

$$u = \zeta_s \cdot \frac{6D}{\lambda} \cdot \left[1 - \exp\left(-\frac{\Delta G_{ac,atom}(T)}{k_B T}\right)\right] \quad (T \leq T_m) \quad (23).$$

By using the Stokes-Einstein equation (**Equation 14**) u can also be written as (Christian, 1965; Raoux, 2009):

$$u = \zeta_s \cdot \frac{2k_B T}{\eta \pi \lambda^2} \cdot \left[1 - \exp\left(-\frac{\Delta G_{ac,atom}(T)}{k_B T}\right) \right] \quad (T \leq T_m) \quad (24).$$

The growth velocity is zero at T_m , because there $\Delta G_{ac,atom}$ is also zero. The diffusivity and the viscosity dominate the change in the growth velocity close to T_g . Hence, for the diffusion limited case, it can be written (Raoux, 2009):

$$u \sim D \sim \frac{1}{\eta} \quad (25).$$

The diffusion limited interface controlled growth velocity u has a maximum between the melting temperature T_m , where u gets zero, and the glass transition temperature, where it gets negligibly small. At this maximum, the growth velocity is highest because of high mobility of the rearranging atoms and high driving force in form of the energy difference $\Delta G_{ac,atom}$. This maximum is normally located closer to T_m than the maximum of the steady state nucleation rate I_{ss} for the diffusion limited case (Raoux, 2009).

By inserting **Equation 16** in **Equation 22** the growth velocity u of the collision limited case of interface controlled growth is defined as (Christian, 1965; Raoux, 2009):

$$u = \zeta_s \cdot u_{sound} \cdot \left[1 - \exp\left(-\frac{\Delta G_{ac,atom}(T)}{k_B T}\right) \right] \quad (T \leq T_m) \quad (26).$$

where u_{sound} is the velocity of sound in the amorphous phase. In the collision limited case the growth velocity increases continuously with decreasing temperature. This behavior is not observed in phase change materials.

3.3 The role of the amorphous phase in phase change materials

The amorphous phase plays an important role in defining the crystallization kinetics of phase change materials. The amorphous phase is the phase in which the crystallization starts. The amorphous phase is defined as a solid phase lacking the long range order of crystalline materials (Zallen, 1983; Pennycook & Nellist, 2011; Egami & Billinge, 2012). This does not mean that the amorphous phase is completely random. Experimental analysis of pair distribution functions with neutron, X-ray and electron diffraction have probed two body and three body correlations in amorphous

materials. These correlations represent bond lengths, bond angles and coordination numbers and therefore the closest surrounding of the atoms. These correlations are combined under the name short range order (SRO) and they are in the length scale of 0.2 nm-0.4 nm (Elliott, 1990; Egami & Billinge, 2012). MRO names the length scale of correlation in the range of 0.5 nm - 4 nm. MRO represents three body and higher body correlations (Treacy et al., 2005). The two most influential models to understand the amorphous phase are the continuous random network model (Zachariasen, 1932) and the dense packed model for metals (Bernal, 1964). MRO is neglected in both models. MRO can help to describe building blocks of the crystallization processes like subcritical nuclei, nuclei and nanocrystals. Various experimental observations are attributed to the influence of the MRO (Sokolov et al., 1991; Pan et al., 2008; Lee et al., 2014). FEM (**Chapter 6.1.5.3**) is a method built on the work of Treacy and Gibson (Treacy & Gibson, 1996). FEM is sensitive to the amount of MRO in a sample (Voyles & Abelson, 2003). It has been shown that high amounts of MRO in the amorphous phase are an indication for an increased amount of subcritical nuclei (Lee et al., 2009b). Other effects in phase change materials grounded in the MRO still have to be investigated. The understanding of the role of the MRO can improve the understanding of the properties of the amorphous phase and their influence on crystallization of phase change materials.

An interesting view on the amorphous phase of phase change materials is also from the perspective of glass forming. Phase change materials are bad glass formers (Kalb et al., 2007; Raoux, 2009) and behave as fragile liquids (Raoux, 2009; Orava et al., 2012; Salinga et al., 2013). Quenching rates higher than 10^9 K s^{-1} are needed to quench phase change materials in the amorphous phase (Wuttig & Yamada, 2007). When the temperature is decreased below melting temperature, the phase change material becomes an undercooled liquid. The undercooled liquid is not the energetically stable phase anymore but the atoms still have enough mobility to be in a kind of metastable equilibrium (Raoux, 2009). To form the crystalline phase the atoms have to form nuclei or have to find crystalline sites they can attach to by growth (Porter & Easterling, 1992). To form an amorphous glass from the melt the decrease in temperature has to be fast enough that no crystallization occurs until the mobility of the atoms gets too low for crystallization on measurable time scales. Such rapid cooling is known as quenching. A low mobility of atoms results in a high viscosity. A material enters the glassy state when the viscosity is around 10^{12} Pas or

higher around the glass transition temperature (Elliott, 1990). The influence of the quenching rate on the viscosity is shown in **Figure 12**.

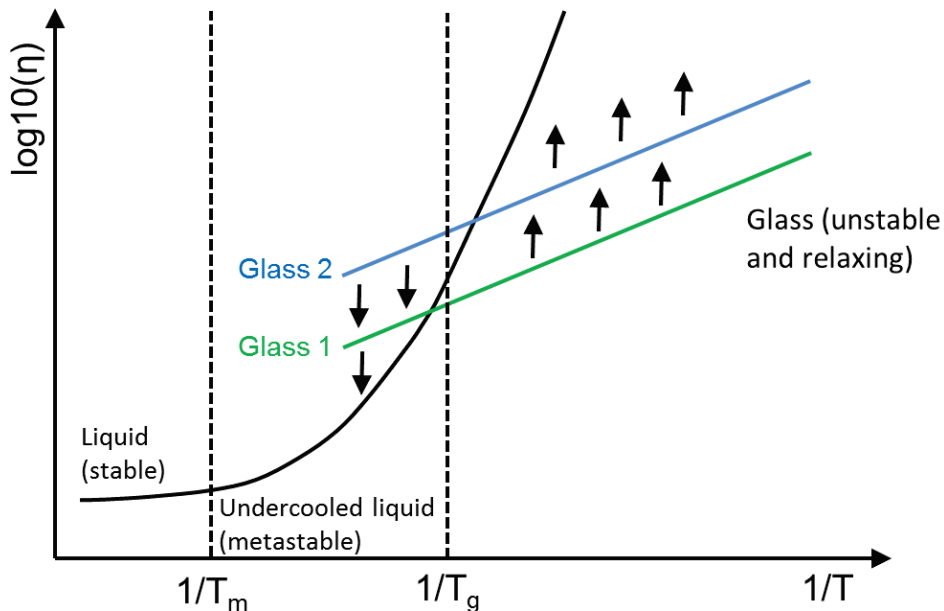


Figure 12: Schematic graph of the viscosity related to the reciprocal temperature. Above the melting temperature T_m the phase change material is in the liquid state. Below T_m the phase change material becomes an undercooled liquid with high enough mobility of the atoms to maintain a metastable equilibrium. When the mobility of the atoms gets too low around the glass transition temperature T_g the phase change material freezes as an amorphous non-equilibrium glass. Faster cooling of the phase change material causes an earlier freezing of the material in the glassy state (Glass 1). Slower cooling causes a delayed transition (Glass 2). At indefinitely slow cooling the metastable equilibrium keeps intact and the material stays in the undercooled liquid state. The glass is not stable and the configuration of the atoms relaxes in direction of the metastable equilibrium of the undercooled liquid indicated by the arrows (Raoux, 2009).

At higher quenching rates, the atom configuration is further away from the metastable internal equilibrium of the undercooled liquid. Also higher quenching rates lead to an earlier transition to the glassy state. Shown in **Figure 12** is the difference of the slope between the undercooled liquid and the glassy state. While in the glassy state the viscosity shows Arrhenius like behaviour, this is not the case for the undercooled liquid. The glassy states are relaxing into the direction of an ideal undercooled liquid. The arrows in **Figure 12** show the relaxation direction (Raoux, 2009). The mentioned drift in the glassy state is one of the reasons that the properties of phase change materials in the amorphous phase are also drifting. This is especially important when main properties defining the qualities as memory devices are affected. Resistance

drift of the amorphous phase of phase change materials is for example one of the main challenges that have to be overcome to build multilevel memories from phase change materials (Ielmini et al., 2009; Lavizzari et al., 2009; Wimmer et al., 2014; Stanisavljevic et al., 2015).

4 Electrically switched phase change devices

Non-volatile electronic memories are the favoured choice of memory in mobile devices. Phase change materials are interesting candidates for such memories (Zhong et al., 2014). Like in optical data storage media, the difference in the structural phase of phase change materials relates to a difference in property. In electrically switched phase change memories the resistivity can change from a high resistive amorphous state to a low resistive crystalline state and vice versa. The switching itself is induced by joule heating from the flowing electrical current. To create the amorphous state, a relatively short high current pulse heats the phase change material above the melting temperature. The heating pulse melts the crystalline phase change material which is then quenched into the amorphous high resistive state. To crystallize the amorphous region a pulse with lower current heats the amorphous phase change material above the glass transition temperature but beneath the melting temperature. For complete crystallization the pulse duration has to be long enough to give the atoms of the phase change material the needed time for their rearrangement (**Figure 1**) (Ovshinsky, 1968; Karpov & Kostylev, 2006).

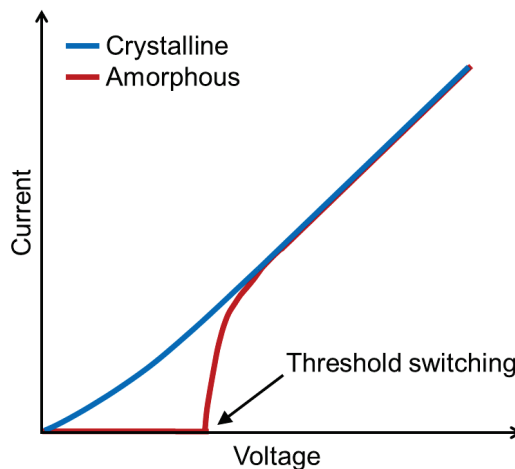


Figure 13: Schematic graph of current related to voltage showing the effect of threshold switching of phase change materials. At the voltage of threshold switching the resistivity of the amorphous phase change material decreases rapidly. This increases the current which helps to reach the temperatures needed for crystallization (Raoux, 2009).

Already Ovshinsky observed the so called threshold switching of phase change materials (Ovshinsky, 1968). Even before crystallization, phase change materials

switch in a lower resistive state after a certain threshold voltage is reached. The threshold switching is schematically shown in **Figure 13**. This low resistive state keeps even intact for lower voltages after the threshold switching event took place. Threshold switching is required to make phase change materials interesting as electronic non-volatile memory devices. The voltage needed to reach high enough heating currents for crystallization in the high resistive state, without threshold switching, would be too high and therefore energy inefficient. To read the saved information, a readout pulse is sent through the phase change material that has lower voltage as the threshold voltage. Both states are then defined by the amount of current the read out pulse generates (Raoux, 2009; Wimmer, 2015).

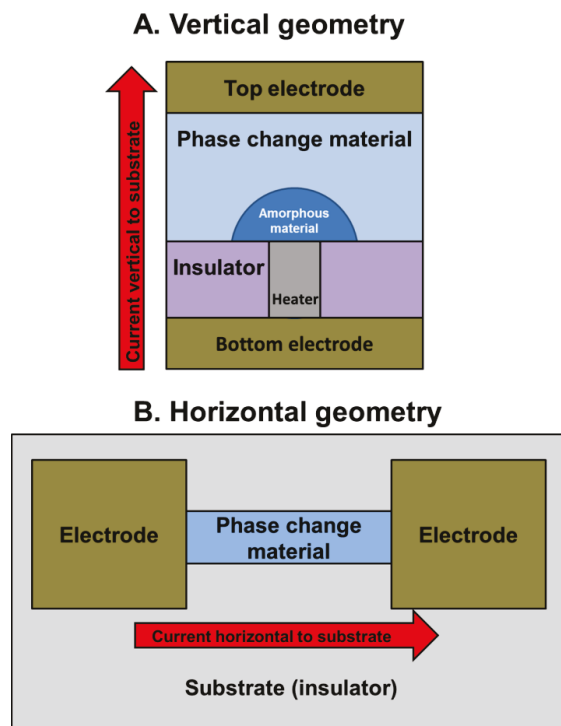


Figure 14: Electronic phase change memory cell layouts are showing two main layouts. (A) In vertical geometry the current flows orthogonal to the substrate surface. (B) In horizontal cells the current flows parallel to the substrate surface (Lankhorst et al., 2005; Kau et al., 2009; Raoux, 2009; Oosthoek, 2014a).

There are various designs of electronic phase change memory devices. **Figure 14** shows general diagrams of the two most frequently used designs which are vertical and horizontal cells (Lankhorst et al., 2005; Kau et al., 2009; Raoux, 2009; Oosthoek, 2014a). The name refers to the direction the switching current flows in relation to the

device substrate surface. In vertical geometry like in the so called mushroom cell, the electrical current flows orthogonal to the substrate surface. In horizontal cells the electrical current flows parallel to the substrate surface. The horizontal cells have often a more simple design which makes them interesting to be built as research devices. Vertical designs promise a higher density of memory cells on a single wafer. Some designs implement a heater. When the voltage increases, it supplies part of the heat for the phase switch. There is also increasing research in creating more than only two readable states. This for example could be realized by switching only a part of the cell. Depending on the amount of phase change material, that is switched in one cell, the resistivity is different (Ielmini et al., 2009; Lavizzari et al., 2009; Raoux, 2009; Stanisavljevic et al., 2015).

5 Interfacial phase change materials

In 2011 it was found by Simpson and co-workers that the switching properties of a composition of alternating layers of a few nanometer of hexagonal Sb_2Te_3 and a few nanometer of cubic GeTe were drastically improved compared to normal GST 225 (Tominaga et al., 2008; Simpson et al., 2011). Simpson called these superlattice structures interfacial phase change materials (IPCM). Simpson showed that the IPCM superlattice structure stays intact in the low and in the high resistive state of an electrically switched IPCM vertical cell. They have demonstrated that melting of the whole IPCM superlattice actually damages the IPCM by losing the superlattice structure and its improved properties. This means, the material is not switched by melting and crystallization of the whole IPCM superlattice. They have speculated that the switching is confined to a rearrangement of Ge atoms in the interface between Sb_2Te_3 and GeTe. But the actual switching mechanism of IPCM is still in debate (Tominaga et al., 2008; Simpson et al., 2011; Shintani & Saiki, 2013; Ohyanagi et al., 2014). GST alloys that are grown in the stable phase show structural similarities to the IPCM structures. Both are composed of building blocks of trigonal layers separated by van der Waals gaps (Hardtdegen et al., 2016). So it will be very interesting to compare the switching properties of both material classes. A thorough understanding of the switching mechanism of IPCM and how it can be translated to other phase change material combinations would be valuable for the future design process of non-volatile phase change memory devices.

6 Experimental

In the following chapters an overview of the used equipment and methods for analysis and specimen preparation is given. The analytical electron microscopy methods are completed by a brief description of the relevant theories and references to literature. In the chapters of the specimen preparation every preparation step is described or referenced to a detailed preparation description in literature.

6.1 Electron microscopy

The theory about electron microscopy fills many books. This thesis can only give a very short overview to the subjects related to this work. For a deeper or more complete look into electron microscopy the reader should for example look into the books of Reimer, Williams and Pennycook where also the main part of the theory of this thesis is taken from (Reimer & Kohl, 2008; Williams & Carter, 2009; Pennycook & Nellist, 2011). This thesis focuses on the use of TEM and STEM. A short overview about SEM and the related FIB were included for a complete overview, because both methods were also used for TEM specimen preparation as a dual beam FIB/SEM.

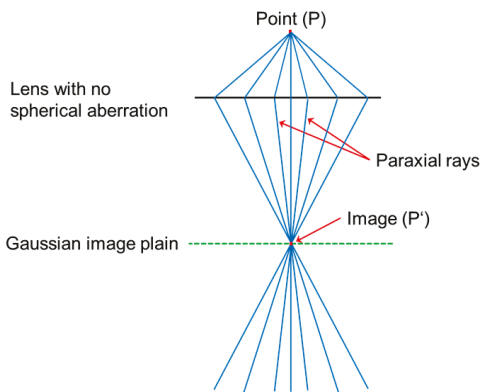
All electron microscopes have in common that they use an electron source to emit electrons and that they are working in vacuum. The electron sources can be thermic sources, field emitting sources or a mixture of both like the Schottky emitter. A vacuum is needed to prevent interactions of beam electrons with the atoms of an atmosphere. High brightness field emitting electron sources are state of the art today. The electrons emitted by the source are then accelerated by a positive voltage. The high energy and therefore small wavelength of the accelerated electrons compared to photons of the visible or ultraviolet light is the main reason to use them for imaging. The resolution σ of a microscope is limited by the Abbe diffraction limit (Abbe, 1873) given by

$$\sigma = 0,61 \cdot \frac{\lambda}{n \cdot \sin(\alpha)} = 0,61 \cdot \frac{\lambda}{NA} \quad (27),$$

where λ is the wavelength, n the refractive index, α the acceptance angle of the lens and NA the numerical aperture. Lenses in light microscopy approach the value of an ideal lens of $NA \approx 1$ and therefore the resolution is finally limited by the wavelength. If magnetic lenses in electron microscopes would be as good as glass lenses in light microscopy, resolutions in the order of the wavelength of 1.97 pm at an acceleration

voltage of 300 kV would be easily possible. The quality of the lenses used in electron microscopes prevents electron microscopes to reach such resolution. Electromagnetic or electrostatic lenses are used to form the electron beam. This is possible because electrons are negatively charged particles. These lenses have the big advantage that their strength can be changed. This makes the beam path of electron microscopes adjustable and therefore highly flexible. The main reasons the theoretical resolutions are not reached are strong aberrations of these electromagnetic lenses (Reimer & Kohl, 2008; Williams & Carter, 2009; Pennycook & Nellist, 2011). These aberration make the magnetic lenses only good for small acceptance angles limiting the reachable resolution (Hawkes, 2009). Otto Scherzer has shown in the “Scherzer Theorem” that round electromagnetic fields used as lenses always suffer from aberrations (Scherzer, 1936). **Figure 15** shows a perfect lens and the effects of the most influential resolution limiting aberration in electron microscopes, the spherical aberration.

A. Perfect lens



B. Spherical aberration

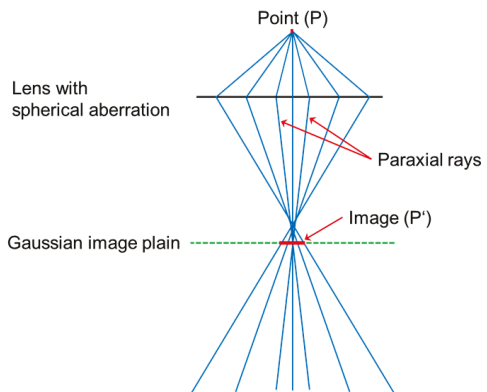


Figure 15: (A) In a perfect aberration free lens all beam rays image a point P in the Gaussian image plain as point P' . (B) Spherical aberration leads to differences in the beam path of the beam rays imaging a point P depending of their distance to the optical axis. Only paraxial rays which are very close to the optical axis meet at the Gaussian image plain correctly. Rays further away from the optical axis have a different focus point leading to blurring of the focus in the Gaussian image plain (Reimer & Kohl, 2008; Williams & Carter, 2009).

Only a perfect aberration free lens can image a point P perfectly focused in the Gaussian image plane as the image point P' (**Figure 15**). A lens suffering from spherical aberration only focuses paraxial beam rays correctly in the Gaussian image plain. Beam rays further away from the optical axis meet at different focus points.

This leads to a blurred image P' of the object point P (**Figure 15**) (Reimer & Kohl, 2008; Williams & Carter, 2009).

Chromatic aberration has the second most influence on resolution. The lens focuses rays of different energy at different focus points. Energy losses of the electron beam rays caused by interaction with the specimen can cause such energy differences. In the Gaussian image plain the image gets consequently blurred (**Figure 16**) (Reimer & Kohl, 2008; Williams & Carter, 2009).

C. Chromatic aberration

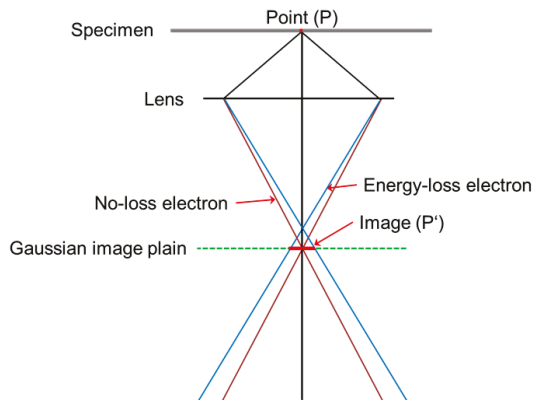


Figure 16: Depending on the energy loss of the electrons transmitting the specimen, the electron beam rays have different focus points. This leads to blurring of the focus in the Gaussian image plane (Reimer & Kohl, 2008; Williams & Carter, 2009).

By using multipole lens systems it is possible to compensate the effects of spherical and chromatic aberration. The multiple pole lens systems generate aberrations that invert the aberrations of the resolution limiting lens. The important invention of the first working aberration correctors has led to a big improvement in resolution of electron microscopes especially in the field of TEM (Haider et al., 1998). Aberration correctors nowadays are even implemented in smaller electron microscopes like SEMs (Zach & Haider, 1995). Additionally the use of energy filters and monochromators can reduce the amount of chromatic aberration (Reimer & Kohl, 2008; Williams & Carter, 2009). Aberration correctors are still fairly expensive so there will be probably a long time period of coexistence of uncorrected and corrected electron microscopes.

Astigmatism is another aberration that occurs if the magnetic lens is not perfectly round. The result is an elliptic electron beam. Astigmatism was one of the major

resolution limiting aberrations in the beginning of electron microscopy, caused by limits in manufacturing precision of the magnetic lenses. In the 1960s the first commercial stigmators were available. They correct the elliptical shape of the electron beam by one or two multipole lenses, like a quadrupole. Stigmators are common elements in most electron microscopes. Higher orders of astigmatism, which cannot be resolved by stigmators alone, can be corrected by modern aberration correctors (Orloff, 1997; Reimer & Kohl, 2008; Williams & Carter, 2009).

6.1.1 Electron interaction with matter

Electron microscopes are using the signals created by the interaction between an electron beam of accelerated electrons and the investigated specimen. The interaction of the shell electrons and the nucleus of the specimen atoms with the electron beam produce various signals. **Figure 17** shows the main signals that are used for imaging or spectroscopy in electron microscopes.

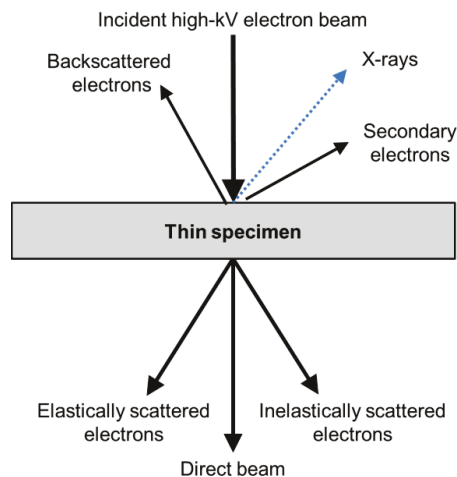


Figure 17: Shown is a schematic drawing of the produced signals that are mainly used for electron microscopy, of an electron beam interacting with a thin specimen.

Secondary electrons are the main signals for imaging in a SEM. Secondary electrons are outer shell or valence band electrons of the sample atoms that get transferred enough energy from interaction with the incoming electron beam or from high energetic backscattered electrons to leave the atom (**Figure 18**). Their energies reach up to 50 eV. Secondary electrons can only leave the sample, if they are created close enough to the surface of the sample. They are the signal of choice for topological imaging in SEMs (Reimer, 1998; Goldstein, 2007).

Backscattered electrons are elastically scattered or reflected electrons of the incident electron beam. They have a similar high energy as the incident electron beam, depending on the acceleration voltage. The backscattered electrons are produced by elastic interactions with nuclei of the sample atoms (**Figure 18**). The amount of backscattered electrons increases with increasing atomic number, which can be used to distinguish chemically different sample regions for example in a SEM (Reimer, 1998; Goldstein, 2007).

If the sample is thin enough, that the largest portion of the electron beam can transmit the sample, then TEM and STEM is possible. The transmitting electrons are either elastically scattered, inelastically scattered or transmitted unaffected by the sample. Scattered electrons can be either coherent or incoherent. The various interactions of the electrons produce different amounts of energy losses (**Chapter 6.2**).

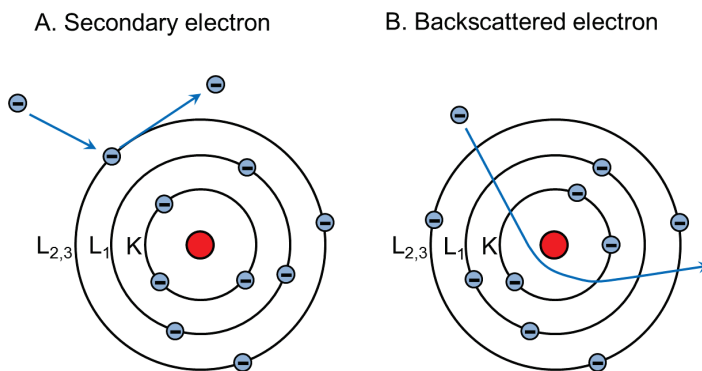


Figure 18: Shown are the schematic drawings of the creation of secondary electrons (A) and backscattered electrons (B). Secondary electrons are leaving their shell after energy transfer from a high energetic electron. Backscattered electrons are high energetic electrons that get scattered back by the nuclei of the sample atoms.

The main part of the electron beam transmits with almost no energy loss through a thin TEM specimen. Plasmon excitations in the specimen and the ionization of specimen atoms can decrease the energy of interacting electrons. Elastically scattered electrons lose almost no energy while energy losses are typical for inelastic scattering processes (Reimer & Kohl, 2008; Williams & Carter, 2009). Depending on the used TEM/STEM detectors and the TEM/STEM lens configuration signals are recorded and used in different ways. This leads to a variety of TEM and STEM methods.

X-ray radiation is emitted by the sample, if an electron is missing in a lower energy shell. This can be for example the case if a lower energy shell electron gets enough energy from an electron of the incident beam to leave the atom. The missing electron is replaced by an electron of a higher energy shell. This process emits a characteristic X-ray photon of corresponding energy (**Figure 19**). The energy of characteristic X-ray radiation is element specific and can be used for chemical analytics. If electrons are deflected by the influence of the positively charged nucleus, continuous X-rays are emitted. The emitted X-ray photon energy equals the decreased kinetic energy of the traveling electron after the interaction. Continuous X-rays produce an underground noise in chemical X-ray analysis. The X-ray signal can be recorded in TEM, STEM and SEM with suited detectors (Reimer, 1998; Goldstein, 2007; Reimer & Kohl, 2008; Williams & Carter, 2009).

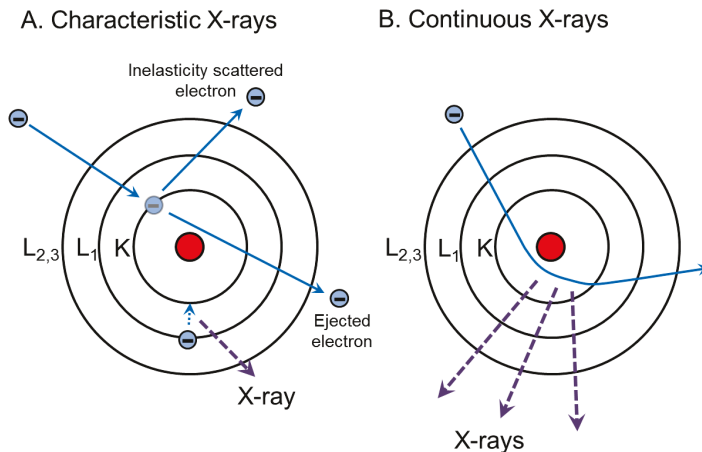


Figure 19: Shown are the schematic drawings of the production of characteristic X-rays (A) and continuous X-rays (B). A characteristic X-ray is emitted when a higher energetic shell electron takes a free lower energetic shell position of an ejected orbital electron. Continuous X-rays are emitted when an electron is deflected from the coulomb force of the nucleus.

6.1.2 Scanning electron microscopes

A SEM mainly uses secondary electrons and backscattered electrons for imaging. The used signals are created by an electron probe focused onto a sample. Typical working values of a SEM are acceleration voltages between 0.1 kV – 30 kV and currents between 10^{-8} A - 10^{-12} A. Higher voltages expand the activated volume the signal is coming from and therefore decrease the possible resolution. The images of a SEM are created digitally pixel by pixel by scanning the focused electron probe

over the sample surface (Reimer, 1998; Goldstein, 2007). **Figure 20** shows a typical schematic drawing of a SEM setup.

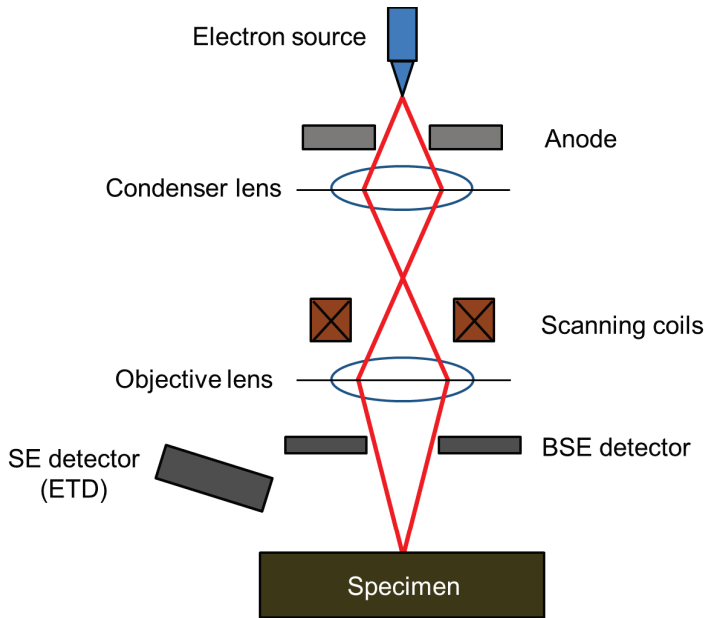


Figure 20: Shown is the principle of a SEM setup.

SEM is a good method to image topographies because the signal is created only a few nanometers into the surface. The actual depth depends on the used acceleration voltage. The most common detectors in SEM for secondary electron detection are Everhart Thornley Detectors (ETD). An ETD is constructed out of a faraday cup that can have a different potential relative to the sample and a scintillator inside. The potential of the faraday cup relative to the sample is important for the selection of the energy of the electrons that should be detected. The scintillator converts them into photons. Then the signal of the photons can be increased in a photo amplifier. Also in lens or through the lens detectors (TLD) are widely used today for secondary electrons. They are often semiconductor type detectors which count the charge of the collected electrons. The TLDs got their name from the location they are built in, which is the pole piece of the electron beam column. TLDs are more effective on smaller working distances than ETDs. Backscattered electrons are detected by doughnut shape arrangements of detectors around the optical axis to maximize the collection angle. They can be scintillator or semiconductor type detectors (Reimer, 1998; Goldstein, 2007).

6.1.3 Focused ion beam and dual-beam FIB

In this work a Helios dual beam FIB/SEM system from FEI was used. It is a combination of a SEM column and FIB column in one machine. The FIB and the dual beam FIB/SEM are described here because of their close relationship to SEM. Dual beam FIB/SEM is a state of the art method for TEM specimen preparation. The main difference of a FIB to a SEM system is the use of charged ions instead of electrons to form a beam. Gallium ions are used for FIB in the Helios dual beam FIB/SEM. Gallium is a good material for liquid ion sources because of low melting point, low volatility at melting point, its viscous behaviour, its low vacuum pressure, its good emission characteristics and good mechanical, electrical and vacuum properties (Giannuzzi, 2005). In the liquid gallium source the gallium in a reservoir is heated and can flow down a tungsten needle. An electric field pulls gallium ions from the tip of the tungsten needle. The gallium ions are then accelerated by an acceleration voltage. A schematic drawing of a liquid gallium source is shown in **Figure 21**.

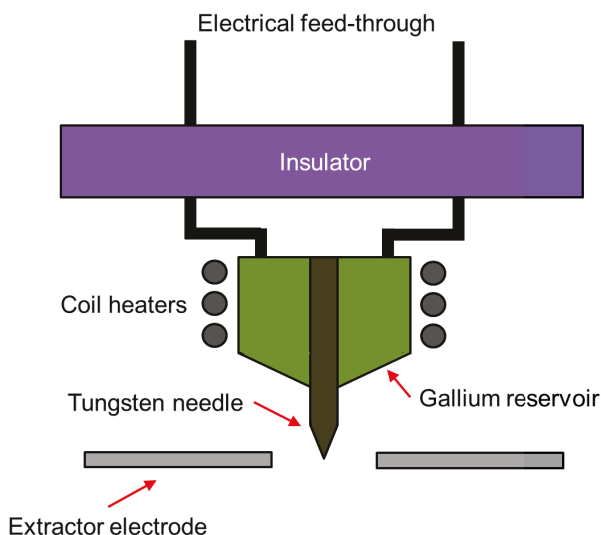


Figure 21: Shown is a schematic drawing of a liquid gallium FIB source.

The extracted and accelerated beam of ions is formed and focused on the sample similar to a SEM by electrostatic lens systems. This focused ion beam is then scanned over the sample. Because of the higher mass of the gallium ions in comparison to electrons there is a stronger interaction of the ions with the irradiated material. This is used for material manipulation on the nanometer scale. It is possible

to cut into samples or to deposit materials, like platinum or wolfram, by cracking precursor gases at the sample surface (Giannuzzi, 2005). To sputter away material by ion milling, the accelerated high energetic gallium ions transfer energy to sample atoms through collisions. If the energy is high enough they leave the sample surface. Atoms leaving the sample are redeposited in the chamber or are pumped away. Gallium atoms can implant in the sample surface leading to defect structures. This defect structures and knocked off atoms can lead to an amorphous surface of several nanometers. The amorphisation of the surface can be reduced by using lower acceleration voltages in the final milling processes. A schematic drawing of ion milling in the FIB is shown in **Figure 22**.

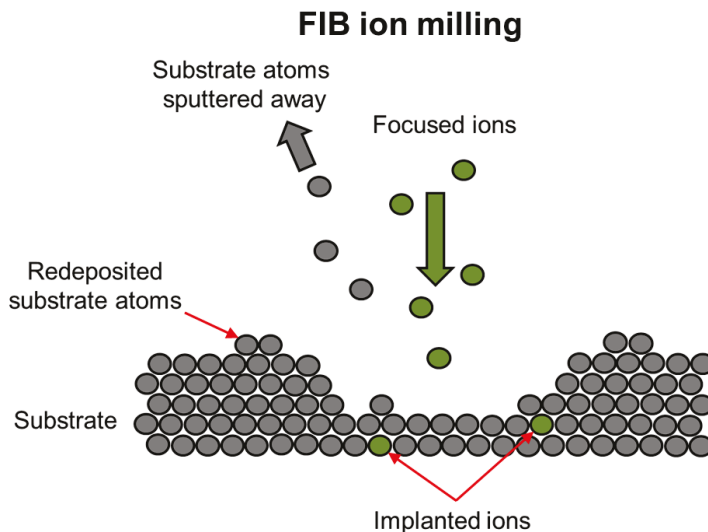


Figure 22: Shown is a schematic drawing of the process of sputtering away material of the sample with the focused gallium ions. The high energetic gallium ions transfer enough energy to the sample atoms to leave the sample surface. Some of these atoms redeposit on a different location on the sample. Some of the gallium ions also implant themselves into the sample.

Precursor gases are used for the deposition of materials in the FIB. These precursor gases are a chemical compound of the deposition metal and a volatile species. The precursor gas is injected by a small needle shaped gas inlet close to the surface (**Figure 24**). The gallium ions crack the precursor gas. The metal is then deposited on the sample surface while the volatile species is pumped away. The deposited layers can be contaminated by implanted gallium and remains of the other precursor

gas species. A schematic drawing of the deposition process in the FIB is shown in **Figure 23**.

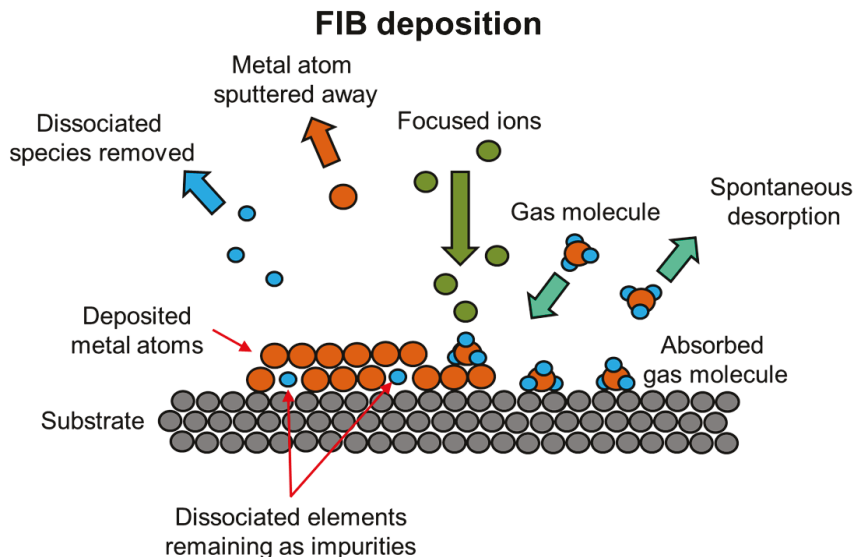


Figure 23: Shown is a schematic drawing of metal deposition by cracking a precursor gas with gallium ions. The gallium ions crack the precursor gas into the metal atoms and a volatile species. The metal ions are deposited on the sample surface while the volatile species is pumped away.

The interaction of the ions with the sample creates secondary electrons that can be used for imaging. The operator of a FIB always has to be careful to irradiate the sample as low as possible by the ion beam for imaging. Therefore the optimal acceleration voltages and currents of the ion beam chosen for the performed task are extremely important (Giannuzzi, 2005).

Already mentioned were dual beam FIB/SEM systems of combined SEM and FIB columns. In the dual beam FIB/SEM the SEM and the FIB column are placed in an angle to each other. In the Helios dual beam FIB/SEM from FEI the angle between both columns is 52° and the SEM column is placed vertically in the system. Both columns share the same eucentric height. That makes it possible to image or manipulate a location on the sample serially or simultaneously with FIB and SEM. A scheme of a dual beam FIB/SEM is shown in **Figure 24**. Through this combination, the usefulness of the FIB as a specimen preparation tool is combined with the much more gentle imaging of the SEM. The angle between FIB and SEM is also advantageous for preparing cross section lamellas for TEM. The region of interest of

the cross section can be controlled in the manufacturing process by SEM while the FIB mills the lamella thinner.

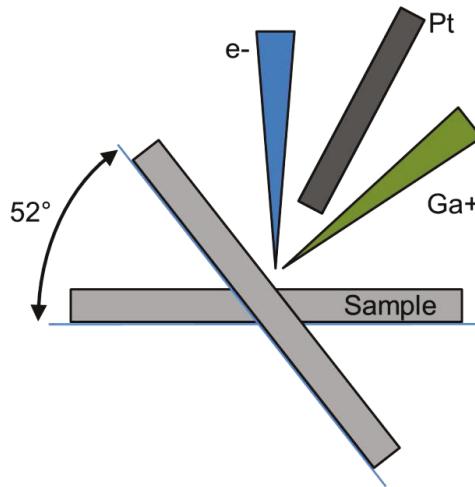


Figure 24: Shown is a schematic drawing of the dual beam FIB/SEM with a 52° angle between SEM and the FIB column. Also shown is a possible location of an inserted gas inlet for a platinum rich precursor gas for deposition.

The electron beam of the SEM can also be used for the deposition of very fine structures or small layers of material by cracking the precursor gases available in dual beam FIB/SEM setups. This can be used to protect the region of interest from damage of the high energetic ions even before FIB preparation starts (Giannuzzi, 2005).

6.1.4 Transmission electron microscopes

TEMs are working with high acceleration voltages usually between 80 – 300 kV. Higher acceleration voltages lead to higher mean free paths of the accelerated electrons in the sample which are crucial for the transmission through the very thin specimen. TEM specimens are usually thinner than 100 nm. The optimal thickness of a TEM sample depends on the material properties, especially its atomic number and density. With higher acceleration voltages the resolution increases because of the decreasing wavelength of the electrons, but in the end aberrations of the magnetic lenses are the limiting factors of resolution in TEM (Reimer & Kohl, 2008; Hawkes, 2009; Williams & Carter, 2009). In this work an uncorrected Tecnai from FEI with 200 kV was used for TEM bright field imaging. **Figure 25** shows a schematic drawing of the beam path of an uncorrected TEM.

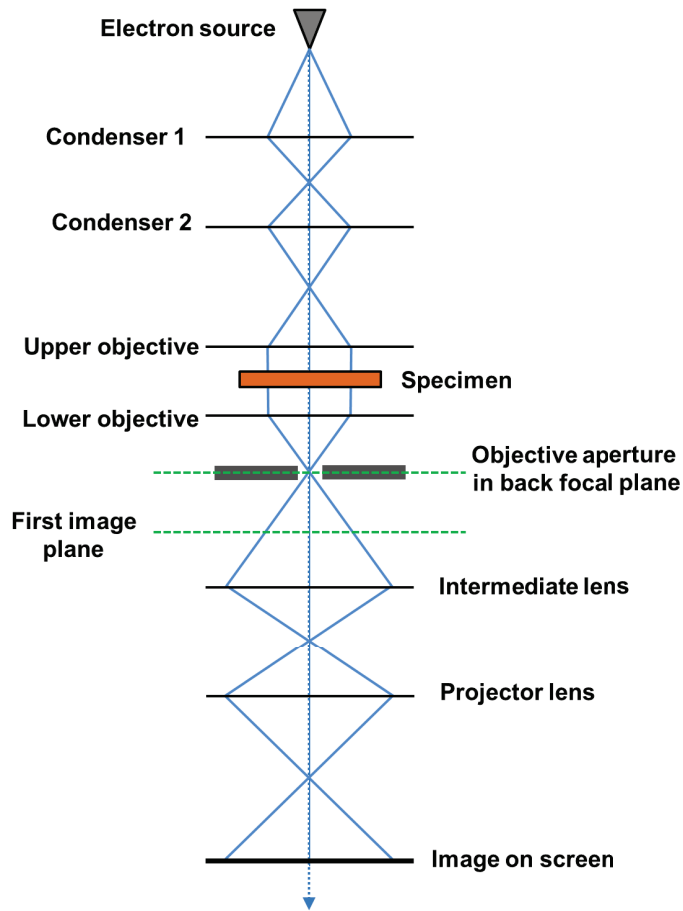


Figure 25: Shown is the schematic beam path of an uncorrected TEM.

The condenser lens system, together with the upper objective, creates a highly demagnified image of the source. This virtual source is used for a parallel and coherent illumination of a region of interest of the specimen. The image of the specimen is magnified by the lower objective. The objective lens is the resolution limiting lens. Aberrations are worst at high angles and the objective has to manage the widest range of angles in the TEM. The projection lens system, including the intermediate lens and additional projector lenses, magnify the image of the objective lens to a chosen magnification. The image is then projected on a fluorescent screen, or recorded by a camera. Most TEM cameras today are using charged coupled devices chips (CCD-Chips). (Reimer & Kohl, 2008; Williams & Carter, 2009).

6.1.4.1 TEM bright field imaging

For TEM bright field imaging, an uncorrected Tecnai from FEI operating at 200 kV was used. In TEM bright field imaging the specimen is illuminated with a parallel and coherent beam. The objective aperture, located in the back focal plane of the TEM below the specimen, is used to filter out the part of the beam that is scattered to sufficiently high angles to hit the objective aperture. The parts of the specimen that scatter the beam to high enough angles will appear dark in the images. The parts of the specimen that do not scatter the electron beam at all or do not scatter the electron beam to high enough angles will appear bright. (Reimer & Kohl, 2008; Williams & Carter, 2009).

The beam can be scattered for different reasons. In crystalline materials Bragg diffraction gives rise to contrast that is strongly dependent on the orientation of the crystalline parts of the specimen. The coherent electron beam is diffracted constructively at the atom lattices for conditions that satisfy Bragg's law (**Figure 26**) (Reimer & Kohl, 2008; Williams & Carter, 2009).

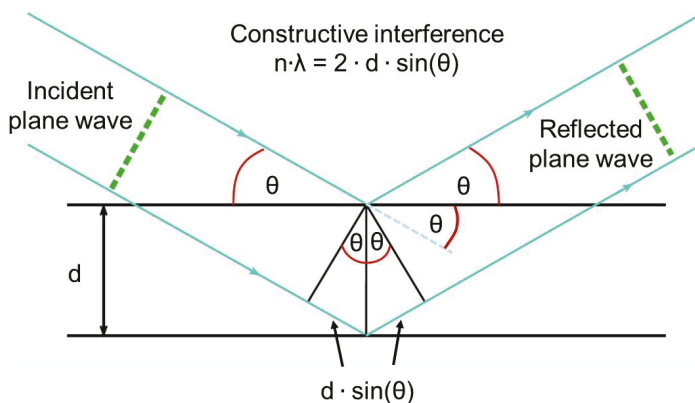


Figure 26: If the incident plane wave satisfies Bragg's law the wave is reflected constructively.

In this case, the electrons are diffracted elastically. The diffracted beams form a diffraction pattern in the back focal plane consisting of diffraction spots or discs. The objective aperture is used to filter out the diffracted beams to produce the Bragg diffraction contrast (**Figure 27**). Bragg diffraction contrast in bright field images can be distinguished from other scattering contrasts by tilting of the specimen, which

changes the Bragg diffraction contrast significantly depending on orientation of the crystals (Reimer & Kohl, 2008; Williams & Carter, 2009).

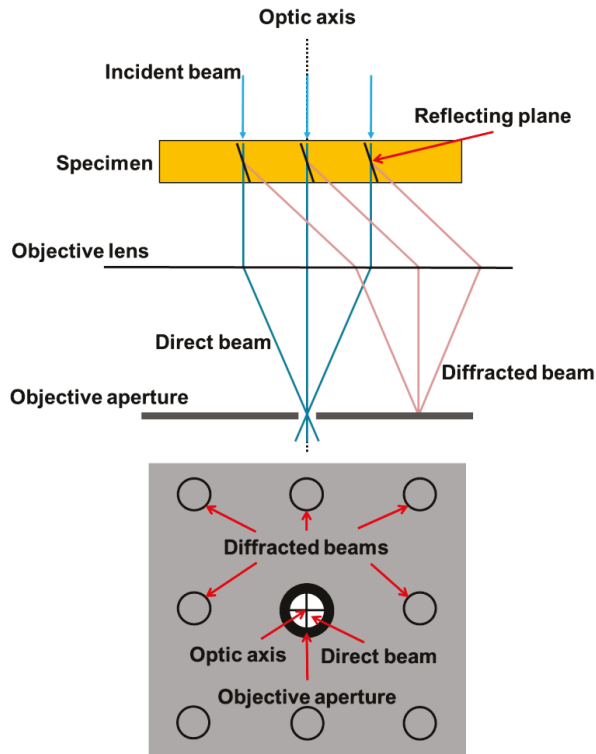


Figure 27: Shown is the working principle of the Bragg diffraction contrast in bright field images. Diffracted beams forming a diffraction pattern in the back focal plane are filtered out by the objective aperture.

Bending contours are results of bending of thin crystalline specimens or intrinsic bended crystals in specimens. The results are bended single crystalline regions. The atom lattices of the single crystalline regions bend in and out of the Bragg condition, which gives rise to dark or bright features (Williams & Carter, 2009). Bending contours can be used for the understanding of materials, as for example the characterization of trans-rotational crystals (Kolosoov, 2008).

Thickness differences, density differences and differences in the atomic number are the main reason for scattering contrast besides Bragg diffraction. High atomic number elements, thicker specimen regions and denser specimen regions scatter more electrons. These regions appear darker because more electrons are filtered out by the objective aperture. Therefore, this contrast is called mass thickness contrast. A smaller objective aperture will result in more contrast of the acquired images,

because even electrons scattered to lower angles are blocked out. On the other hand the overall intensity of the image decreases by decreasing the size of the objective aperture (Figure 28)(Williams & Carter, 2009).

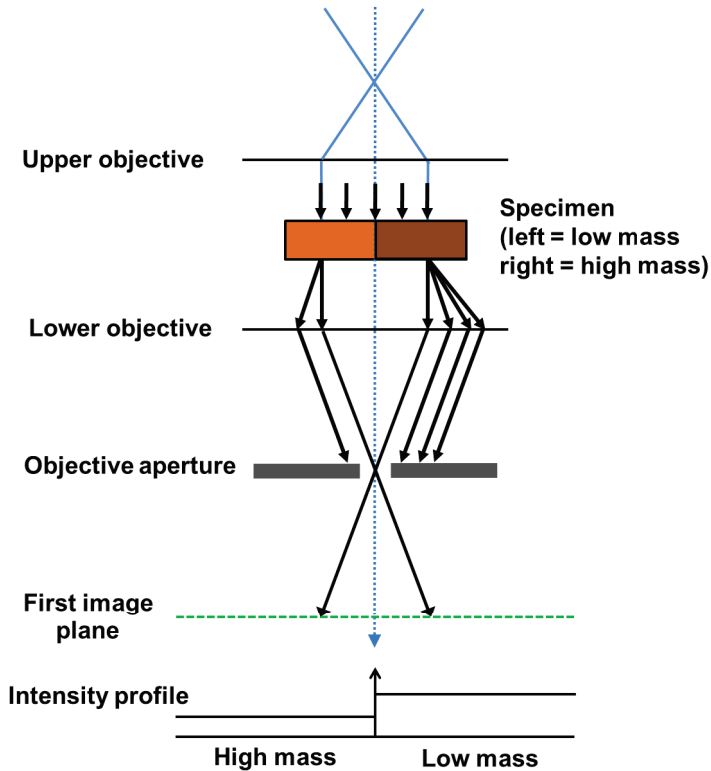


Figure 28: Shown is the working principle of the mass thickness contrast in bright field images. Thicker specimen regions or specimen regions with elements of higher atomic number scatter more electrons, which are filtered out by the objective aperture. Consequently these regions appear darker in the image, which is shown by the intensity profile.

6.1.4.2 High resolution transmission electron microscopy

High resolution transmission electron microscopy (HRTEM) images are produced by coherent interference of the incident beam and the diffracted beams. The intensity distribution in the image plane is given by $|\psi_i(r)|^2$, where $\psi_i(r)$ is the image plane wave function and r is a position vector in real space. The image plane wave function is a convolution of the exit plane wave function $\psi(r)$ after leaving the specimen and a point spread function $T(r)$.

$$\psi_i(r) = \psi(r) \otimes T(r) \quad (28).$$

$\psi(r)$ is the exit wave function and contains the information about the influence of the atom configuration on the incident electron wave function of the electron beam. This means it encodes the structural information about the specimen. The point spread function describes the influence of the microscope on the image. An ideal TEM would perfectly transfer the information of $\psi(r)$ to the image plane. In this case $\psi_i(r)$ and $\psi(r)$ would be equal. In real life $T(r)$ blurs the image in the image plane. The image plane function in reciprocal space located in the back focal plane is given by the Fourier transformation of $\psi_i(r)$. In reciprocal space the convolution of $\psi(r)$ and $T(r)$ can be expressed as a multiplication of their Fourier transformations.

$$\psi_i(q) = F[\psi_i(r)] = F[\psi(r) \otimes T(r)] = F[\psi(r)] \cdot F[T(r)] = \psi(q) \cdot T(q) \quad (29),$$

where q is a reciprocal position vector. $T(q)$ is known as the microscope transfer function. The components of $T(q)$ are the aperture function $A(q)$, the envelope function $E(q)$ and the aberration function $B(q)$.

$$T(q) = A(q) \cdot E(q) \cdot B(q) \quad (30).$$

$A(q)$ describes which beams are allowed to contribute to the image additional to the primary beam by interference. This is selected by the physical size of the objective aperture. Beams that can pass the hole of the aperture contribute to the image formation. The other beams are filtered out. $E(q)$ describes the information limit given by the damping of the wave function. $E(q)$ is a complex function, but mainly defined by the limits given by chromatic aberration and spatial coherence. $B(q)$ describes the influences of the lens aberrations and is defined as:

$$B(q) = \exp(i\chi(q)) \quad (31),$$

where $\chi(q)$ for an TEM without aberration correction can be defined as:

$$\chi(q) = \pi \cdot \Delta f \cdot \lambda \cdot q^2 + \frac{1}{2} \cdot \pi \cdot C_s \cdot \lambda^3 \cdot q^4 \quad (32),$$

where Δf is the defocus, λ is the electron wavelength and C_s is the spherical aberration coefficient. Further detail of the topic of HRTEM can be found in literature (De Graef, 2003; Reimer & Kohl, 2008; Williams & Carter, 2009).

6.1.5 Scanning transmission electron microscopes

STEM combines the principles of SEM and TEM. The specimens have similar specifications as for TEM. Usually in STEM the electron beam is a smallest possible

probe on the specimen to reach highest possible resolutions. This is done by the condenser lenses and the upper part of the objective lens above the specimen. STEMs are suffering from the same problems of aberrations of the magnetic lenses like all electron microscopes (Hawkes, 2009). In this work a spherical aberration probe corrected Titan dedicated to STEM from FEI at 200 kV was used to reach atom resolution (Kovacs et al., 2016). Resolutions up to around 50 pm at 300 kV in spherical aberration corrected STEM machines are possible (Day, 2009; Barthel et al., 2015; Jeol, 2016). For most methods a convergent electron probe is used to reach the smallest probe sizes. Special STEM methods like NAED use an almost parallel coherent beam in the 1 nm-10 nm size range. For NAED we used a Titan from FEI dedicated to STEM at 300 kV (Pennycook & Nellist, 2011; Heggen et al., 2016). By scanning over the sample like in a SEM a digital image is formed pixel by pixel by the gathered signal depending on the used detectors. **Figure 29** shows the simplified schematic drawing of an uncorrected STEM and some of the annular detectors. The Titans of FEI have an additional condenser lens and a probe corrector is mounted between the last condenser lens (C3) and the objective lens.

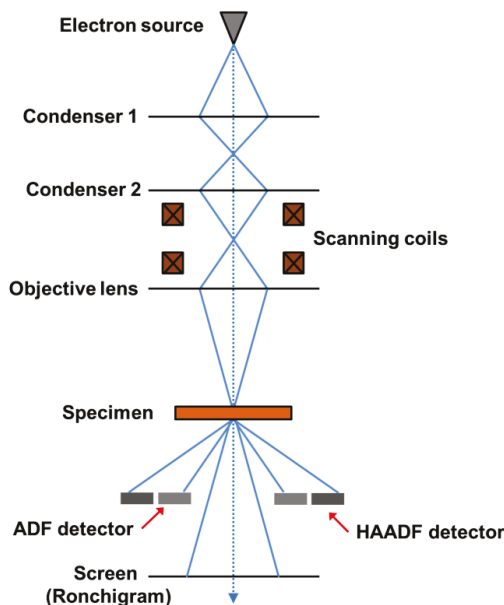


Figure 29: Shown is the scheme of an uncorrected STEM.

6.1.5.1 STEM annular dark field imaging

Annular detectors located after the specimen are used to collect the signal of the electrons that are diffracted or scattered by the specimen (**Figure 29**). The ADF detector collects primarily the signal of electrons which were diffracted at crystalline lattices. An annular detector, which is far away from the optical axes, detects only electrons deflected by thermal diffuse scattering (TDS). Therefore, it excludes all unwanted effects of coherent influences. This electron signal is predominantly caused by the thermal vibration of the atoms. Thicker and denser materials or materials with higher atomic number scatter the beam stronger which increases the signal. Therefore, this contrast mechanism is called Z-contrast. The acquired images are called high angle annular dark field (HAADF) images. **Figure 30** shows a schematic drawing of possible locations of the annular detectors in STEM. When the annular detectors are used for the creation of dark field images, those areas appear brighter, which scatter the electrons strongly to high enough angles. Regions, which do not scatter the electron beam strongly, appear darker. The sensitivity of HAADF to the Z-contrast is very useful for sample analysis. It can help judge thickness or density gradients or find regions of heavier or lighter elements in the specimen (Pennycook & Nellist, 2011).

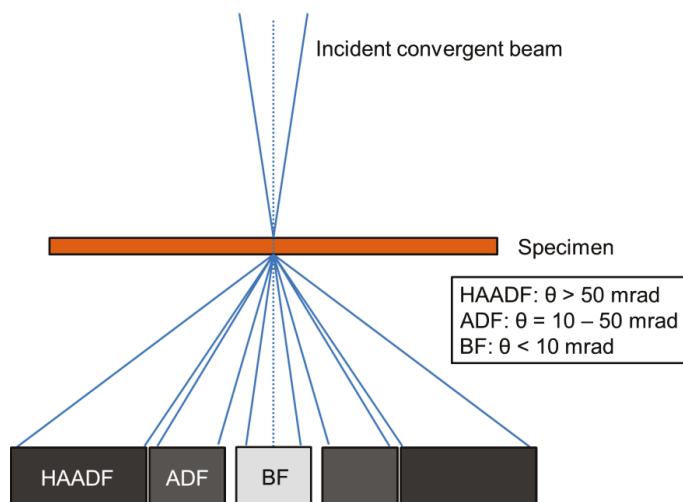


Figure 30: Shown is a scheme of possible locations of different STEM detectors and the angular relationships to the imaged signals.

6.1.5.2 Nano area electron diffraction in STEM

In STEM a coherent and almost parallel 1 nm-10 nm sized probe can be used to scan the specimen. Then a diffraction pattern, of the probed spot, can be acquired on a suitable detector. In this work a CCD was used to record the diffraction patterns. The area of a thin specimen attributing to the diffraction pattern has a similar size as the electron probe. Therefore this diffraction method has a spatial resolution directly given by the chosen probe size and is called nano area electron diffraction (NAED). A smaller probe size increases the spatial resolution of the ADF STEM images. Smaller probes are also decreasing the contributing area to a single NAED pattern. On the other hand smaller probes for the most part require an increase in the convergence angle. The increase in convergence angle leads to bigger diffraction discs in the diffraction patterns, which can result in losing spatial resolution in the reciprocal space. The convergence angle should be small enough that the diffraction discs are not overlapping in the diffraction patterns (Pennycook & Nellist, 2011).

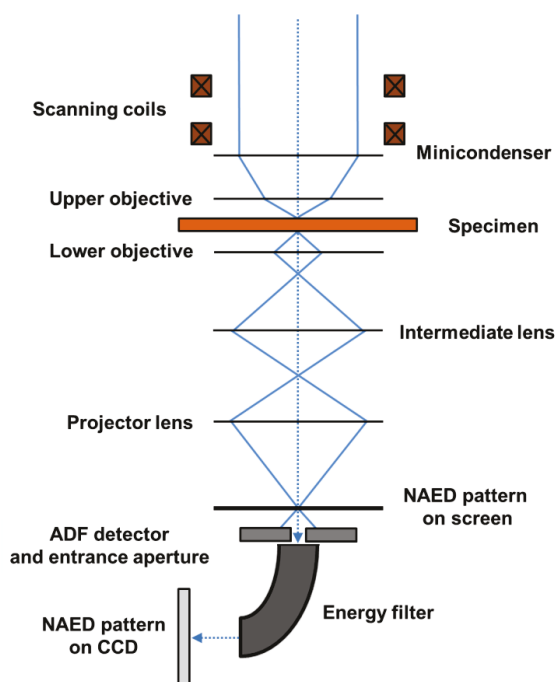


Figure 31: Shown is the STEM arrangement for acquiring NAED patterns. NAED patterns require small convergence angles (convergence in scheme is exaggerated). The NAED patterns can be viewed on the fluorescence screen or recorded on a CCD. Also the detector mounted on the entrance aperture of the energy filter can be used to record the ADF signal.

A schematic drawing of the STEM setup to acquire NAED patterns is given in **Figure 31**. The advantage of the shown detector arrangement in **Figure 31** is the possibility to acquire ADF images at the same time by a detector mounted to the entrance aperture of the energy filter as using the CCD for the collection of diffraction patterns. The NAED patterns give information if the material is crystalline or amorphous. NAED probes mostly produce single crystalline diffraction patterns, because only a nanometer sized area of the crystalline material is probed on this length scales. Only nanocrystalline regions or thin films combine to a mixture of single crystalline diffraction patterns. NAED patterns of crystalline materials formed by the long range order show a pattern made out of discs that can be indexed and analyzed. They contain information about lattice parameters and symmetry. Amorphous materials show rings of speckled intensity that are lacking long range order information and have to be tackled by other analysis approaches like FEM (Pennycook & Nellist, 2011).

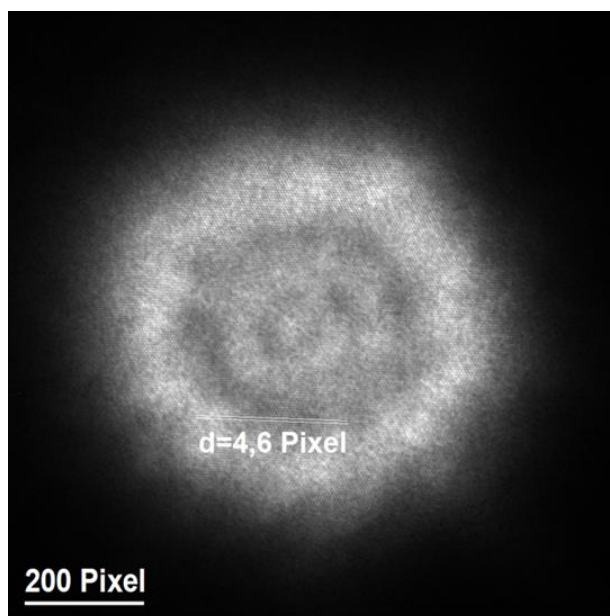


Figure 32: Shown is the CCD Calibration by a HRTEM image of the spreaded electron probe looking at Si along the [111] direction. In the example the $(\bar{2}02)$ lattice plane spacing d is measured in pixel to calculate the calibration factor.

In this work for NAED the microprobe mode of a 300 kV Titan dedicated for STEM of FEI was used with a 10 μm C2 aperture. The CCD is calibrated in real space by

HRTEM images of Silicon viewed along the [111], [110] or [100] directions (**Figure 32** and **Figure 33**). The calibration images are taken with a weakened C3 lens to spread the probe and decrease the intensity on the CCD. The good coherence of the probe leads to interference rings of different intensity in the probe (**Figure 32**). The calibration factor F_{real} of the CCD images in real space is then calculated by dividing the known lattice plane spacing from literature d_{lit} by the measured lattice plane spacing d_{meas} :

$$F_{\text{real}} = \frac{d_{\text{lit}}}{d_{\text{meas}}} \quad (33).$$

As an example in **Figure 33** the HRTEM image of Si is shown, which is viewed along the [111] direction. The lattice plane spacing of the $(\bar{2}02)$ lattice planes was measured in pixel. From this F_{real} was calculated.

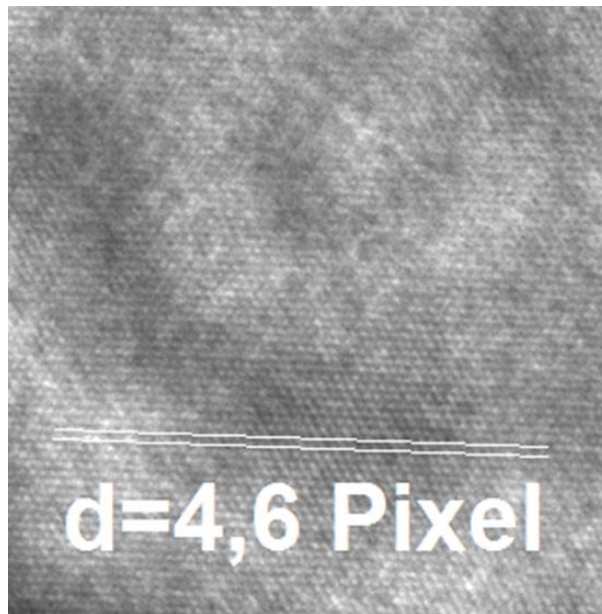


Figure 33: Shown is the magnification of the HRTEM image of the spreaded probe in **Figure 32** viewed at Si along the [111] direction. In the example the $(\bar{2}02)$ lattice plane spacing d is measured in pixel to calculate the calibration factor.

We use the definition of the probe size as the full width half maximum (FWHM) of the focused probe intensity profile on the CCD (**Figure 34**) (Williams & Carter, 2009; Pennycook & Nellist, 2011). The image of the probe with focused C3 lens in vacuum is then recorded on the calibrated CCD and the FWHM of the intensity profile is

measured. The determined probe size is between 1.8 nm-2 nm with a 10 μm C2 aperture (**Figure 34**).

The CCD is calibrated for imaging in reciprocal space by diffraction patterns taken from Silicon in [111], [110] or [100] direction (**Figure 35**). The calibration factor F_{rec} of the CCD images in reciprocal space is calculated by dividing the known reciprocal lattice plane spacing from literature d^*_{lit} by the measured reciprocal lattice plane spacing d^*_{meas} :

$$F_{rec} = \frac{d^*_{lit}}{d^*_{meas}} \quad (34).$$

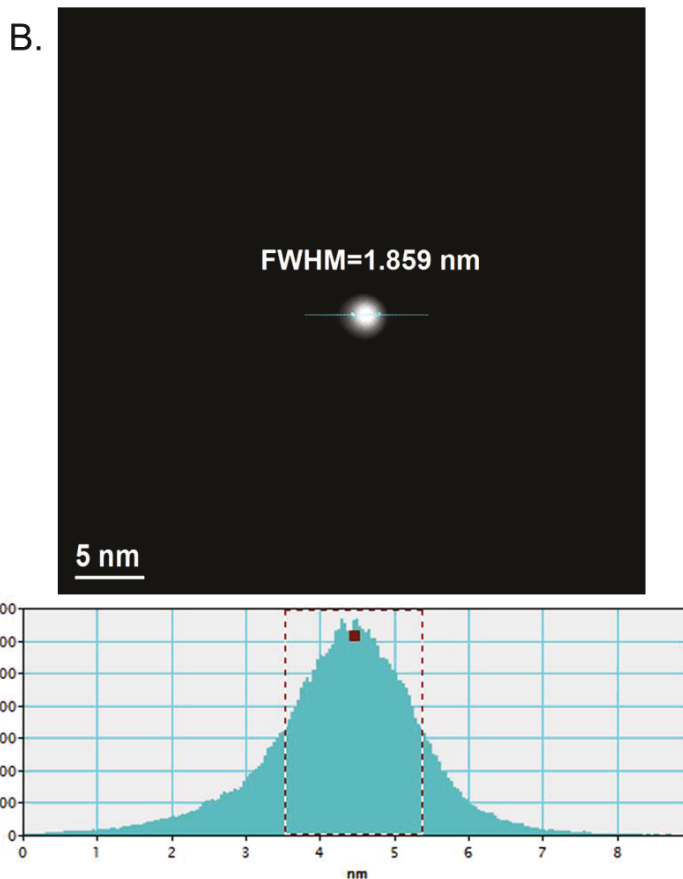


Figure 34: The size of the FWHM of the focused probe used for NAED can be measured after the calibration through the HRTEM images.

From the calibrated Si diffraction pattern the semi convergence angle α can be determined by (Williams & Carter, 2009):

$$2 \cdot \alpha = 2 \cdot \theta_B \cdot \frac{a}{b} \quad (35),$$

where $2 \cdot \theta_B$ is the Bragg angle of a chosen (hkl) lattice plane, a the diameter of the (000) diffraction spot and b the distance of the (000) spot to the next diffraction spot of the chosen (hkl) lattice plane (**Figure 35**).

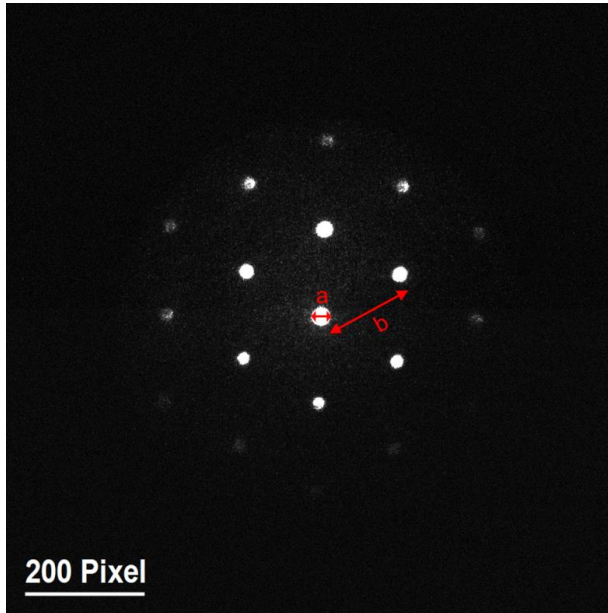


Figure 35: NAED pattern of Si viewed along the [111] direction for calibration of the CCD images in reciprocal space. Also shown are the distances used for the calculation of the convergence angle.

The probe size can also be approximated by the Abbe criterion (Abbe, 1873; Yi et al., 2010; Pennycook & Nellist, 2011)

$$\text{Probe size} = \frac{0.61 \cdot \lambda}{\alpha} \quad (36),$$

where λ is the wavelength of the electrons. From the diffraction patterns of Si, viewed along the [111] direction, a semi convergence angle of 0.44 mrad is calculated. The approximated probe size is then 2.7 nm. The approximated value is bigger than the measured FWHM value of 1.9 nm, but both values are in the aimed few nanometer range of NAED. Probe setups, which were similar to the shown example, were used for all NAED methods in this work. For all experiments the probe current (50 pA - 80 pA) was kept as constant as possible through adjustment of the focus of the built in monochromator.

6.1.5.3 Fluctuation electron microscopy in STEM

The NAED can be used to get information about the MRO of nanocrystalline or amorphous materials. This is possible by calculating the variance of the diffracted intensity in relation to the position in reciprocal space of a statistical amount of NAED patterns (normally more than 500 patterns) acquired by scanning the specimen by the electron probe. **Figure 36** shows a schematic drawing of the acquisition process of the NAED patterns for FEM.

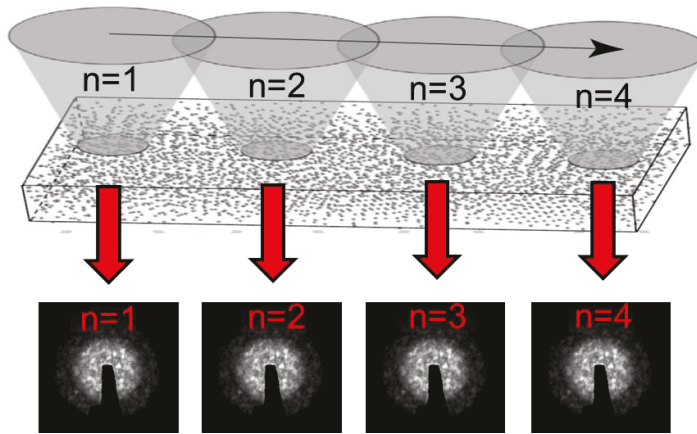


Figure 36: In FEM an electron probe scans over a sample acquiring a NAED pattern at every chosen spot. Higher order correlations of the atoms in the thin sample lead to intensity fluctuations in the NAED patterns.

Every NAED pattern of the scanned regions is radially averaged to get an intensity profile in reciprocal space. The normalized variance V of the material is then calculated from every intensity profile by the equation

$$V(k,Q) = \frac{\langle I^2(k,Q) \rangle}{\langle I(k,Q) \rangle^2} - 1 \quad (37),$$

where k is the scattering vector, Q is the reciprocal space resolution, $I(k,Q)$ is the measured intensity, and $\langle \rangle$ indicates averaging over positions on the specimen. This method is called fluctuation electron microscopy (FEM) in STEM (Voyles & Muller, 2002). From now on it will be called simply FEM in this work. For the calculation of the variance from the acquired NAED patterns we used a by us modified version of the freely available MATLAB script from P. Voyles and M. Burton (Voyles & Burton, 2014). The variance of a material measures the MRO. The MRO is in the length scale of a few nanometers. This is the same length scale as atom clusters forming subcritical nuclei, stable nuclei or nanocrystals. The variance

measures the MRO because it is sensitive to third, fourth and higher order correlations of the atomic arrangement. Normal diffraction is only sensitive to second order correlation and is not sensitive to the MRO (Treacy & Gibson, 1996; Voyles & Muller, 2002; Treacy et al., 2005). The variance signal is related to the probe size of the electron beam. The variance signal is the highest, if the probe size is similar to the probed cluster sizes. This relation makes it possible to determine cluster sizes by performing FEM with various probe sizes on the same material and comparing the amplitude of the variance (Hwang & Voyles, 2011). In the present work, all FEM measurements were done with similar probes of sizes around 2 nm. The variance signal is also influenced by the current in the probe (Hwang & Voyles, 2011). To produce comparable data, the probe current was kept at similar values (50 pA - 80 pA) adjusting the focus of the built-in monochromator of the Titan instrument. The thickness of the analysed specimens is also very important. The specimen should be thin enough so that the beam is not diffracted multiple times. Therefore the thickness should be below the mean free path of the electrons for elastic scattering at the given accelerating voltage (Voyles & Muller, 2002). The thickness differences of the scanned specimen regions influence the variance signal. If the thickness varies, this leads to a decrease of the variance (Hwang & Voyles, 2011). This is an especially important issue if lamellas produced by FIB are used. While the FIB is a very good tool to make thin specimens, the thickness over the range of one specimen or the thickness of several lamellas can vary. This can make the comparison and interpretation of variance plots challenging. In the following a correction procedure is presented that produces comparable FEM variance plots of specimens of the same material.

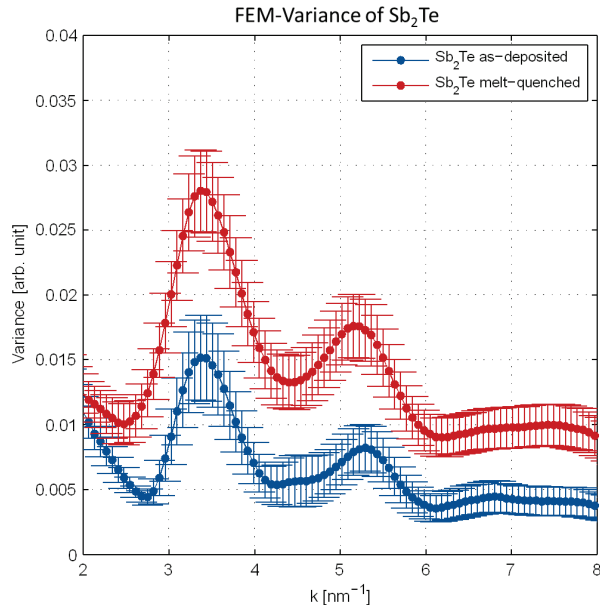


Figure 37: Shown are the variance plots in relation to the scattering vector k of as deposited and melt quenched Sb_2Te . Both graphs show an offset to each other.

The presented method for thickness correction of FEM data was developed and implemented into the freely available MATLAB script of P. Voyles and M. Burton (Voyles & Burton, 2014) by J. Pries and is explained in detail in his master thesis (Pries, 2015). The original MATLAB routine provides an alternative way for thickness correction, which was not used in this work. The method developed by J. Pries is also described here because it is used for all FEM plots. **Figure 37** shows uncorrected FEM data of two lamellas of the phase change material Sb_2Te , one lamella in the as deposited and one lamella in the melt quenched amorphous state. This material was investigated in the master thesis of J. Pries (Pries, 2015) and in the doctoral thesis of J. Benke (Benke, 2017). The shown variance plots of Sb_2Te are used as an example for the thickness correction procedure. It is easy to see that the uncorrected FEM data of the as deposited and the melt quenched Sb_2Te plots have an offset. This is seen best in the flat regions between 6 nm^{-1} - 8 nm^{-1} . A big difference in variance values in these high k regions of both measurements is physically not plausible. This is especially true because no peaks of variance seem to be present there. The idea is to correct for this thickness artefact by a further normalization process in the variance calculation.

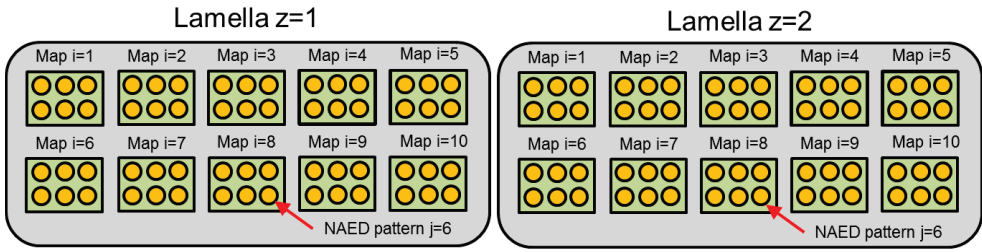


Figure 38: Schematic drawing of the index definition used for the thickness correction.

The specimens are indexed by z . On every specimen, maps of usually 100 NAED patterns are taken. The maps are indexed by i and every single NAED pattern is indexed by j (**Figure 38**). From the intensities of a single NAED pattern the annular averaged intensity $I_{z,i,j}(k)$ is calculated.

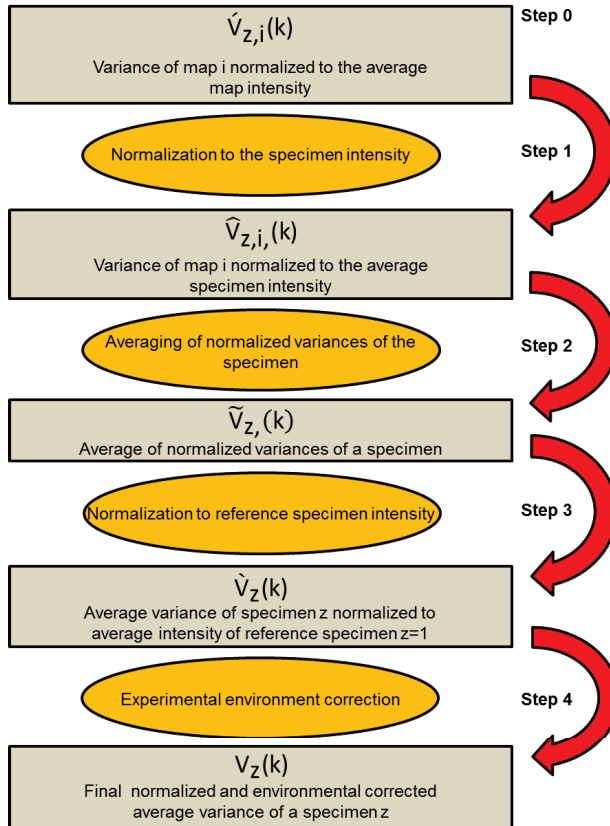


Figure 39: Schematic drawing of the step by step calculation of the various variances involved in the thickness correction procedure.

The integrated intensity $I_{int,z,i,j}$ of a single annular averaged NAED pattern j is then calculated by:

$$I_{int,z,i,j} = \int_0^{\infty} I_{z,i,j}(k) dk \quad (38).$$

For the normalization of the intensities $I_{z,i,j}(k)$ in every NAED pattern j of a map i the average intensity $I_{avg,z,i}$ of the whole map i is calculated by:

$$I_{avg,z,i} = \frac{1}{N} \cdot \sum_{j=1}^N I_{int,z,i,j} \quad (39),$$

where N is the number of NAED patterns in the map. The intensities $I_{z,i,j}(k)$ of every NAED pattern j are then normalized by:

$$\hat{I}_{z,i,j}(k) = I_{z,i,j}(k) \cdot \frac{I_{avg,z,i}}{I_{int,z,i,j}} \quad (40).$$

In **Figure 39** the step by step calculation of the thickness corrected variance is shown in a schematic drawing as an overview of the procedure. The variance $\hat{V}_{z,i}(k)$ of the map i is calculated by **Equation 37** but for NAED patterns with intensities normalized to the average map intensity. For the normalization factor of the specimen the average intensity $I_{avg,z}$ of a specimen is calculated for M maps by:

$$I_{avg,z} = \frac{1}{M} \cdot \sum_{i=1}^M I_{avg,z,i} \quad (41),$$

where M is the number of maps. The variance $\hat{V}_{z,i}(k)$ of a map i , which is normalized to the average specimen intensity, is calculated by:

$$\hat{V}_{z,i}(k) = \hat{V}_{z,i}(k) \cdot \frac{I_{avg,z}}{I_{avg,z,i}} \quad (42).$$

The average variance $\tilde{V}_z(k)$ of a specimen is calculated by averaging over all normalized variances of the maps. This corrects the effects of thickness gradients in one specimen z . To compare two or more specimens, the average variances $\tilde{V}_z(k)$ of every specimen is normalized to one chosen specimen as reference. This is usually specimen $z=1$. The variance $\hat{V}_z(k)$ of a specimen z , which is normalized to the reference $z=1$, is calculated by:

$$\check{V}_z(k) = \check{V}_z(k) \cdot \frac{I_{\text{avg},1}}{I_{\text{avg},z}} \quad (43).$$

Finally, differences in the measurement environment are included. The vacuum beam intensity $I_{\text{vac},z}$ of the measurement of every specimen z is obtained and the average vacuum beam intensity $I_{\text{vac,avg}}$ is calculated. The final and between every measured and corrected specimen comparable variance $V_z(k)$ is then given by:

$$V_z(k) = \check{V}_z(k) \cdot \frac{I_{\text{vac,avg}}}{I_{\text{vac},z}} \quad (44).$$

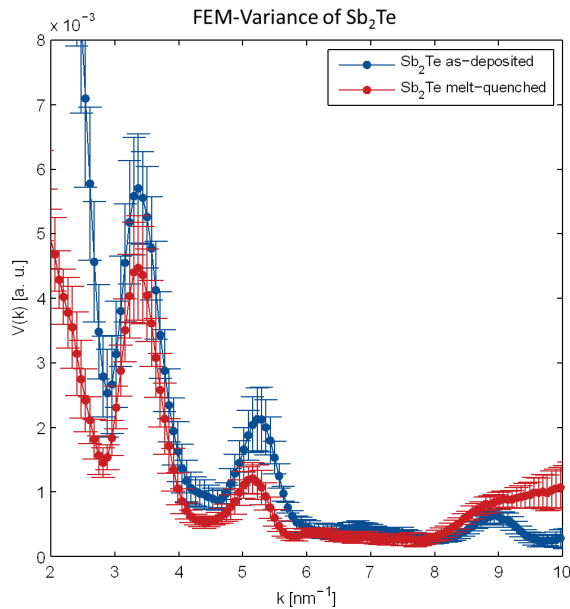


Figure 40: Shown are the corrected variance plots in relation to the scattering vector k of as deposited and melt quenched Sb_2Te . Both graph are now comparable and without an offset.

Figure 40 shows the corrected FEM plot of the previous shown Sb_2Te data. The differences in variance at high k values ($>8.5 \text{ nm}^{-1}$) of the melt quenched variance plot is probably an artefact known for specimen thicknesses close to the electron mean free path (Bogle et al., 2010). The differences in variance at low k values ($<3 \text{ nm}^{-1}$) are artefacts caused by the beam block in this region of the NAED pattern image. The FEM plots are now more comparable because the plot shows now

interpretable differences. The former strong offset caused by the thickness differences in the uncorrected data made this impossible. It should be noted that there is almost no influence on specimens with similar thicknesses and no thickness gradients because the normalization factors would be close to one (Pries, 2015; Benke, 2017).

6.2 Energy filtering to improve image quality in TEM and NAED

The electrons in the electron beam of a TEM or STEM can undergo energy losses by inelastic interactions with the specimen. A magnetic prism can spread the electron beam in relation to the energies of the electrons. This spread of electrons can be imaged on a detector like a CCD as an electron energy loss spectrum. This method is therefore called electron energy loss spectroscopy (EELS) (Reimer & Kohl, 2008; Williams & Carter, 2009). In **Figure 41** a scheme of the function of a magnetic prism in a TEM is shown.

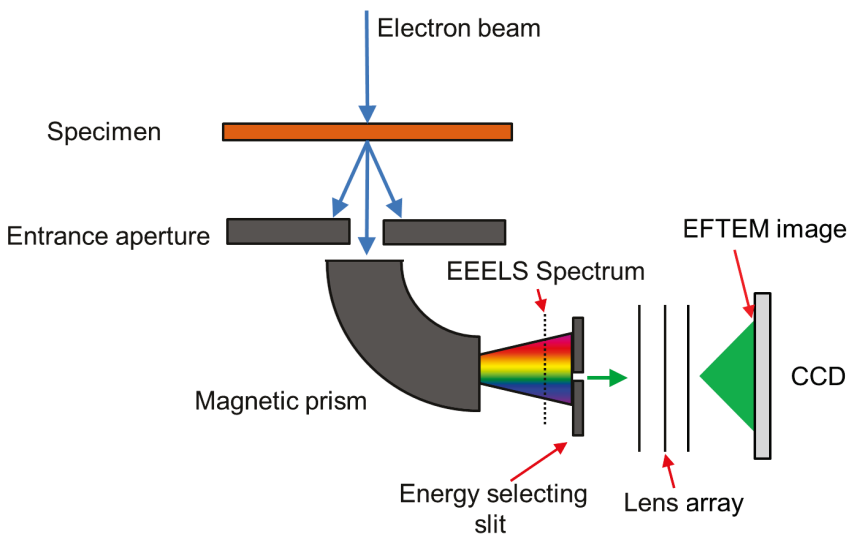


Figure 41: The electrons are deflected in the magnetic prism in relation to their energy. The EELS spectrum can be imaged or only a part of the spectrum is selected by an energy selecting slit for imaging.

The first peak in the EELS spectrum is the zero loss peak. Most electrons undergo no or only elastic scattering events in interaction with the specimen. The zero loss peak is usually by far the highest peak. The second highest peak in the EELS spectrum is the plasmon peak. Electrons that lose energy by exciting vibrations of

valence electrons of the specimen contribute to the plasmon peak. By comparison of the zero loss peak and the plasmon peak the thickness of a sample can be estimated. If a sample is very thick the plasmon peak can be the dominant peak. Further peaks in the higher energy loss regions are results of electrons that contribute to ionization of specimen atoms, which are element specific. The ionization peaks can be used for an element analysis (**Figure 42**). The magnetic prism and lenses to correct distortions, which are introduced by the prism, precede the CCD in the energy filter. By introducing a slit, parts of the EELS spectrum can be filtered out. This is used to filter out the inelastic scattered electrons and therefore enhance the contrast of TEM bright field images and the contrast of the NAED patterns (Reimer & Kohl, 2008; Williams & Carter, 2009).

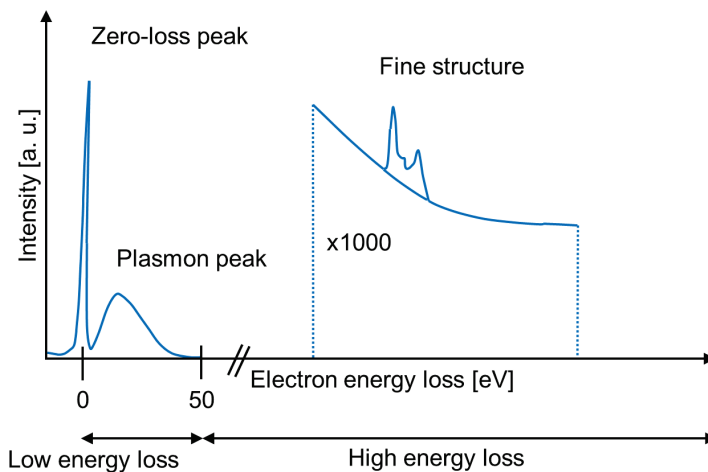


Figure 42: Schematic drawing of an EELS spectrum with some typical features.

6.3 Sample and TEM specimen preparation

In the following chapters the preparation of the various samples and the preparation of the specific specimens for TEM and STEM are described. Electron transparent specimens for both techniques will only be called TEM specimens in this work because the requirements for TEM and STEM are very similar (Reimer & Kohl, 2008; Williams & Carter, 2009). There is also a brief description of the sample preparation preceding the TEM specimen preparation. More detailed information about the sample preparation can be found in the given references.

6.3.1 Phase change material multilayer stack sputter deposition on silicon substrate

Si (100) wafers with dimensions of 2 cm x 2 cm and with a 50 nm thick layer of amorphous silicon nitride are used as substrates. The silicon nitride was deposited on the wafers prior to the further deposition steps by the AMO GmbH. The multilayer stack shown in **Figure 43** was deposited in the I. Institute of Physics (IA) by magnetron sputtering from stoichiometric targets (Kaldenbach, 2012; Wasa, 2012).

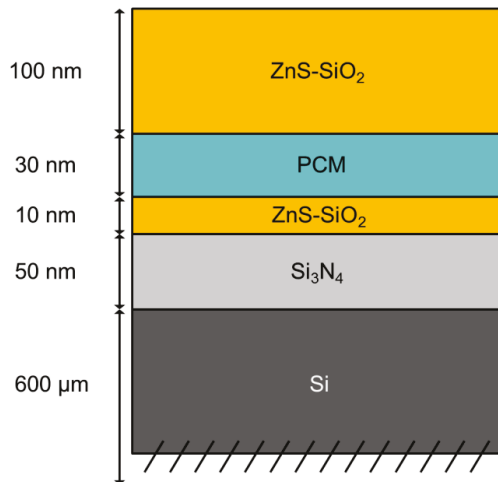


Figure 43: Scheme of the cross section of the chosen multilayer stack design.

The shown multilayer stack was designed to fulfill the requirements of in plane TEM specimen preparation by etching and to enable melt quenching of the phase change layer by laser irradiation. The silicon is used as a heatsink if the phase change material is melted by laser and afterwards quenched to reach the required cooling rates ($<10^9 \text{ Ks}^{-1}$). The silicon nitride layer is an etching stop implemented for in plane TEM specimen preparation. A 30 nm thick film of as deposited phase change material is sandwiched between two layers of amorphous $(\text{ZnS})_{80}:(\text{SiO}_2)_{20}$ to prevent oxidation, evaporation and enhance the mechanical stability when heated. For melt quenched phase change material samples, the phase change material layer is crystallized by heating in a vacuum furnace. The heating ramp is started from room temperature and increased in $2 \text{ }^\circ\text{C/s}$ steps until it reaches $473.15 \text{ }^\circ\text{K}$ and hold at this temperature until the material is completely crystalline. M. Mio of the National Research Council of Italy (CNR) melted circular regions with a diameter of around 2-

4 mm by laser irradiation. These regions were quenched to room temperature in the amorphous melt quenched state afterwards.

6.3.2 AIST line cell on silicon substrate

AIST line cells were produced in the I. Institute of Physics (IA). Detailed information about the preparation process can be found in the doctoral thesis of M. Wimmer (Wimmer, 2015). A line of AIST is deposited on silicon dioxide and is contacted by two electrodes from above. The whole structure is then capped by $(\text{ZnS})_{80}:(\text{SiO}_2)_{20}$. The cell can be switched by contact pads connected to the electrodes on top of the AIST line. **Figure 44** shows the scheme of such line cell structures.

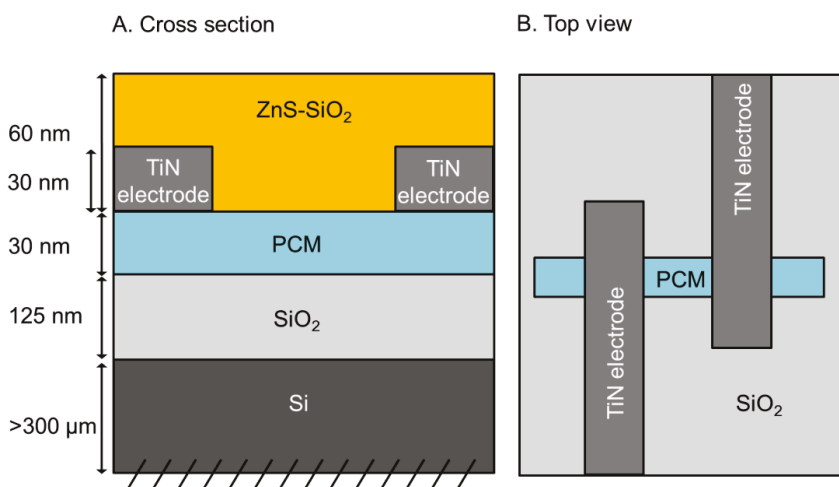


Figure 44: Shown are schematic drawings of the cross section (A) and the top view without the $(\text{ZnS})_{80}:(\text{SiO}_2)_{20}$ capping layer (B) of the line cell layouts investigated in this work.

6.3.3 Wet solvothermal synthesis of Sb_2Te_3 hexagon platelets

In a Teflon-lined autoclave, antimony oxide and tellurium dioxide were heated in the presence of polyvinylpyrrolidone (PVP) in diethylene glycol and sodium diethylene glycolate under solvothermal conditions at 473.15 K. Intermediates of this chemical synthesis were produced by T. Salzmann from the Institute of Inorganic Chemistry. To form the intermediates, the reaction was stopped at different points in reaction time by quenching to room temperature. The intermediates were separated by centrifugation. To produce TEM specimens, 1 μl – 1.5 μl droplets of diluted product of the synthesis were applied to commercially available copper grids covered with

carbon film. After drying, the intermediates of the synthesis can then be analyzed by TEM and STEM on the carbon film. All analyzed specimens were prepared freshly. They were not older than one day to minimize effects of aging and oxidation. Further details of the synthesis are described in the doctoral thesis of T. Saltzmann (Saltzmann, 2014) and in a publication of T. Saltzmann and co-workers (Saltzmann et al., 2015).

6.3.4 MOVPE of GST 124 on silicon substrate

GST 124 was deposited by the PGI-9 by MOVPE on Si (111) wafers (Thompson, 1997; Schuck et al., 2015; Hardtdegen et al., 2016; Riess, 2017). The phase change material was deposited in a commercially available horizontal low-pressure cold wall MOVPE reactor AIX 200 from AIXTRON. The wafers were deoxidized by a 60 s dip in hydrofluoric acid (1 %). The carrier gas was pure N₂ which transported the source compounds Sb(C₂H₅)₃ and Te(C₂H₅)₂ as metal-organic precursors. 10 % Ge₂H₆ in H₂ was the chosen germanium source. Further details can be found in the doctoral thesis of S. Riess (Riess, 2017), in the publication of M. Schuck and co-workers (Schuck et al., 2015) and in the publication of H. Hardtdegen and co-workers (Hardtdegen et al., 2016).

6.3.5 Plan view TEM specimen preparation

The specimen preparation technique for plan-view phase change material TEM specimens was developed in the process of the doctoral thesis of A. Kaldenbach (Kaldenbach, 2012). It was the main focus of the bachelor thesis of J. Scheifers (Scheifers, 2011) and part of my master thesis (Bornhöfft, 2012). In the present work the preparation technique was improved to be a routine procedure and used for this work, the bachelor thesis of J. Pries (Pries, 2013), the master thesis of J. Pries (Pries, 2015) and in the doctoral thesis of J. Benke (Benke, 2017). The main difference to earlier approaches is the use of cyanoacrylate adhesive, which is easier to dissolve by acetone.

For the preparation, the Si wafers with the deposited multilayer stack described in **Chapter 6.3.1** are used. The wafer is glued by cyanoacrylate adhesive on top of a metal bloc. The deposited surface is facing the polished metal bloc surface. The cyanoacrylate adhesive provides a mechanical stable connection between wafer and metal bloc and protects the wafer surface against damage and contamination at the

same time. An ultra-sonic disc cutter from Gatan cuts discs with a diameter of 3 mm from the glued wafer. A diameter of 3 mm is the standard size of most TEM specimen holders. The disc cutter uses a mixture of 70 % boron carbide and 30 % amorphous silicon diluted in distilled water. Afterwards the metal bloc with the cutted discs and the rest of the sample is submerged for one hour in an acetone bath. This dissolves the cyanoacrylate adhesive beneath the disc surface. The extracted discs are submerged afterwards in a clean acetone bath around 1 min - 2 min, with the deposited surface facing upwards, to dissolve any remaining adhesive. Contamination of acetone is removed in two consecutive pure isopropanol baths. The discs are put onto paper towel with the deposited surface facing downwards. This secures a uniform and fast drying of the deposited surface with as little contamination as possible. After the deposited surface has dried, the disc is turned over to dry from the backside. The dried discs are glued with cyanoacrylate adhesive on glass sample holder discs from Bühler with the deposited surface facing the glass surface.

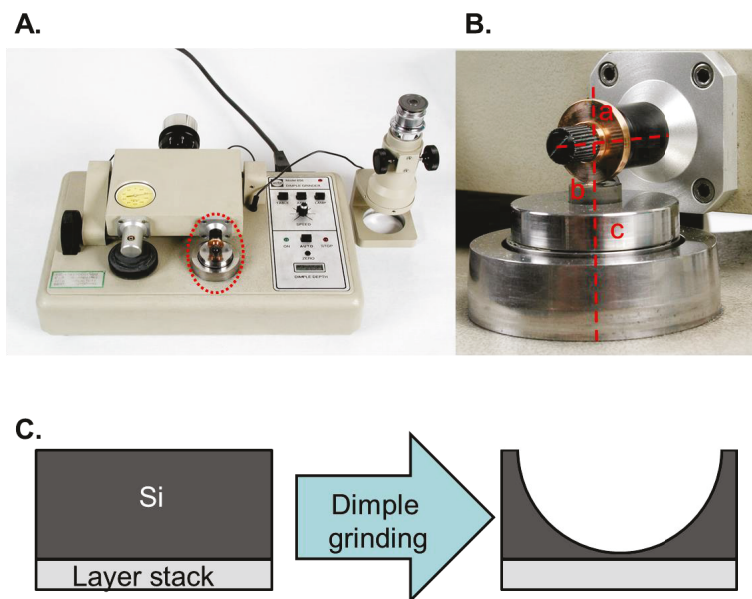


Figure 45: (A) A dimple grinder from Gatan is used to thin a sample mounted in the region marked by a red frame. (B) In closer view of the thinning process in the framed region it can be seen that the wheel (a) spins on top of the disc (b) which is mounted to a rotating table (c). The rotation axes are marked red. (C) The schematic drawing shows the part of the sample that got thinned away by the grinding process.

An automated grinder from Bühler grinds one disc at a time from their original thickness of 300 μm - 600 μm down to a thickness of 100 μm – 150 μm . To ensure a

smooth grinding a few drops of distilled water are applied on the grinding disc before the process. The grinded discs are removed and cleaned as described for the ultra-sonic disc cutting. The cleaned discs are glued with cyanoacrylate adhesive on glass sample holder cylinders from Gatan with the deposited surface facing the glass surface. In the dimple-grinder one disc at a time is rotating around its center, while first a metal wheel and then a felt wheel is spinning in a diamond water suspension, with a grain size of $3\ \mu\text{m}$, on the silicon surface of the sample disc. This forms a dimple in the center of the disc. Most material is taken away in the center. The edge of the sample stays close to the original thickness. The metal wheel is used for grinding until the center of the disc reaches a thickness of around $40\ \mu\text{m}$. Afterwards the felt wheel polishes the surface until the center of the disc reaches a thickness of around $10\ \mu\text{m}$ (**Figure 45**). The polishing ensures a more uniform and faster etching.

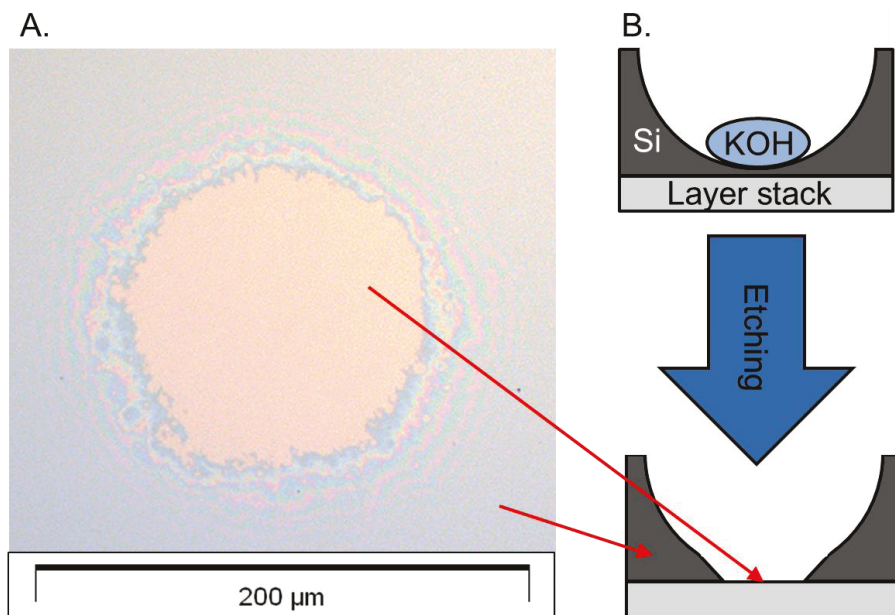


Figure 46: (A) Shown is a light microscope image of a typical electron transparent specimen window. (B) Shown is a schematic drawing of the specimen before and after the etching process. The red arrows connect the related regions between the light microscope image and the scheme.

The glass cylinder with the dimple grinded disc is removed from the dimple grinder and is rinsed with distilled water and with ethanol to remove rests of the diamond suspension. The glass cylinders with the glued discs are put on a heating plate set to 343.15°K - 353.15°K to increase the following etching process. A pipette set to $0.2\ \mu\text{l}$

is used to put small droplets of 30 % KOH solution into the center of the dimple of the discs. When the droplet is completely dried, it is rinsed away with warm distilled water, which is also located on the heating plate in a small glass bowl. Onto the dried disc a new droplet of KOH is put into the dimple. This is repeated until a 100 μm – 500 μm in diameter large specimen window, with removed silicon substrate, forms inside the center of the dimple. After the etching process, the discs are removed from the glass holder and cleaned the same way described above. The thickness of the edges of the discs is still around 100 μm . This enables the handling of the specimen with sharp metal tweezers. The described sample preparation method produces silicon free specimen TEM windows with diameters above 100 μm . The described multilayer system including the silicon nitride etch stop is now electron transparent and ready for TEM or STEM analysis (**Figure 46**).

In the preparation process the specimen surface was contaminated with chains of iron oxide nanoparticles of various amounts. The particles were around 50 nm in size and only the thinned surface site was contaminated. This was checked by TEM tomography. The origin of the nanoparticles is not completely understood. The contamination occurred in different labs by using completely different equipment and preparing different sample systems. Using plastic bowls instead of glass bowls and plastic tweezers instead of metal tweezers does not prevent the contamination. A thorough investigation of all the preparation steps and materials by SEM EDX narrows the origin of the nanoparticles on the etching process and revealed that they are iron oxides. The used KOH pellets were of laboratory quality and purity. Nonetheless it is until now the most likely iron source. The iron oxide particles have no measurable effect on the results described later, because they are separated from the investigated multilayer system by the silicon nitride layer. They also do not change their position or shape while the specimens are heated, which makes them at least good position markers to identify the same regions and orientations on the specimens.

6.3.6 Ex situ heating of plan view TEM window specimens

To measure the crystallization kinetics, the plan view TEM window specimens are heated between measurements in a differential scanning calorimeter (DSC) from Perkin Elmer. The heating furnace of the DSC is used as a very precise oven with a maximum error of 0.5 K. In the DSC the temperature control is automated and the

heating procedure starts and stops at room temperature. A heated oil bath is used for higher temperatures, where the heating and cooling rates of the DSC would be too low. The specimens are dipped and held in the oil bath kept on the chosen temperature for a measured amount of time. Afterwards the sample is cooled down rapidly to room temperature in Glycol. Both methods are not strictly isothermal because the specimens are heated and cooled, but the heating and cooling ramps are very steep compared to the isothermal plateau of the chosen temperature for the experiment. The time of the heating and cooling ramps is neglected in the presented measurements except of influence to the statistical error.

6.3.7 Cross section TEM lamella preparation

Electron transparent cross-section lamellae were prepared on a Helios dual beam FIB/SEM from FEI. The used machine was the FEI Helios Nanolab of the I. Institute of Physics (IA). The sample is glued to a metal holder with conductive silver paste. To enhance conductivity of the sample, the sites, the rim of the sample and overhanging parts of the sample on the backside are also covered by silver paste. The sample surface is also covered with up to 50 nm of carbon, deposited by a carbon coater. These preparation steps prevent charging in the Helios.

In the Helios a 200 nm thick, 2 μm broad and 10 μm - 15 μm long platinum protection layer is deposited with the electron beam at 2 keV energy and 0.8 nA - 1.6 nA beam current and 0° stage tilt (electron beam orthogonal to the sample surface). Additional 2 μm of platinum are deposited by the ion beam at 52° tilt (ion beam orthogonal to sample surface), 30 keV ion energy and 0.43 nA - 0.79 nA beam current (**Figure 47**). In parallel to the long sites of the platinum protection layer, trenches are cut by the ion beam at 52° stage tilt, 30 kV and 0.79 nA - 2.5 nA. The trenches are a few micrometers longer as the platinum protection layer. The depth of the trenches decreases in steps from their deepest point close to the platinum protection layer (**Figure 47**). Afterwards, the sample is tilted back to 0° stage tilt. At the left short side of the platinum protection layer a 1 μm broad and a few micrometer long trench is cut upwards by the ion beam. At the same time a trench is cut in parallel to the long side of the platinum protection layer. This 1 μm broad trench undercuts the lamella because of the tilt of the ion beam to the surface and is a little longer than the protection layer. Both trenches are cut by the ion beam at 30 keV ion energy and 0.79 nA - 2.5 nA beam current. Material that has redeposited in the cutting process

has to be removed with the ion beam afterwards, especially if it has built an additional mechanical connection from sample to lamella at some other location (**Figure 47**).

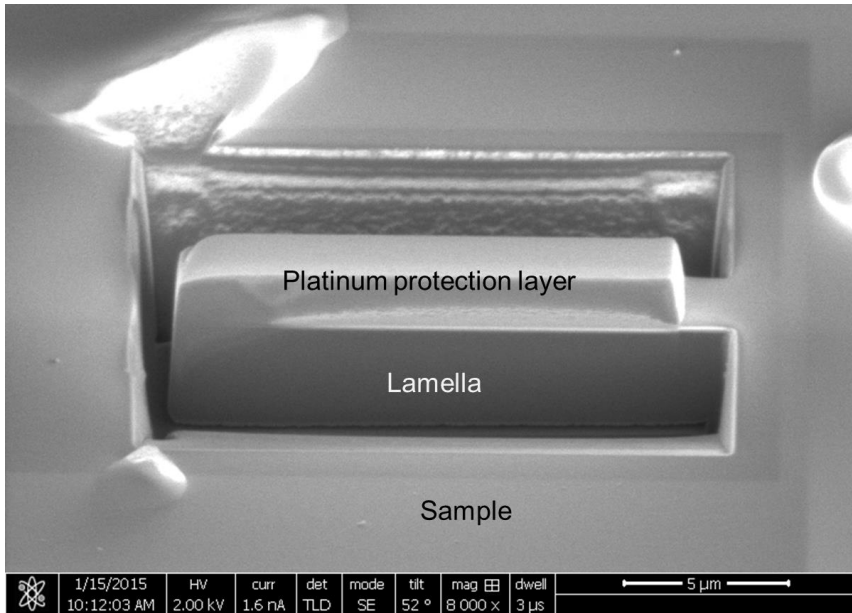


Figure 47: The shown cross section lamella is cut free from the sample except of a connection at the right side. The protection layer can be seen as the embossed material on top of the lamella. The lamella is cut free by two big trenches, a cut at the left side and an undercut over the whole length of the lamella.

The lift-out of the lamella is performed by a build-in micro-manipulator at 0° tilt. The micro-manipulator contacts the lamella at the short left-hand side with a velocity of 0.1 μm/s to prevent drift of the manipulator. The tip of the manipulator and the lamella are bonded with 1 μm of ion beam deposited platinum at 30 kV and 43 pA - 80 pA. Afterwards a 1 μm broad trench is cut, on the short right-hand side of the lamella, to separate the lamella from the sample. The ion beam cutting of this trench is executed at 30 keV ion energy and 0.79 nA - 2.5 nA beam current until the lamella is completely separated from the sample and is now only connected to the manipulator. To protect the lamella, the manipulator with the connected lamella is retracted into a save parking spot inside the Helios. The sample is then exchanged against a copper grid specially used for TEM lamella attachment. On the copper grid are posts at which the lamella can be connected. The manipulator with the attached lamella approaches one of the posts from the left-hand side. The short right-hand side of the lamella contacts the surface of the left-hand side of a post with a velocity of 0.1 μm/s.

The lamella and the post are bonded with 1 μm of ion beam deposited platinum at 30 keV ion energy and 43 pA – 80 pA beam current. Afterwards the manipulator gets separated from the lamella by the ion beam at 30 keV ion energy and 0.79 nA - 2.5 nA beam current. The manipulator is retracted afterwards. The platinum covered part of the lamella on the short left-hand side is removed by the ion beam at 30 keV ion energy and 0.79 nA - 2.5 nA beam current. This ensures a better geometry of the lamella for the following thinning steps. Additionally, 1 μm of ion beam deposited platinum are often deposited at the connection between lamella and post to increase mechanical stability (**Figure 48**).

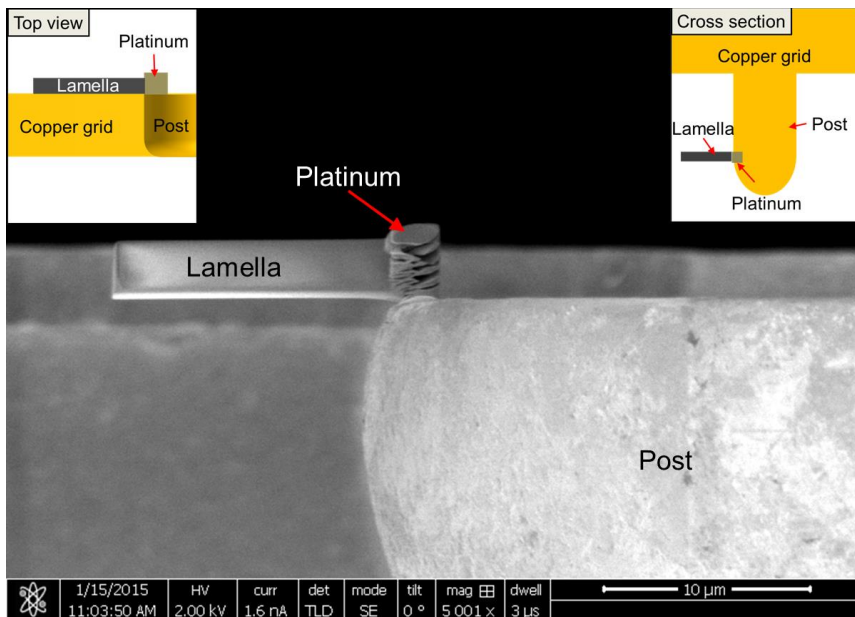


Figure 48: The shown cross section lamella is attached at a post of the special copper grid by ion beam deposited platinum and ready for further thinning. Additional platinum was deposited at the connection for mechanical stability. Furthermore remainders of the connection to the micromanipulator were cut away by the ion beam. Schematic drawings of the cross section and top view of the lamella are shown to explain the geometry.

A thickness below 100 nm is ideal for an electron transparent lamella to be analysed by TEM (Reimer & Kohl, 2008; Williams & Carter, 2009). So the lamella has to be thinned further with the ion beam. The angles for thinning are material dependent. The thinning of the lamella starts with decreasing the thickness of the lamella to 1 μm by ion beam cutting at 30 keV ion energy and 0.79 nA - 2.5 nA beam current. The next step is to decrease the thickness to 300 nm by ion beam cutting at 30 keV ion

energy and 0.23 nA - 0.49 nA beam current. Further the lamella is thinned to 100 nm by ion beam cutting at 30 keV ion energy and 33 pA - 80 pA beam current. Short lamellas are less likely to bend while their thickness decreases. Often only a part of the extracted lamella is thinned to 100 nm and below. FEM and high resolution imaging in STEM require very thin lamellas and benefit from cleaning away material amorphized by the ion beam. This can be done by careful ion beam showering at low ion energies (5 keV and 2 keV). Unfortunately, lamellas with thicknesses below 100 nm often start to bend which has to be taken into account. The bending can lead to inhomogeneous thinning, deformation of the lamella and the destruction of the lamella. This general procedure can be used for most cross section lamellas. A finished lamella in top view is shown in **Figure 49**.

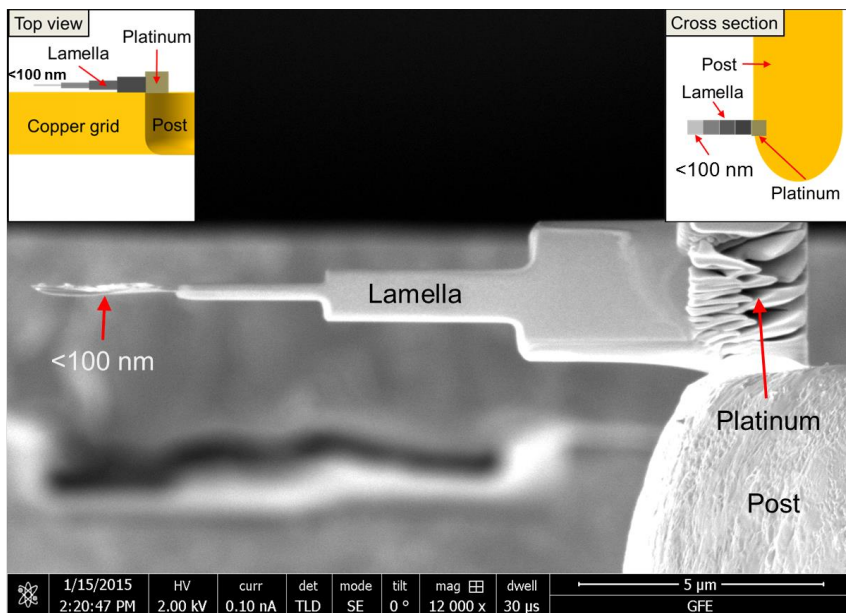


Figure 49: In this top view of a finished cross section TEM lamella from a step by step thinning is shown. The thinnest part of the lamella on the left is a very thin (thickness < 100 nm) foil. A slight bending of the foil is observable. Schematic drawings of the cross section and top view of the thinned lamella are shown to explain the geometry.

7 Results

In the following chapters the obtained results are presented. There are four main parts: the crystallization kinetics of AIST and GeTe thin films, including the FEM analysis, the TEM investigation of AIST line cell cross sections, NAED of Sb_2Te_3 platelet intermediates and the TEM/STEM investigation of a GST 124 layer grown by MOVPE.

7.1 Crystallization kinetics of AIST and GeTe thin films

In order to measure and understand the crystallization kinetics of phase change materials, a combination of two methods was used. The growth velocities of as deposited and melt quenched AIST and GeTe were determined by alternating ex situ heating of plane view TEM window specimens and bright field TEM imaging. Furthermore, the variance of as deposited and melt quenched AIST and GeTe cross section lamellas was determined by FEM as a measure of the MRO in the materials.

7.1.1 TEM measurements of grain growth velocities of AIST and GeTe

The growth of grains in an amorphous matrix was investigated by energy filtered bright field TEM (**Chapter 6.1.4.1**). TEM window specimens were used (**Chapter 6.3.5**). Growth velocities were determined for as deposited and melt quenched AIST and GeTe. The specimens were heated ex situ in a DSC or an oil bath (**Chapter 6.3.6**) at a chosen temperature, until first grains were detected by light microscopy in the electron transparent TEM window areas of the specimens. Grains were imaged by bright field TEM and their size fitted by circles whose radii were measured. The fitting of circles was used because of the observed isotropic growth of the grains. **Figure 50** shows a typical bright field TEM image used for grain size measurement. After the measurement, the specimens were annealed again at the same temperature. Afterwards they were imaged and measured again in the described way. If possible radii of the same grains at 3 different times were measured. The results were expected to be independent of temperature, because the crystal growth of investigated phase change materials indicated to be interface controlled (Raoux, 2009). The growth velocities were then given by the slopes of a linear fit of the grain radii related to the heating times.

We found for as-deposited AIST at 413.15 K, where more than 5 radii at different heating times for 6 grains were measured, a quadratic increase in radii with time (Benke, 2017). The effect could be either attributed to the influence of the electron beam or interface effects, which reduce the activation barrier for atom jumps and increase the attempt frequency (Pandian et al., 2007). For as deposited GeTe we found at an extended study at 423.15 K, where more than 6 radii at different heating times for 12 grains were measured, a decrease in radii with time. J. Pries could fit the decrease with a local or global Kohlrausch-Williams-Watts (KWW) model. Therefore, the decrease was attributed to aging and/or formation of stress (Pries, 2015). Both effects can be described by the KWW model. Aging is especially probable, because GeTe is known to have pronounced resistance drift (Wimmer et al., 2014). An influence of phase separation could be excluded by TEM EDX analysis. In the observed time scales of our measurements the effects were small. Therefore, we used a linear fit as a sufficient approximation for growth velocity calculation.

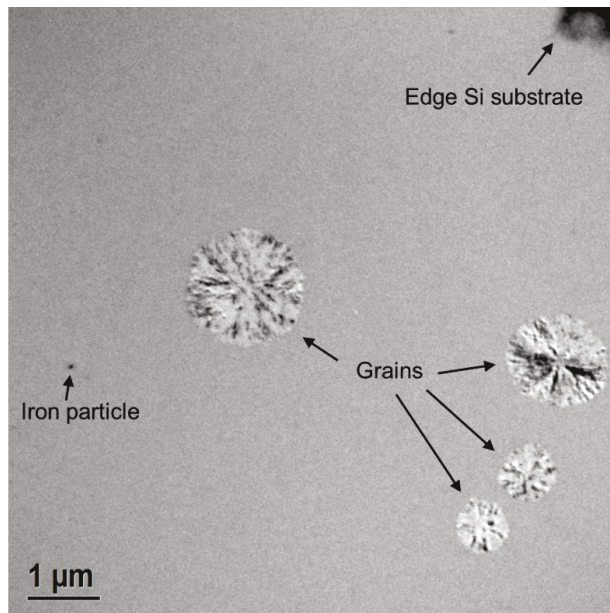


Figure 50: Bright field TEM image showing grains in as deposited AIST after 90 min of ex situ heating at 418.15 K. A single iron particle and the edge of the Si substrate can be seen, which are used for orientation.

The same grains could be found again by identifying landmark formations in the silicon at the specimen window edges, artefacts or by orientation on a light microscope image recorded beforehand. Grains nucleated statistically in the

amorphous matrix were preferred for measurement of the growth velocities but there was no difference in growth velocities observed for grains nucleated at observed damage sites in the film. Grains that nucleated at damage sites were used mainly for the melt quenched samples which contained much more of this damage sites. Furthermore melt quenched samples of AIST nucleated much later without the help of damage sites, which was expected after the results from Lee and co-workers (Lee et al., 2009b).

7.1.1.1 Growth velocities of as deposited AIST

TEM window specimens of as deposited AIST were annealed at 413.15 K, 418.15 K, 423.15 K and 428.15 K. **Figure 51** shows an example of a growing grain of as deposited AIST at three steps of heating time at 418.15 K. The measurement for a single grain starts, as soon as it was detected by TEM bright field imaging for the first time. The grains are growing isotropically. In the grains Bragg contrast of bending contours are visible. The growth velocities of the grains are calculated from the slope of the growing radii over heating time. **Figure 52** shows examples of the linear fits for one example grain per temperature and that the approximation of linear growth is sufficient for the calculation of the growth velocity. The growth velocity of as deposited AIST is calculated as the average of all growth velocities of the measured grains at one heating temperature (413.15 K: 18 grains; 418.15 K: 36 grains; 423.15 K: 15 grains; 428.15 K: 14 grains). **Figure 53** shows the growth velocities of as deposited AIST related to the heating temperatures. In **Figure 53** the Arrhenius like behaviour of the measured crystal growth velocities with increasing temperature can be observed.

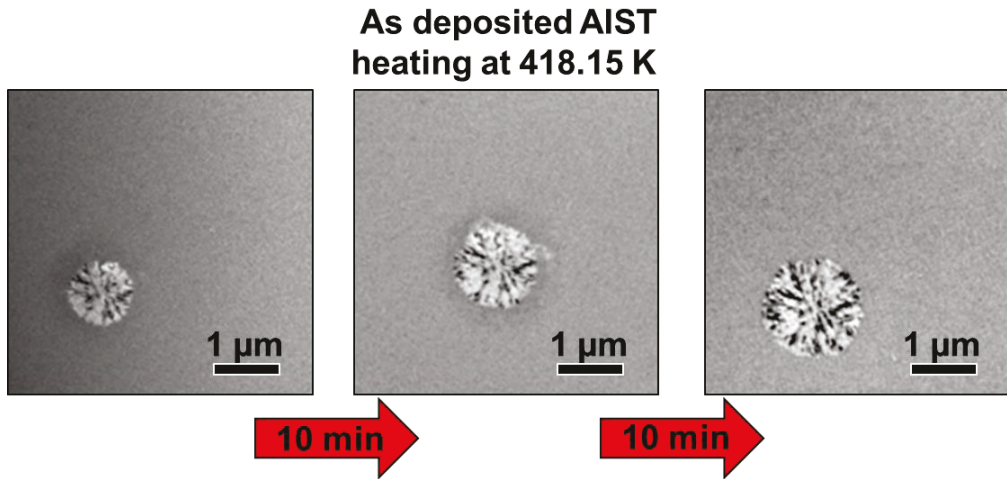


Figure 51: Shown is a single grain in as deposited AIST growing from ex situ heating.

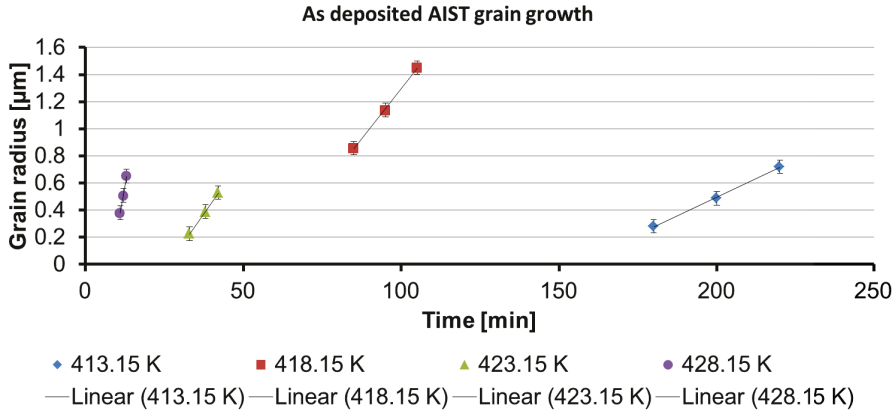


Figure 52: Shown are examples of the as deposited AIST grain radii over heating time. The linear fits are used to calculate the slopes and therefore the growth velocities of the grains. The starting point of a measurement of a grain is the first time the grain was found in the TEM after a heating cycle.

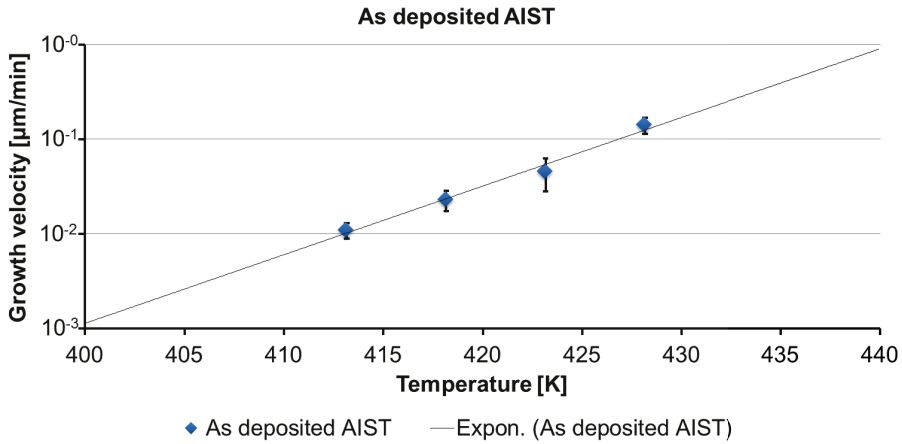


Figure 53: The growth velocity of as deposited AIST shows Arrhenius like behaviour with increasing temperature.

7.1.1.2 Growth velocities of melt quenched AIST

TEM window specimens of melt quenched AIST were annealed at 383.15 K, 388.15 K and 393.15 K. The measurement for a single grain starts, as soon as it was detected by TEM bright field imaging for the first time. **Figure 54** shows an example of a growing grain of melt quenched AIST at three steps of heating time at 393.15 K. The grains are growing isotropically. In the grains, Bragg contrast of bending contours is visible. The growth velocities of the grains are calculated from the slope of the growing radii over heating time.

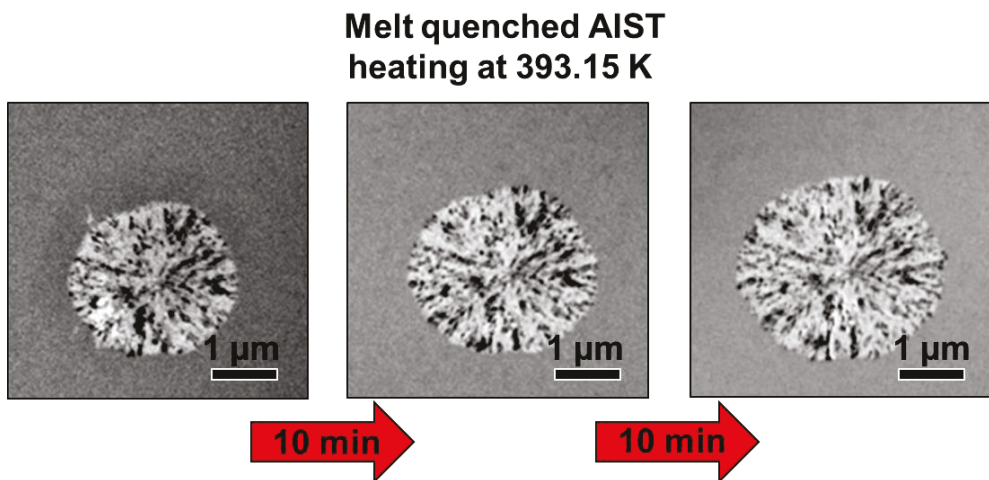


Figure 54: Shown is a single grain in melt quenched AIST growing from ex situ heating.

Figure 55 shows examples of the linear fits for one example grain per temperature and that the approximation of linear growth is sufficient for the calculation of the growth velocity. The growth velocity of one temperature of melt quenched AIST is calculated as the average of all growth velocities of the measured grains at one heating temperature (383.15 K: 16 grains; 388.15 K: 5 grains; 393.15 K: 6 grains).

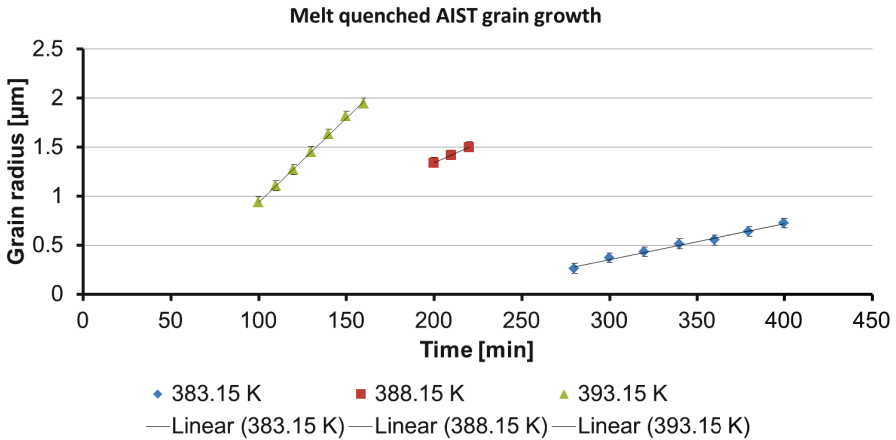


Figure 55: Shown are examples of the growing melt quenched AIST grain radii over heating time. The linear fits are used to calculate the slopes and therefore the growth velocities of the grains. The starting point of a measurement of a grain is the first time the grain was found in the TEM after a heating cycle. Error bars are partly hidden behind the markers.

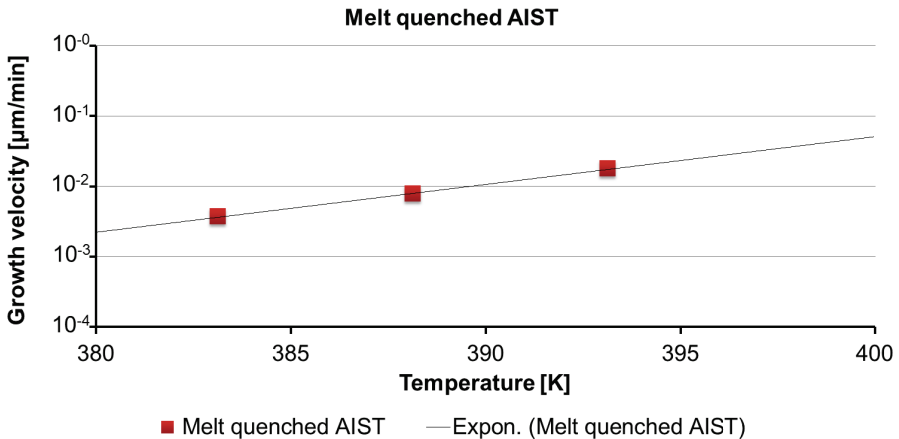


Figure 56: The growth velocity of melt quenched AIST shows Arrhenius like behaviour and increases with increasing temperature. Error bars are hidden behind the markers.

Figure 56 shows the growth velocities of melt quenched AIST related to the heating temperatures. In **Figure 56** the Arrhenius like behaviour of the measured crystal growth velocities with increasing temperature can be observed.

7.1.1.3 Growth velocities of as deposited AIST and melt quenched AIST in comparison

In **Figure 57** the growth velocities in relation to temperature of as deposited and melt quenched AIST are compared. The comparison reveals that melt quenched AIST grows over 1.5 orders of magnitude faster than as deposited AIST at a given temperature. This difference decreases only slightly with increasing temperature.

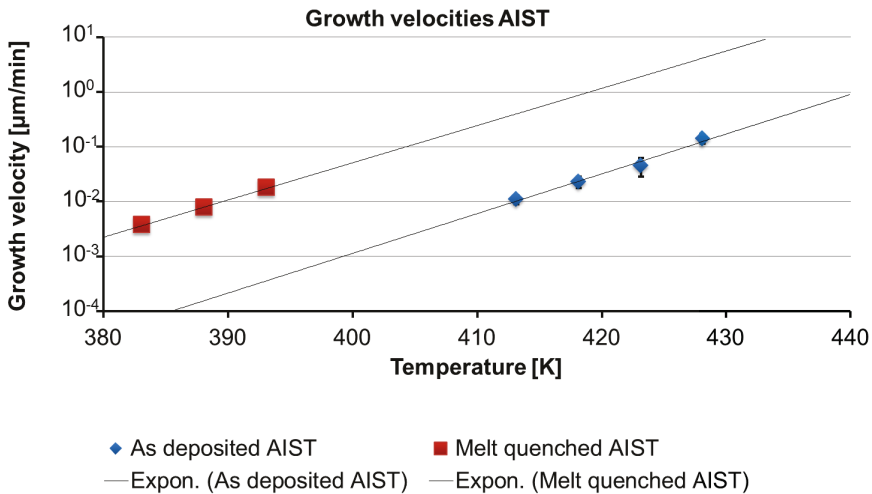


Figure 57: Shown is the comparison of the growth velocities of as deposited and melt quenched AIST in relation to temperature. Melt quenched AIST grows over 1.5 orders of magnitude faster than as deposited AIST at a given temperature. Error bars are partly hidden behind the markers.

7.1.1.4 Growth velocities of as deposited GeTe

TEM window specimens of as deposited GeTe were annealed at 408.15 K, 413.15 K, 418.15 K, 423.15 K, 428.15 K, 438.15 K, 443.15 K, 448.15 K and 453.15 K. The measurement for a single grain starts, as soon as it was detected by TEM bright field imaging for the first time. **Figure 58** shows an example of a growing grain of as deposited GeTe at three steps in heating time at 423.15 K. The grains are growing isotropically. In the grains, Bragg contrast of bending contours is visible. **Figure 59** shows examples of the linear fits for one example grain for 6 temperatures and that the approximation of linear growth is sufficient for the calculation of the growth

velocity. The growth velocities of the grains are calculated from the slope of the growing radii over heating time. The growth velocity of one temperature of as deposited GeTe is calculated as the average of all growth velocities of the measured grains at one heating temperature (408.15 K: 1 grain; 413.15 K: 3 grains; 418.15 K: 8 grains; 423.15 K: 10 grains; 428.15 K: 12 grains; 438.15 K: 15 grains; 443.15 K: 10 grains; 448.15 K: 9 grains; 453.15 K: 9 grains).

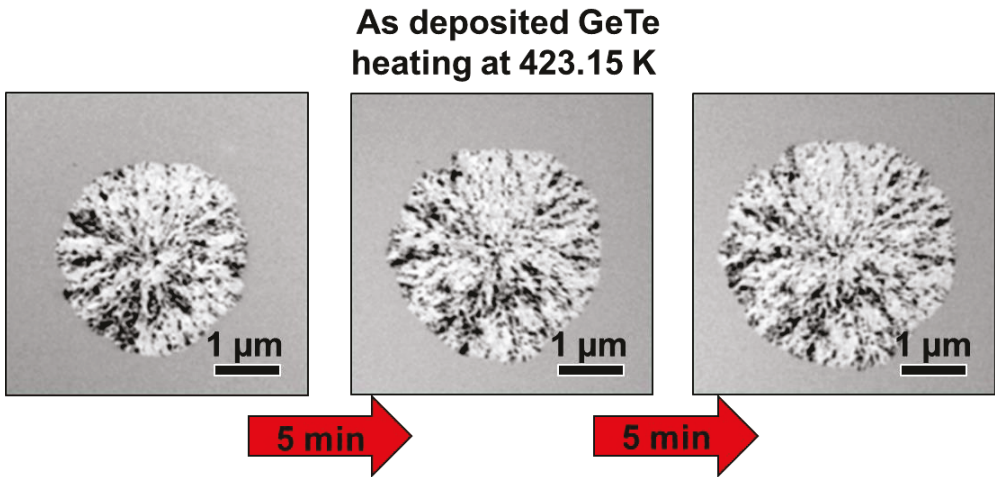


Figure 58: Shown is a single grain in as deposited GeTe growing from ex situ heating.

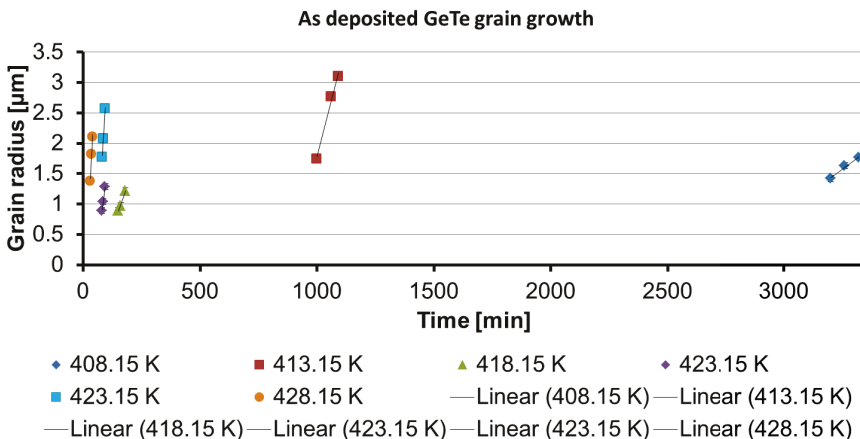


Figure 59: Shown are examples of the growing as deposited GeTe grain radii over heating time. The linear fits are used to calculate the slopes and therefore the growth velocities of the grains. The starting point of a measurement of a grain is the first time the grain was found in the TEM after a heating cycle. Error bars are partly hidden behind the markers.

Figure 60 shows the growth velocities of as deposited GeTe related to the heating temperature. The oil bath heating method used at higher temperatures produces results that are in good agreement with the DSC data. The growth velocities of as deposited GeTe show Arrhenius like behaviour.

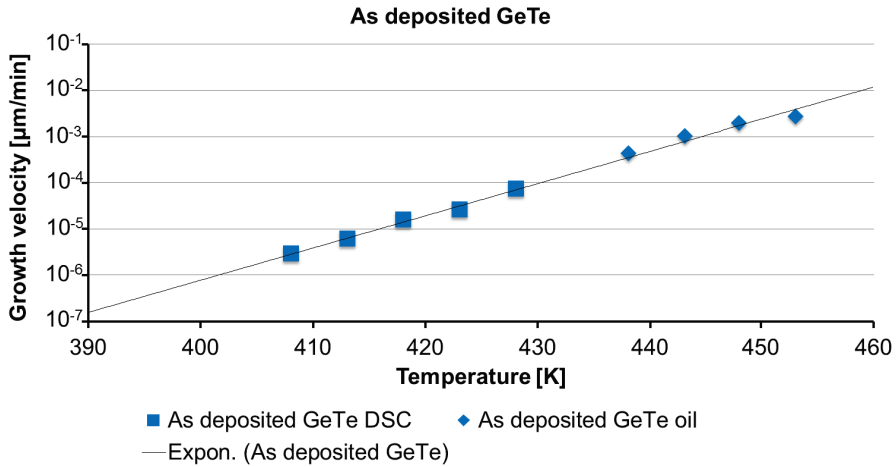


Figure 60: The growth velocity of as deposited GeTe shows Arrhenius like behavior and increases with increasing temperature. The DSC and oil bath method are in good agreement. Error bars are behind the markers.

7.1.1.5 Growth velocities of melt quenched GeTe

TEM window specimens of melt quenched GeTe were annealed at 418.15 K, 428.15 K, 438.15 K and 448.15 K. The measurement for a single grain starts, as soon as it was detected by TEM bright field imaging for the first time. **Figure 61** shows an example of a growing grain of melt quenched GeTe at three steps in heating time at 428.15 K. The grains are growing isotropically. In the grains, Bragg contrast of bending contours is visible. **Figure 62** shows examples of the linear fits for one example grain per temperature and that the approximation of linear growth is sufficient for the calculation of the growth velocity.

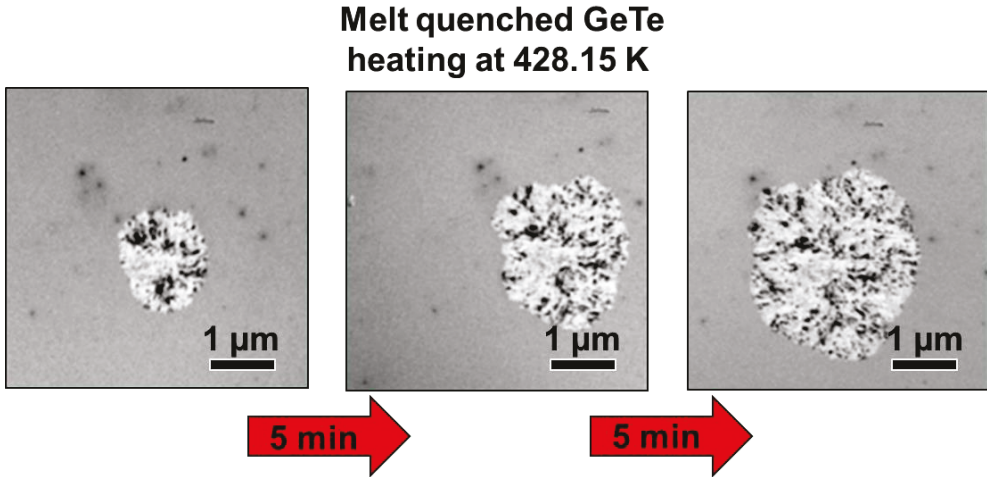


Figure 61: Shown is a single grain in melt quenched GeTe growing from the ex situ heating.

The growth velocity of one temperature of melt quenched GeTe is then calculated as the average of all growth velocities of the measured grains at one heating temperature (418.15 K: 7 grains; 428.15 K: 18 grains; 438.15 K: 21 grains; 448.15 K: 24 grains). **Figure 63** shows the growth velocities of melt quenched GeTe related to the heating temperatures. The graph in **Figure 63** shows also that the oil bath heating method produces results that are in good agreement with the DSC data. The growth velocities of melt quenched GeTe shows Arrhenius like behaviour.

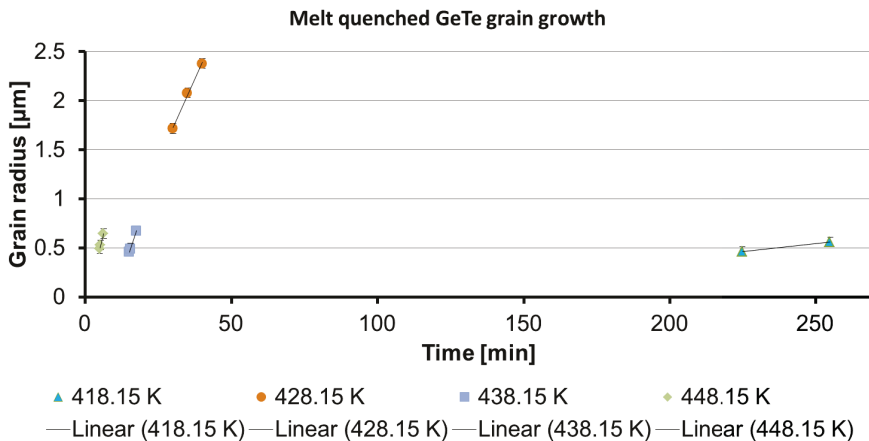


Figure 62: Shown are examples of the growing melt quenched GeTe grain radii over heating time. The linear fits are used to calculate the slopes and therefore the growth velocities of the grains. The starting point of a measurement of a grain is the first time the grain was found in the TEM after a heating cycle. Error bars are partly hidden behind the markers.

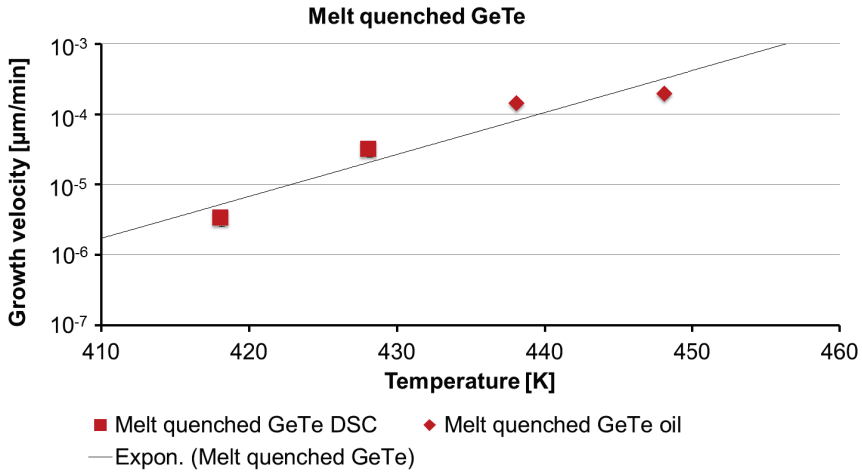


Figure 63: The growth velocity of melt quenched GeTe shows Arrhenius like behavior and increases with increasing temperature. The DSC and oil bath method are in good agreement. Error bars are behind the markers.

7.1.1.6 Growth velocities of as deposited GeTe and melt quenched GeTe in comparison

In Figure 64, the growth velocities in relation to temperature of as deposited and melt quenched GeTe are compared.

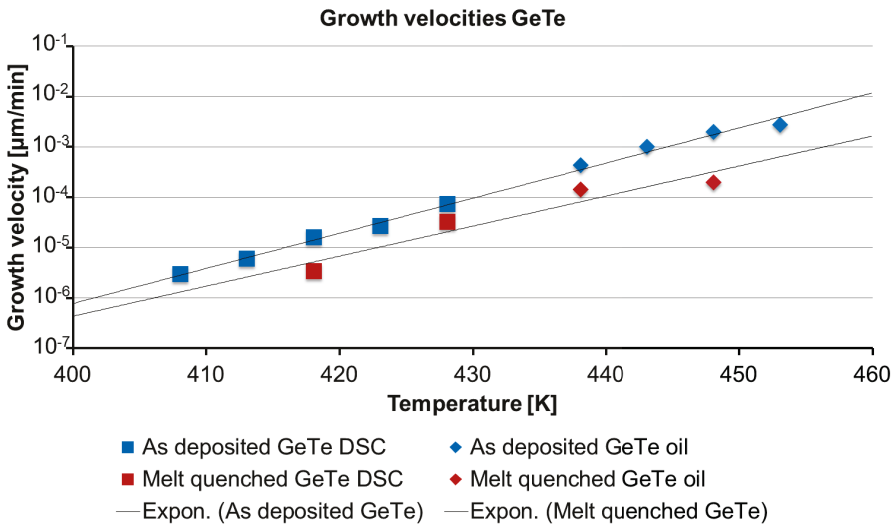


Figure 64: Shown is the comparison of the growth velocities of as deposited and melt quenched GeTe in relation to temperature. As deposited GeTe shows a slightly steeper slope of increasing growth velocity by increasing temperature than melt quenched GeTe. At a given temperature as deposited GeTe grows faster than melt quenched GeTe. Error bars are behind the markers.

The comparison reveals that as deposited GeTe grows faster than melt quenched GeTe at a given temperature. This difference increases with temperature because of a steeper slope of increasing growth velocity by increasing temperature of as deposited GeTe.

7.1.2 FEM of phase change thin film cross sections

For the FEM measurements, the microprobe mode of a 300 kV FEi Titan dedicated to STEM (Heggen et al., 2016) with a 10 μm C2 aperture for NAED was used. The probe size of the electron beam was adjusted to around 2 nm (**Chapter 6.1.5.2**). All NAED patterns were acquired with a beam blocker for the unscattered beam inserted. This prevented oversaturation of the CCD and overshadowing of other features in the diffraction patterns. It has to be taken into consideration that the manual positioning of the beam blocker produces artefacts in the FEM data between $0 \text{ nm}^{-1} - 3 \text{ nm}^{-1}$.

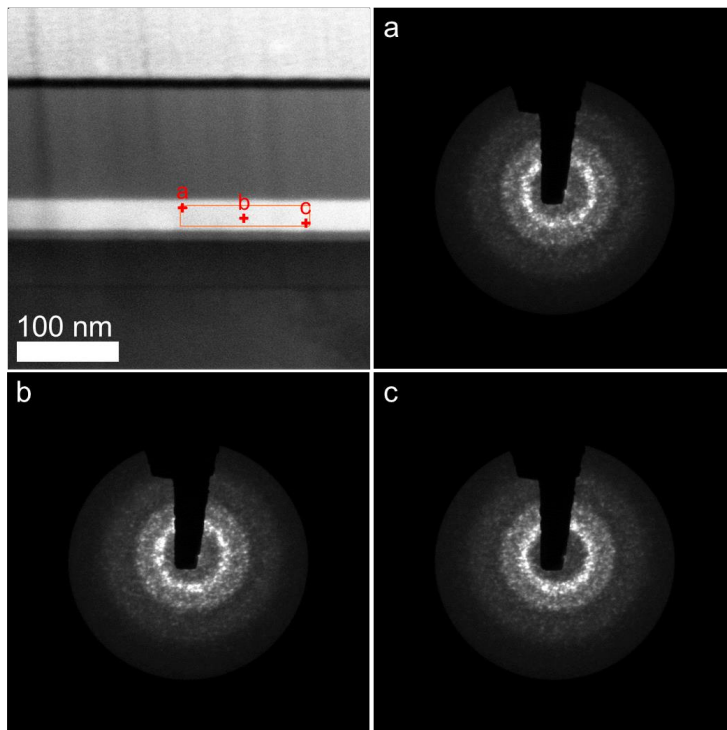


Figure 65: Shown is an ADF STEM image of a cross section lamella of melt quenched AIST. The orange rectangle marks the scanning field for the 100 NAED patterns that were acquired in the bright AIST layer. The red crosses mark the three exemplary NAED patterns a, b and c.

TEM cross section specimens produced by dual beam FIB/SEM were used (**Chapter 6.1.3**). **Figure 65** shows an example of a FEM scanning area and example NAED patterns of the depicted melt quenched AIST specimen.

7.1.2.1 FEM of AIST cross sections

Figure 66 shows the uncorrected FEM data of as deposited AIST and melt quenched AIST. The measured variance in diffracted intensity is plotted in relation to the scattering vector k . There is no big offset induced by thickness differences in the uncorrected data between the as deposited AIST and the melt quenched AIST. In the uncorrected data, a big difference in features of the plots of as deposited AIST and melt quenched AIST is already visible. The plot of as deposited AIST shows four peaks. The highest peak is at $\sim 4.3 \text{ nm}^{-1}$. The second highest peak is located at $\sim 3.2 \text{ nm}^{-1}$. The third highest peak is visible at $\sim 5.2 \text{ nm}^{-1}$ and a small peak at $\sim 7.4 \text{ nm}^{-1}$. The uncorrected FEM plot of melt quenched AIST shows two peaks. The highest peak in form of a shoulder is located at $\sim 3.2 \text{ nm}^{-1}$ and the second highest peak is located at $\sim 5.2 \text{ nm}^{-1}$. That corresponds to the positions of the second and third highest peaks in as deposited AIST.

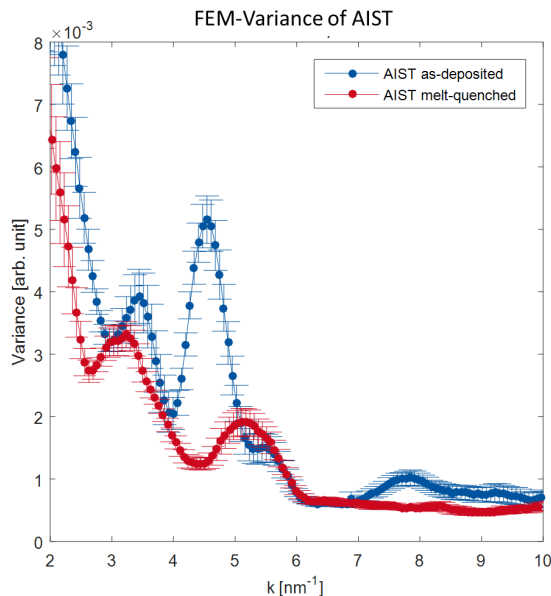


Figure 66: The variance in relation to the scattering vector k shows increased MRO in the as deposited state of AIST even without a correction for thickness.

To eliminate effects of thickness variations, the data were corrected by the method described in **Chapter 6.1.5.3**. **Figure 67** shows the corrected FEM plots of as deposited AIST and melt quenched AIST. After correction, the variance plots can be further compared in amplitude with higher accuracy. The first and second highest peak of as deposited AIST at $\sim 3.2 \text{ nm}^{-1}$ is much higher than the first and highest peak of melt quenched AIST. This reveals a higher MRO-contribution in as deposited AIST at $\sim 3.2 \text{ nm}^{-1}$. A similar case is found at the location of the third highest peak of as deposited AIST at $\sim 5.2 \text{ nm}^{-1}$. At the same location in reciprocal space melt quenched AIST shows the second peak. Again the variance is higher in the as deposited state indicating a higher MRO-contribution to the variance signal. At $\sim 3.2 \text{ nm}^{-1}$ and $\sim 5.2 \text{ nm}^{-1}$ as deposited AIST and melt quenched AIST show MRO-contributions. The MRO-contribution is stronger pronounced in the as deposited case. A different case is visible at $\sim 4.3 \text{ nm}^{-1}$. While the FEM plot of as deposited AIST shows its highest peak there, the FEM plot of melt quenched AIST shows a minimum. The minimum in variance at this k value indicates a weak or no MRO-contribution to the variance signal. Similar is the case at $\sim 7.4 \text{ nm}^{-1}$. In the as deposited AIST there is a small peak visible, indicating some MRO-contribution to the variance signal. The variance of melt quenched AIST is missing this feature completely. The increase in variance at $\sim 8.5 \text{ nm}^{-1}$ of the as deposited variance plot is probably an artefact known for specimen thicknesses close to the electron mean free path (Bogle et al., 2010). As deposited AIST shows more and overall higher peaks in the FEM data compared to melt quenched AIST. These indicate a higher MRO-contribution to the variance signal at these locations in reciprocal space and an overall higher MRO of the as deposited state of AIST in general.

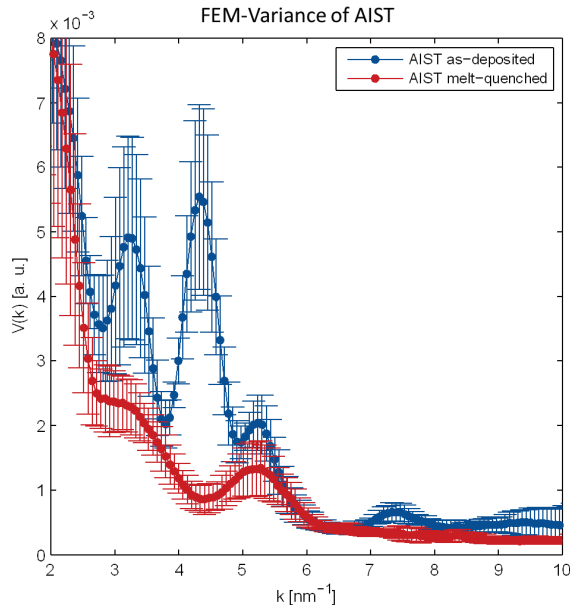


Figure 67: The thickness corrected variance in relation to the scattering vector k shows increased MRO in the as deposited state of AIST.

7.1.2.2 FEM of GeTe cross sections

Figure 68 shows the uncorrected FEM data of as deposited GeTe and melt quenched GeTe. Between the as deposited GeTe and the melt quenched GeTe, the variance graphs show a significant offset to each other. This is an effect caused by differences in thickness. In both plots a peak at ~ 3.2 nm⁻¹ and at ~ 5.4 nm⁻¹ are visible. **Figure 69** shows the thickness corrected FEM data of as deposited GeTe and melt quenched GeTe. In the corrected data the offset of the data has vanished and now the peak heights are comparable.

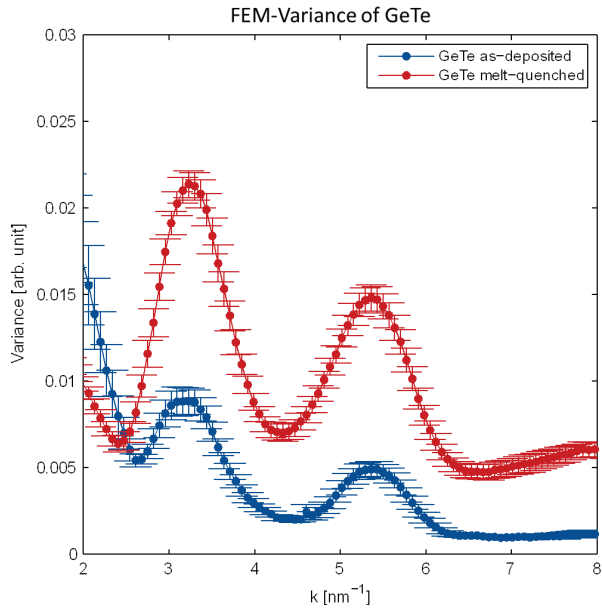


Figure 68: The variance of as deposited and melt quenched GeTe in relation to the scattering vector k . A comparison of peak heights is difficult because of an offset caused by thickness variations.

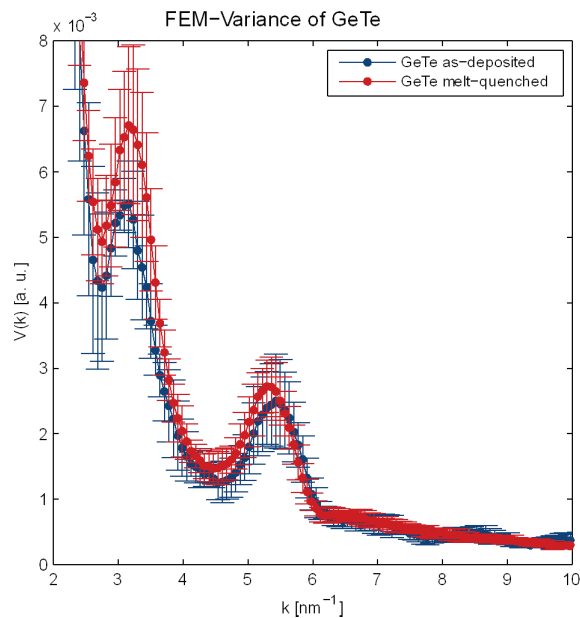


Figure 69 The thickness corrected variance V in relation to the scattering vector k shows comparable peaks in as deposited and melt quenched GeTe without the offset. Higher variance peaks of melt quenched GeTe indicate increased MRO compared to the as deposited state.

As deposited GeTe and melt quenched GeTe have the same amount of peaks and minima. Their highest and their second highest peak are at similar locations in reciprocal space. This indicates that in both states there is MRO of similar kind. Both peaks are higher in the melt quench state. This indicates that the MRO in the melt quenched state is more pronounced than in the as deposited state.

7.2 TEM investigations of AIST line-cell cross sections

FIB cross sections of an as produced crystalline AIST line cell as reference and an AIST line-cell after electrical switching into the reset state were investigated by bright field TEM. **Figure 70** shows an overview of the cross section of crystalline reference AIST line cell. The region of interest is the AIST beneath the gap of the two electrodes.

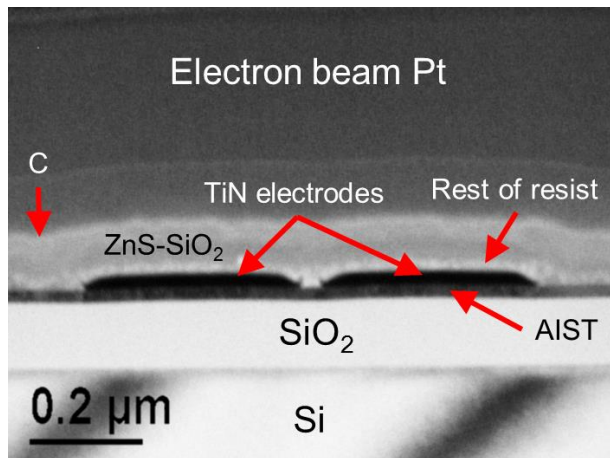


Figure 70: Shown is an overview bright field TEM image of the reference line cell. The different materials are clearly visible and labeled.

Figure 71 shows a closer look at the gap between the electrodes. The AIST layer appears to be crystalline. This is indicated by Bragg contrast throughout the whole layer. The specimen was tilted around the alpha axis of the specimen holder between 15° and -15°. Crystals in Bragg condition appear dark by their diffraction of the electron beam in relation to orientation.

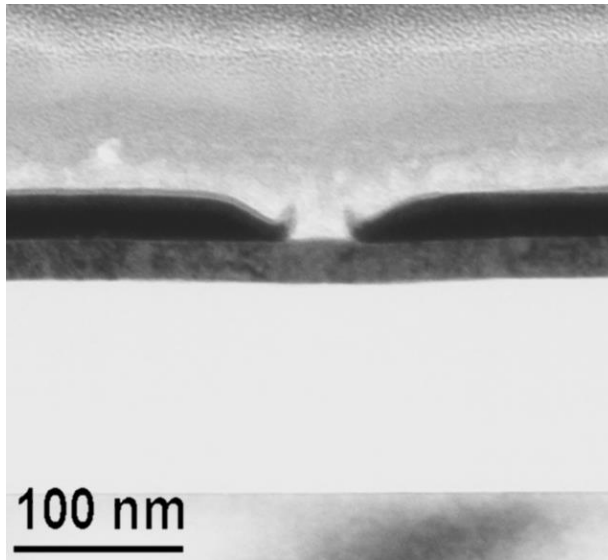


Figure 71: Shown is a closer look at the gap between the electrodes of the reference line cell. Even at this magnification dark Bragg contrast of grains can be seen through the whole AIST layer.

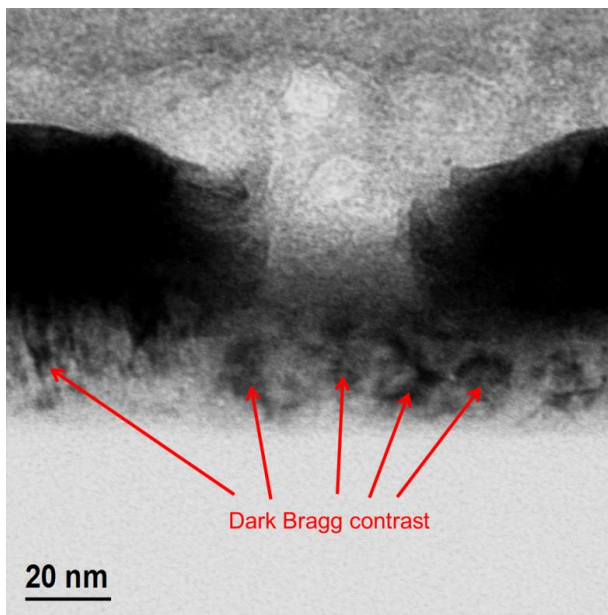


Figure 72: Shown is a bright field TEM image at +15° alpha tilt of the reference line cell. Dark Bragg contrast of grains in the AIST layer shows the crystallinity of the AIST layer.

Figure 72 shows a closer look at the AIST layer of the gap at +15° tilt. The dark Bragg contrast of the grains, shown at +15° tilt, prove the crystallinity of the AIST

layer. The dark contrast of the grains appears and disappears while the specimen is tilted.

Figure 73 shows a bright field TEM overview of the cross section of the electrically switched AIST line cell in the reset state. The investigated cell was switched by an electrical pulse with a pulse width of 10 ns and an amplitude of 9 V. The overview bright field TEM image of the switched cell looks very similar to the reference cell overview. It has to be noted that, because of slight differences in design between the reference and the switched cell, the reference has a longer AIST line and a smaller gap between the electrodes.

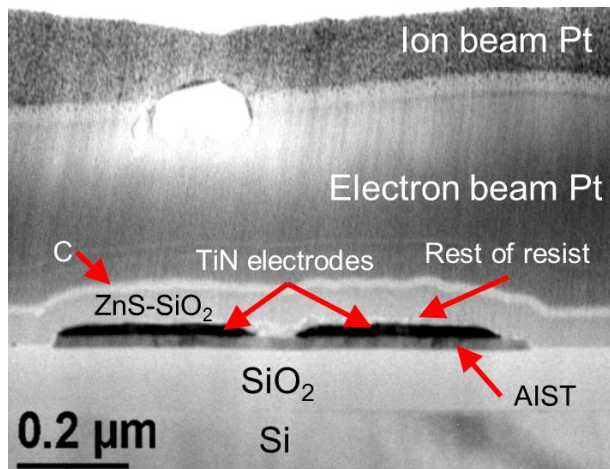


Figure 73: Shown is an overview bright field TEM image of the electrically switched line cell. The different materials are clearly visible and labelled.

Figure 74 shows the gap at higher magnification. The AIST layer beneath the electrode gap lacks dark Bragg contrast. But the grey of the AIST material beneath the gap changes from a brighter grey at the left side of the gap to a darker grey on the right. This indicates changes in the amount of diffracted electrons. To clarify the phase state, the specimen was tilted around the alpha axis of the TEM holder from 15° till -15° degree.

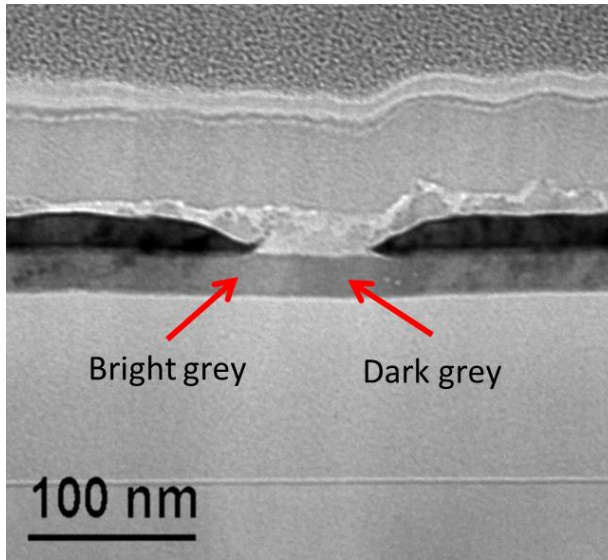


Figure 74: Shown is a closer look at the gap between the electrodes. The AIST layer beneath the electrode lacks dark Bragg contrast of orientated grains. The grey of the AIST material beneath the gap is on the left hand side brighter than on the right hand side.

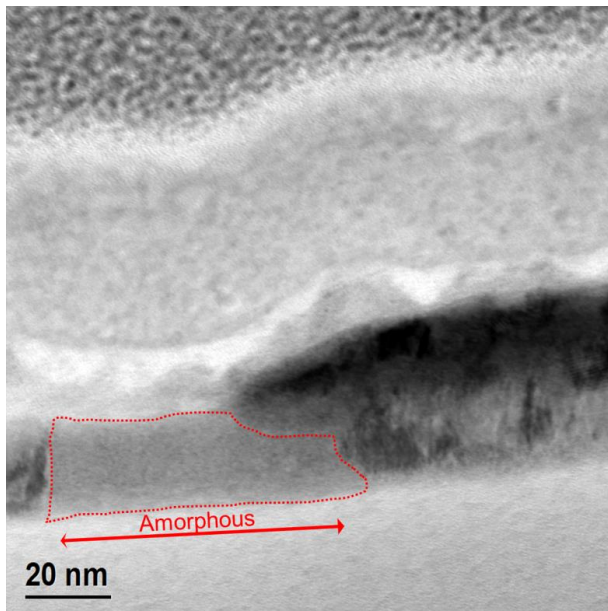


Figure 75: Shown is a bright field TEM image of the AIST layer beneath the electrode gap at 15° tilt. The diffuse grey amorphous part in the AIST layer can be clearly distinguished.

Figure 75 shows a bright field TEM image of the gap at 15° tilt. In **Figure 75** it is clearly visible that in the electrically switched AIST line cell an amorphous part has

formed. The amorphous part starts exactly where the darker grey of material starts in **Figure 74**. The bright grey part changes contrast depending on tilting angle. Therefore, it is considered to be Bragg contrast. Therefore not the complete AIST layer beneath the gap has transformed into the amorphous state. The amorphous material is closer to the right electrode and some amorphous material is beneath the right electrode. The right electrode was the anode in the switching process. The amorphous region keeps its contrast stable while it is tilted. In both line cells, rests of the resists are visible between the capping and the layers below. The rests of the resists are leftovers of the lithography steps.

7.3 Nano area electron diffraction of Sb_2Te_3 platelet intermediates

Intermediate products on the reaction path of a solvothermal synthesis of Sb_2Te_3 hexagonal platelets were investigated by ADF STEM imaging and NAED. The intermediate products were scanned by a 2 nm (**Chapter 6.1.5.2**) sized almost parallel and coherent electron beam in a FEI Titan dedicated STEM at 300 kV (Heggen et al., 2016). At every scanning position, a NAED pattern was acquired. The whole intermediates were scanned by 15 x 15 scanning points but only NAED patterns of characteristic specimen regions are shown here. T. Saltzmann identified four different intermediates by SEM that are formed on the reaction path of the solvothermal synthesis of the Sb_2Te_3 hexagonal platelets. Every intermediate is the main reaction product of the stopped reaction at the time (Saltzmann, 2014; Saltzmann et al., 2015). The intermediates 2, 3 and 4 were investigated by NAED. **Figure 76** shows the ADF STEM image of an intermediate 2 and NAED patterns of crystalline and amorphous regions. The NAED patterns reveal that only the brighter core of the intermediate is crystalline and the surrounding of it is amorphous. Only at the core, bright diffraction discs are visible, proving crystallinity. The surrounding shows diffuse rings and no diffraction discs in the NAED pattern, which indicates amorphous material. In the surrounding layer black spots are visible. These spots are probably holes or regions of thinner material. Some regions are brighter in the surrounding which might indicate additional layers of material.

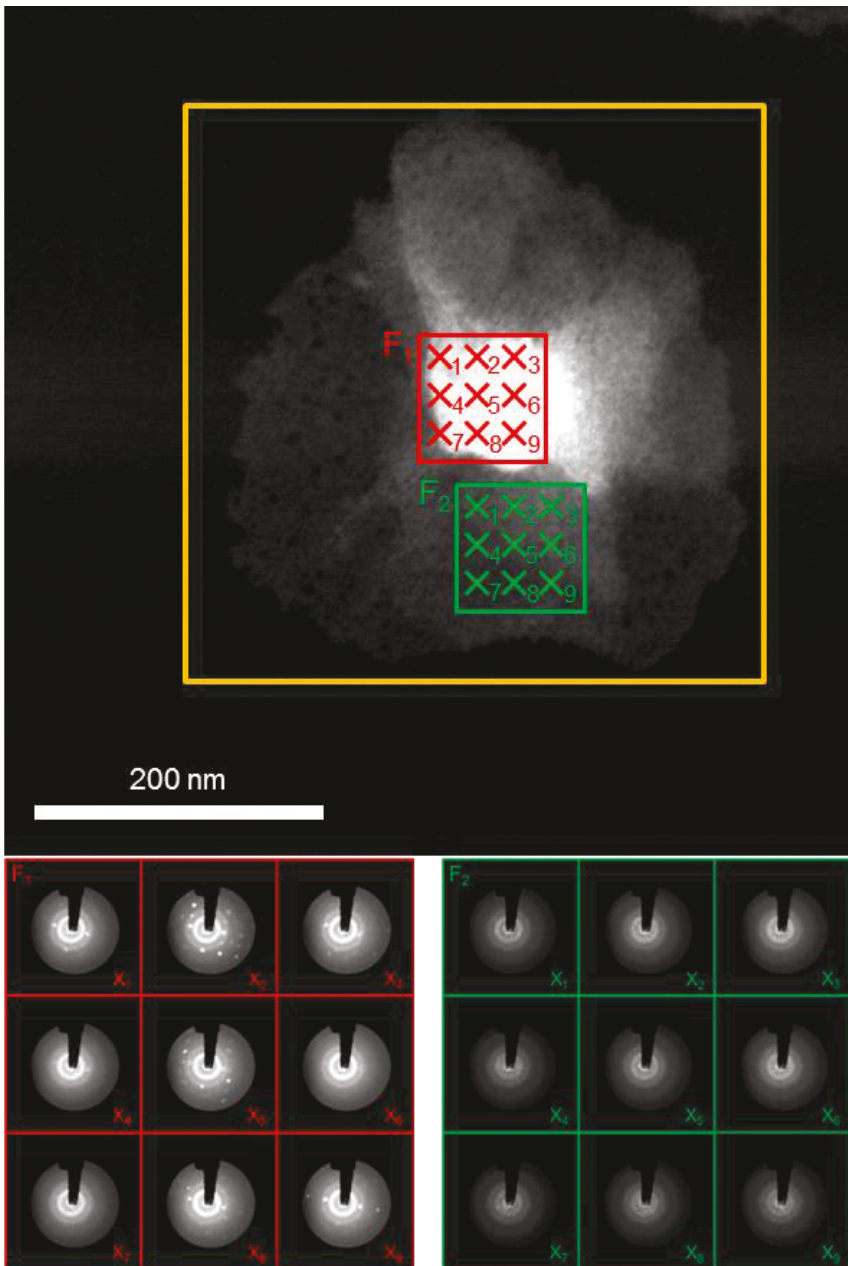


Figure 76: Shown is an ADF STEM image of an intermediate 2. The yellow frame marks the size of the 15 x 15 NAED scanning grid. F_1 and F_2 are selected 3 x 3 NAED scanning grids which NAED patterns are shown below the ADF STEM image. (F_1) In the core of the intermediate 2 crystalline NAED patterns can be observed. (F_2) The surrounding of the intermediate is completely amorphous showing diffuse NAED patterns.

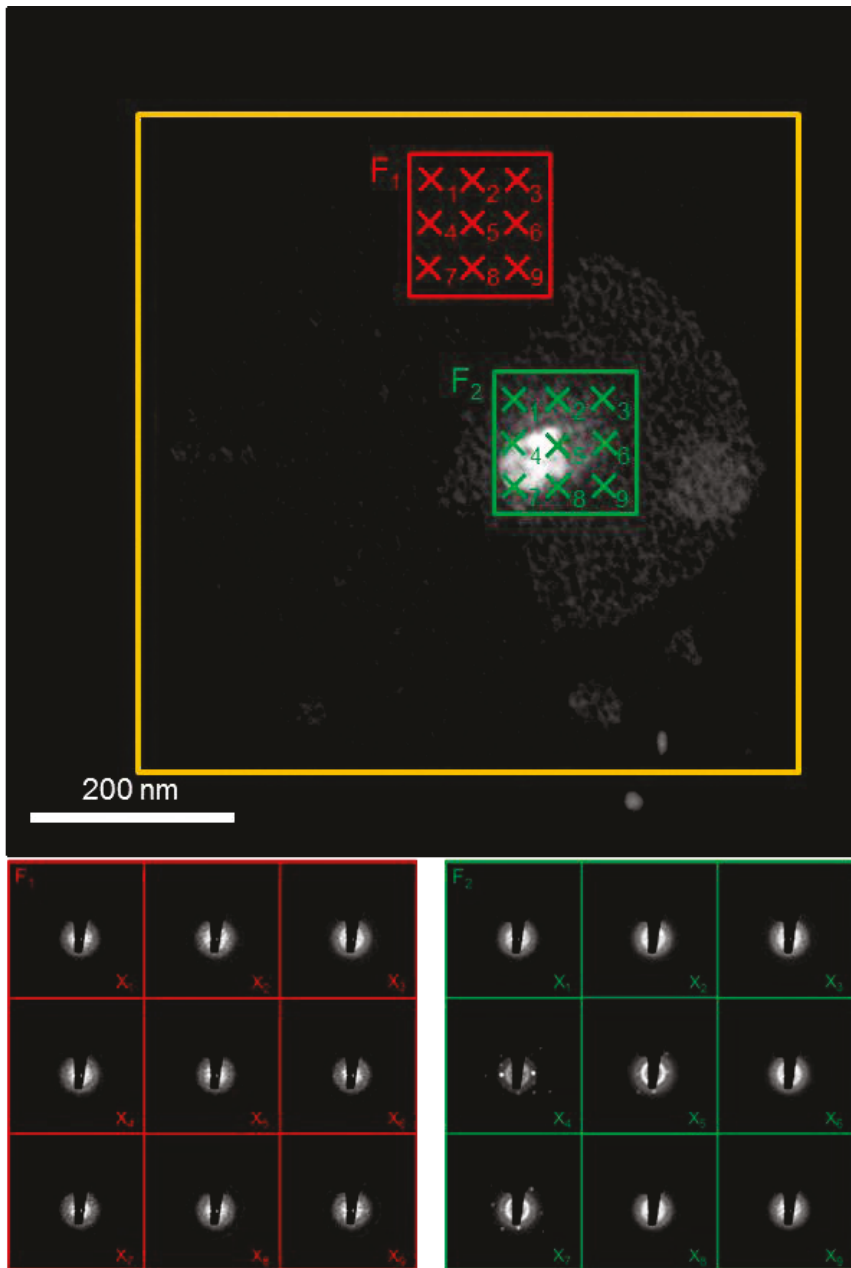


Figure 77: Shown is an ADF STEM image of an intermediate 2. The edges of the surrounding seem to form in a vague hexagonal shape. The yellow frame marks the size of the 15 x 15 NAED scanning grid. F₁ and F₂ are selected 3 x 3 NAED scanning grids which NAED patterns are shown below the ADF STEM image. (F₁) The surrounding of the intermediate is completely amorphous showing diffuse NAED patterns. (F₂) In the core of the intermediate 3 crystalline NAED patterns can be observed.

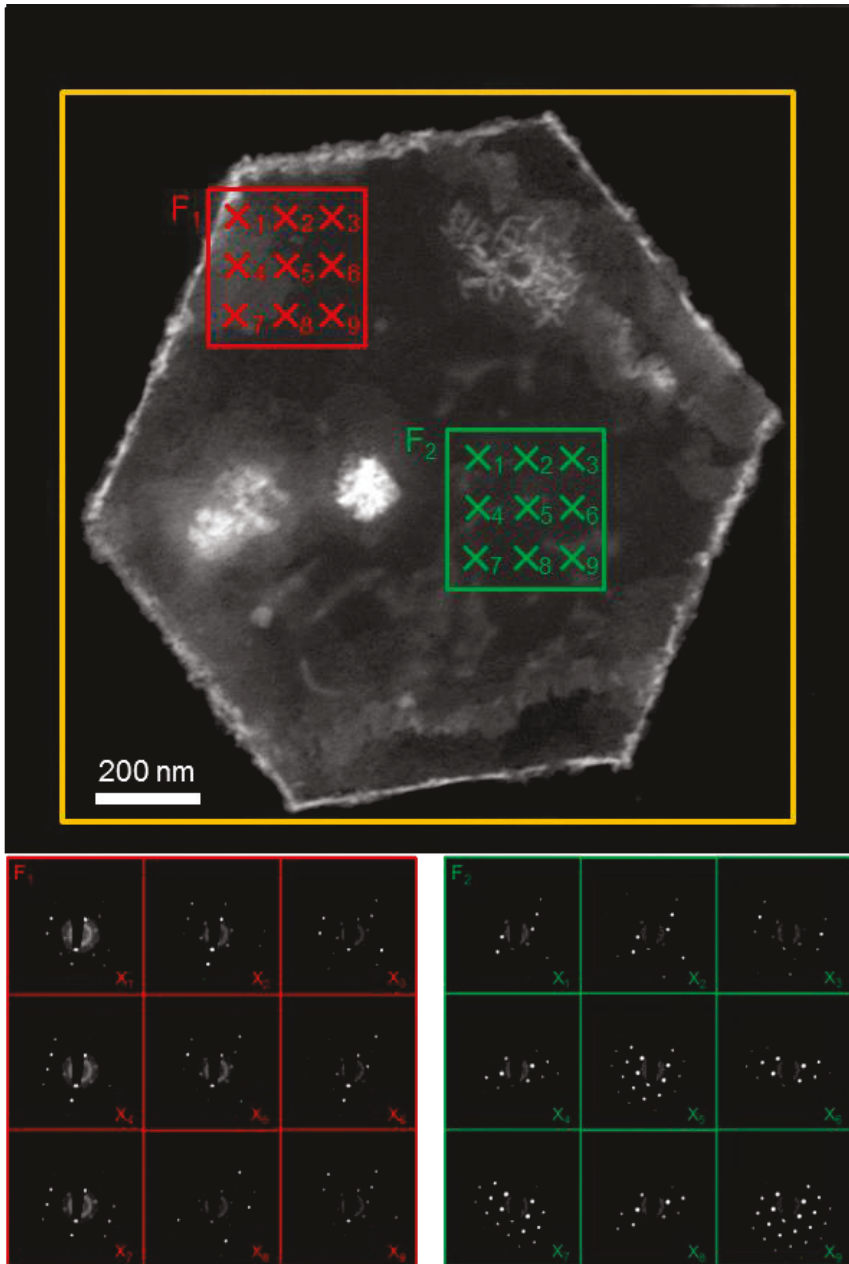


Figure 78: Shown is an ADF STEM image of an intermediate 4. The yellow frame marks the size of the 15 x 15 NAED scanning grid. F_1 and F_2 are selected 3 x 3 NAED scanning grids which NAED patterns are shown below the ADF STEM image. (F_1) Shown is a NAED pattern at a scanning point where additional material is seen on top of an intermediate 4. This results in additional diffraction spots. (F_2) The main hexagonal NAED pattern can be seen throughout the whole crystalline hexagonal shaped intermediate.

Figure 77 shows the ADF STEM image of an intermediate 3. The NAED patterns reveal again that only the brighter core of the intermediate 3 is crystalline and the surrounding of it is amorphous. The surrounding approaches a vague hexagonal shape. Only in the bright core region diffraction discs are visible. The surrounding shows diffuse rings and no diffraction discs, which are prove the surrounding is amorphous. The surrounding shows variations in thickness these cause variations in contrast. Again additional layers of material are visible by appearing brighter in the ADF STEM image. **Figure 78** shows the ADF STEM image of an intermediate 4. The complete intermediate 4 is crystalline at every scanning position. Furthermore the intermediate 4 shows single crystallinity throughout the main layer. The intermediate 4 has a clear hexagonal shape and is surrounded by a brighter rim. Only at scanning points with additional material on top of the continuous layer, additional diffraction spots are visible. This indicates additional crystalline layers of material in different orientations. **Figure 79** shows one chosen hexagonal NAED pattern of the shown intermediate 4 indexed by simulation of the diffraction pattern of Sb_2Te_3 by the software jems (Stadelmann, 2016). We used structure data of Anderson and co-workers for generating a simulated diffraction pattern of Sb_2Te_3 (Anderson & Krause, 1974). The intermediate 4 is viewed along the $[0001]$ direction which is orthogonal to the carbon layer of the copper grid. The hexagonal structure is easily visible in the NAED pattern. The imaged NAED pattern fits very well to the simulation.

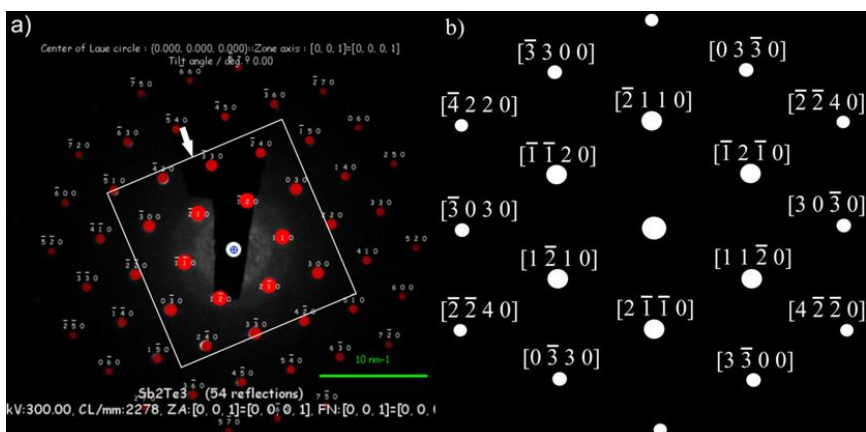


Figure 79: (a) Shown is a NAED pattern of an intermediate 4 with an overlay of the simulated hexagonal Sb_2Te_3 structure viewed along the $[0001]$ direction. (b) Closer view of the simulated and in Miller-Bravais notation indexed hexagonal Sb_2Te_3 structure viewed along $[0001]$ direction.

7.4 TEM/STEM investigations of a $\text{Ge}_1\text{Sb}_2\text{Te}_4$ layer grown by MOVPE

S. Riess of the Peter Grünberg Institut 9 deposited GST 124 on Si (111) in the stable phase by MOVPE (Riess, 2017). The deposited layer of GST 124 on Si (111) does not completely cover the whole substrate surface with homogenous thickness. There are orientated terrace steps visible. These are caused by the preferred growth directions of the GST 124 crystallographic orientations (**Figure 80**). In the publication of Schuck and co-workers a detailed description of the coverage of the Si substrate by GST 124 in relation to deposition parameters is found (Schuck et al., 2015).

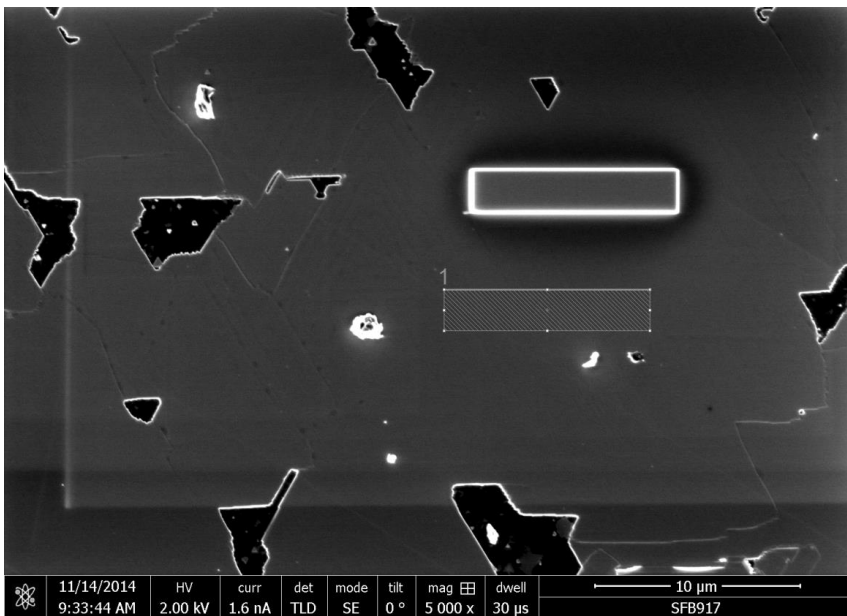


Figure 80: Shown is a SEM image of a chosen preparation site for a cross section TEM lamella of GST 124. The rectangle with the bright edges is a deposited platinum protection layer. The numbered rectangle is a marker of the dual beam FIB/SEM software and was used before to mark the deposition site.

A lamella is prepared in parallel to these steps to cut the cross section oriented close to a high symmetric zone axis. A homogeneous closed part of the layer was chosen for preparation (**Figure 80**). A cross section TEM lamella (**Chapter 6.3.7**) of the sample is prepared. The lamella is thinned and cleaned until a hole has formed at the interface between silicon and GST 124 (**Figure 81**). In the SEM image of the 47° degrees tilted lamella the layer stack is visible. It consists from top to bottom out of ion beam deposited platinum, an interface layer between ion beam deposited

platinum and electron beam deposited platinum, electron beam deposited platinum, a carbon layer, the GST 124 layer and silicon substrate (**Figure 81**).

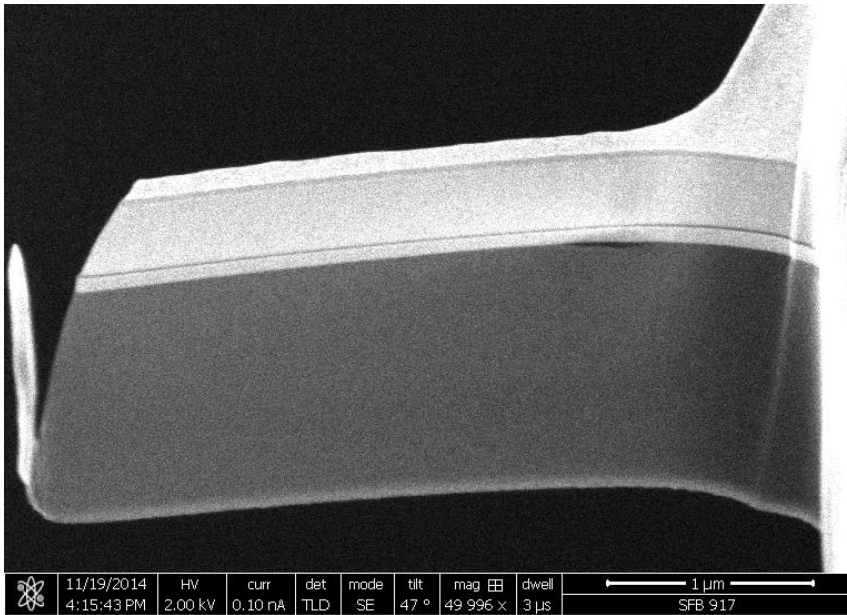


Figure 81: Shown is a SEM image of the thinned lamella in side view. A small hole can be seen beneath the GST 124 layer and the silicon substrate.

7.4.1 TEM investigations of a $\text{Ge}_1\text{Sb}_2\text{Te}_4$ layer

The GST 124 on Si (111) lamella is investigated by bright field TEM. A Tecnai F20 from FEI at 200 kV was used for the investigation. An overview of the lamella shows the different layers, which are already distinguishable in the SEM. Regions which were damaged by FIB are also visible. The GST 124 layer has a uniform thickness over the whole range of the lamella with the exception of the hole cut by the FIB (**Figure 82**). At higher magnification, smaller FIB damage artefacts in the silicon at the silicon GST 124 interface are observable (**Figure 83**).

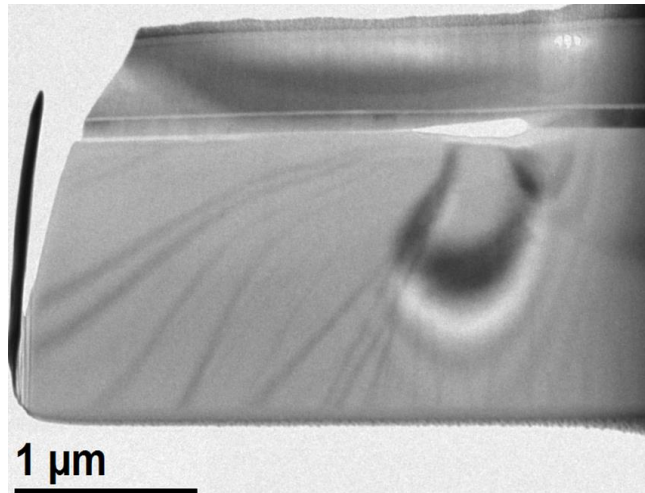


Figure 82: Shown is a bright field TEM overview image of the GST 124 lamella.



Figure 83: Bright field TEM image shows additional FIB damage artifacts. Also a planar defect can be seen in the GST 124 layer that runs through the whole lamella with uniform thickness. Image reprinted with acknowledgment from the publication of H. Hardtdegen and co-workers (Hardtdegen et al., 2016).

The GST 124 layer is single crystalline but not defect free. There are no grains visible even by tilting between $+15^\circ$ and -15° degree around the axis of the lamella. There is a lamellar defect visible. The defect runs through the whole observed GST 124 layer with uniform thickness (Figure 83). At even higher magnification, sublayers of the

GST 124 layer are observable. The lamellar defect is also clearly distinguishable. The GST 124 layer consists of three parts. The first part is 13.4 nm thick and ranges from the silicon interface to the lamellar defect. The lamellar defect has a thickness of 11.8 nm. The last part reaching from the planar defect to the carbon layer interface is 74.6 nm thick. All three parts show a similar layered structure. The interface between GST 124 and Carbon is not completely flat. There are some pores or gaps which are filled up with carbon. Except for the lamellar defect, the material is single crystalline. The brighter and darker regions are formed by bending of the thin lamella. Different parts of the single crystal are in Bragg condition depending on the orientation of the lamella to the electron beam (**Figure 84**). (Williams & Carter, 2009).

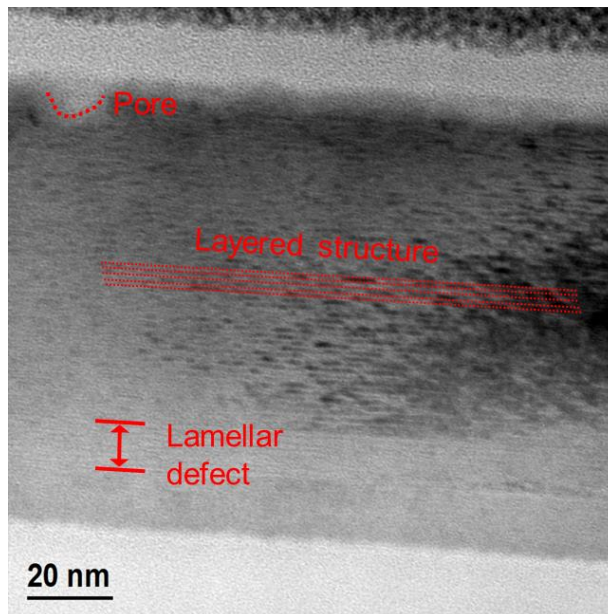


Figure 84: The GST 124 layer imaged by bright field reveals the sublayers of the GST 124 layer itself. A lamellar defect can be observed by its slightly different contrast. The GST 124 carbon interface has some pores or gaps that are filled by carbon deposition.

7.4.2 HAADF HRSTEM investigations of a $\text{Ge}_1\text{Sb}_2\text{Te}_4$ layer

To investigate the crystal structure of the GST 124 Layer in more detail, the cross section lamella was investigated at 200 kV in a Cs-corrected FEI Titan 80-200 ChemiSTEM dedicated STEM (Kovacs et al., 2016). The investigation was done together with H. Du from the GFE. Viewed along the [210] direction, the lamellar defect, which can be seen in the TEM bright field image (**Figure 83**), is invisible and

could not be found in HAADF HRSTEM images. This indicates that the previously seen defect is a twin. The atomic arrangement in this perspective has to look the same for the investigated structure orientation and its twin counterpart of GST 124. In the HAADF HRSTEM images the highly ordered sublayer structure of the GST 124 layer is visible. The structure is composed of bands of atoms separated by dark lines. These are probably van der Waals gaps (**Figure 85**). This structure causes the layered appearance already seen in lower magnification TEM bright field images.

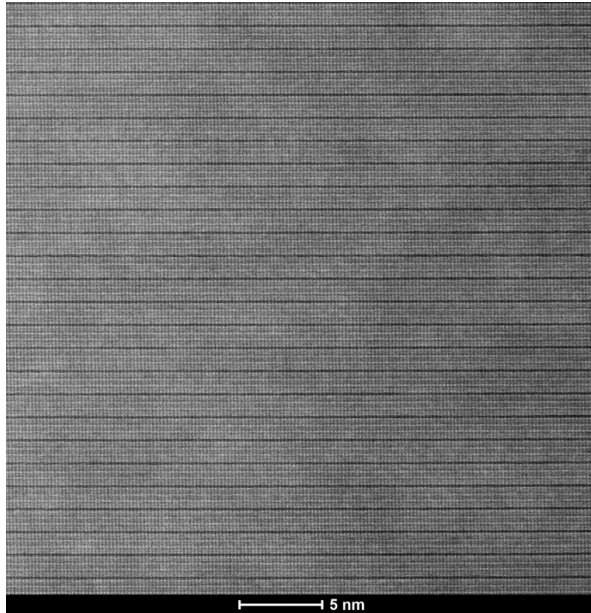


Figure 85: The layered structure of the GST 124 material can be clearly observed in the HAADF HRSTEM image (Hardtdegen et al., 2016).

A simulation of the diffraction pattern by the software JEMS for the structure found by Matsunaga and co-workers viewed along the [210] direction is in very good agreement with the Fourier transformation of the imaged atom stacking (**Figure 86**) (Matsunaga & Yamada, 2004; Stadelmann, 2016). From the shown Fourier transformation pattern the lattice constants a and c are derived. The values are $a = 0.42$ nm and $c = 4.04$ nm with an error of around 0.1 nm.

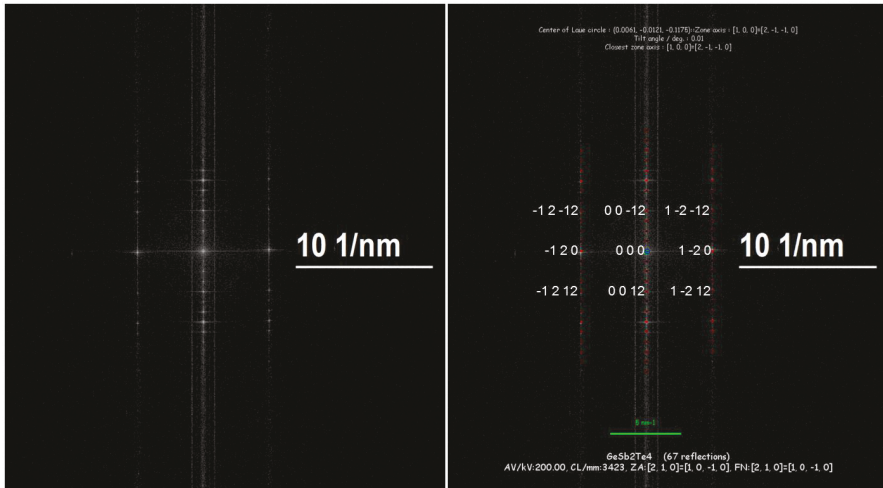


Figure 86: Shown is the Fourier transformation of the HAADF HRSTEM image of GST 124 (left image). The Fourier transformation agrees well with the simulated GST 124 structure (right image) (Matsunaga & Yamada, 2004).

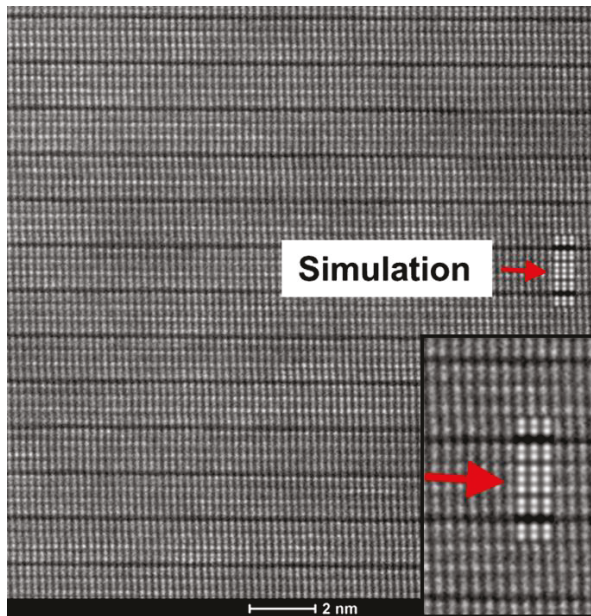


Figure 87: The HAADF HRSTEM image shows good agreement with the overlaid shown HAADF HRSTEM simulation performed with the software Dr. Probe on basis of the data of Matsunaga and co-workers (Matsunaga & Yamada, 2004; Barthel, 2012).

At higher magnification the structure can be seen in more detail. Always seven atoms per band are sandwiched between the van der Waals gaps. Matsunaga proposed a gap-Te-Ge₂₅Sb₇₅-Te-Ge₅Sb₅-Te-Ge₂₅Sb₇₅-Te-gap structure. Based on the structure found by Matsunaga and co-workers, a simulation of the HAADF image was

performed. (Matsunaga & Yamada, 2004). The Dr. Probe software was used for this task (Barthel, 2012). The simulated image fits very well into the acquired one (**Figure 87**). Even the slightly bigger atom-to-atom distances separating the three atoms in the middle of the two outer atoms of the seven atom bands can be seen in the simulation and also in the image. In the HAADF STEM image the horizontal positions of the atoms at the top of the image are slightly shifted to the left in comparison to atoms further below. This is a result of the sample drift while the STEM image is acquired. Imaging of the silicon interface reveals the thickness of the disturbed region of adaption between the silicon viewed along the [211] direction and the GST 124 viewed along the [210] direction. This region has a thickness of around 2.04 nm. After this adaption region the GST 124 is perfectly ordered (**Figure 88**).

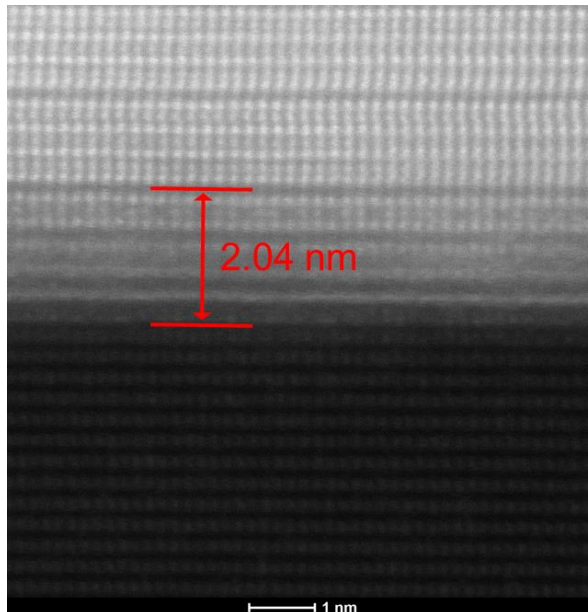


Figure 88: Shown is a HAADF HRSTEM image of the interface between the silicon substrate and the GST 124 layer. The adaption of the GST 124 structure to the Si substrate is observable. After the adaption the GST 124 is perfectly ordered (Hardtdegen et al., 2016).

8 Discussion

In the following sections the results from **Chapter 7** will be discussed. The discussion is structured in four main parts. The four parts are the crystallization kinetics of AIST and GeTe thin films, the TEM investigation of AIST line cell cross sections, Nano area diffraction of Sb_2Te_3 platelet intermediates and the TEM/STEM investigation of a GST 124 layer grown by MOVPE.

8.1 Crystallization kinetics of AIST and GeTe thin films

In this work, the growth velocities of AIST in the as deposited and in the melt quenched state were measured. It has been shown that the growth velocities of melt quenched AIST is around 1.5 orders of magnitude higher than in the as deposited state. **Figure 89** compares the measurements and simulations of growth velocities of AIST produced by different methods.

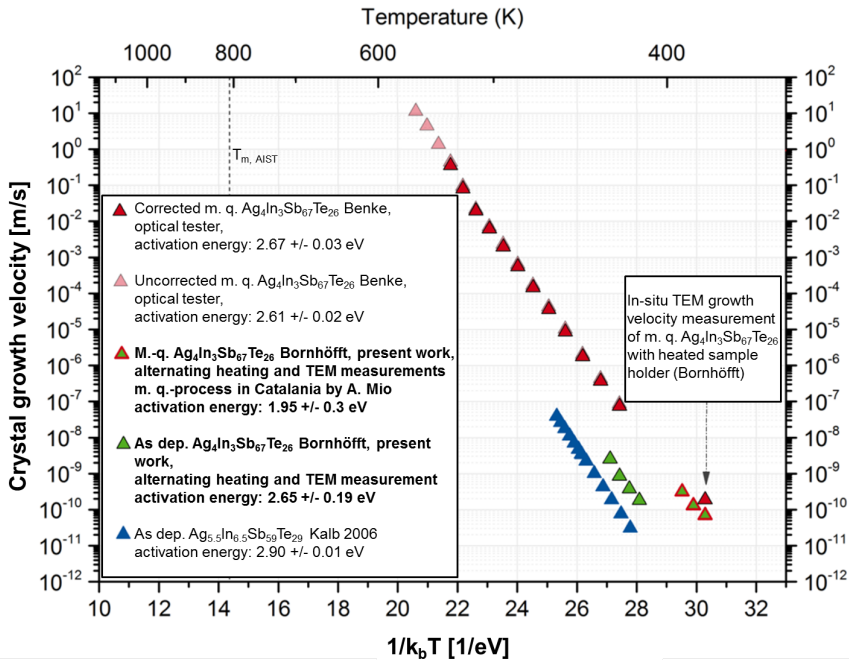


Figure 89: Shown are measured and calculated growth velocities of as deposited and melt quenched AIST performed by different methods in comparison (Kalb, 2006; Bornhöfft, 2012; Kaldenbach, 2012; Benke, 2017). Image reprinted and amended with permission from the thesis of J. Benke (Benke, 2017).

The TEM measurements show that the knowledge of the measured amorphous state, namely the as deposited and the melt quenched state, is very important. The

values and the Arrhenius behaviour of the melt quenched AIST data fit very well to the growth velocities of melt quenched AIST measured at higher temperatures in the optical tester setup of the I. Physikalisches Institut (Salinga et al., 2013; Benke, 2017). This shows that the growth velocity data of AIST acquired by the optical tester by measuring the reflectivity are valid. The data of this work help also to understand the difference of the measured data of melt quenched AIST in the optical tester of the I. Physikalisches Institut (Salinga et al., 2013; Benke, 2017) to the measured growth velocity data of as deposited AIST measured by atomic force microscopy (AFM) (Kalb, 2006). The reason for the big difference in growth velocity is the as deposited state of the AIST material investigated by Kalb. This is evident because the growth velocities of the as deposited AIST, measured in this work by TEM, are much closer to Kalb's AFM data. Kalb's samples have the same thickness as the samples in this work. There is probably an additional contribution to a difference in growth velocity values by the difference in stoichiometry between AIST used in this work and in the work of Kalb. Furthermore Kalb used uncapped samples that are not protected against oxidation. There is also a difference between the in situ TEM heating experiment of the master thesis of the present author and the values gathered in this work. The increased growth velocity of melt quenched AIST, measured in the master thesis, is most likely based on a higher temperature uncertainty of the in situ heating holder used. The acquired data in this work shows the big influence of only 5 K difference in temperature. The in situ heating TEM holder had an error of around 10 K (Bornhöfft, 2012). The measured AIST growth velocities of the as deposited and the melt quenched states of all measurement series show Arrhenius behaviour indicating that they are in a glassy state. It is referred to the thesis of J. Benke and the publication of M. Salinga and co-workers (Salinga et al., 2013; Benke, 2017) for a more detailed comparison of the measured and also simulated growth velocities for the different methods.

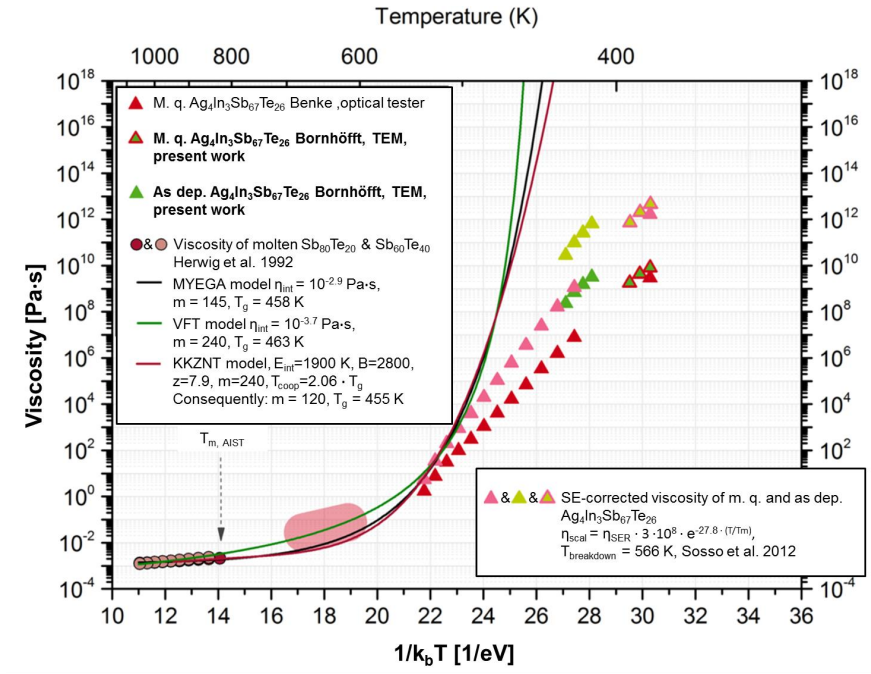


Figure 90: Shown are the calculated viscosities for as deposited and melt quenched AIST from the data of the optical tester, TEM and Kalb’s AFM measurement (Kalb, 2006; Benke, 2017). Also shown are the calculated viscosity curves of AIST as a super cooled liquid on the basis of three different theoretical models. Image reprinted and amended with permission from the thesis of J. Benke (Benke, 2017).

By the application of the Stokes-Einstein relation, J. Benke calculated the viscosities from the growth velocities of AIST. The viscosities were calculated for the data of the optical tester, TEM and the AFM (Kalb, 2006; Benke, 2017). **Figure 90** shows the calculated viscosities. The very high fragility of AIST and its Arrhenius like behaviour over more than nine orders of magnitude for the melt quenched state was already shown in the publication of Salinga and co-workers (Salinga et al., 2013). In **Figure 90** the expected plot of the super cooled liquid state of AIST calculated by J. Benke with three different models is shown (Benke, 2017). She used the Mauro-Yue-Ellison-Gupta-Allan (MYEGA) model (Mauro et al., 2009), the Vogel-Fulcher-Tamman model (Vogel, 1921; Fulcher, 1925; Tamman & Hesse, 1926) and the Kivelson-Kivelson-Zhao-Nussinov-Tarjus (KKZNT) model (Kivelson et al., 1995). She corrected the viscosity also by a temperature-dependent factor according to the work of Sosso and co-workers (Sosso et al., 2013a).

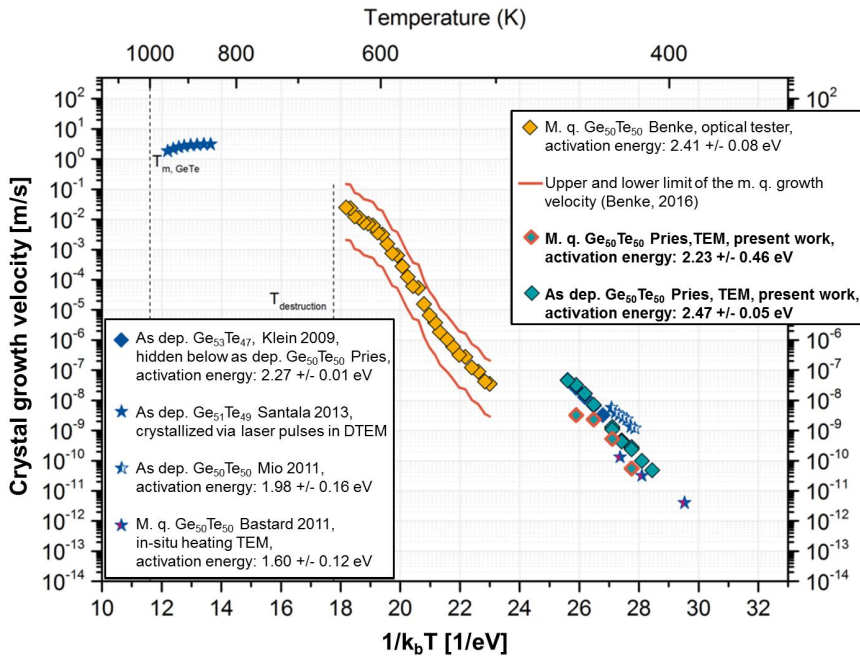


Figure 91: Shown are measured and simulated growth velocities of as deposited and melt quenched GeTe performed by different methods in comparison (Klein, 2009; Bastard et al., 2011; Mio et al., 2011; Santala et al., 2012; Pries, 2015; Benke, 2017). Image reprinted and amended with permission from the thesis of J. Benke (Benke, 2017).

It can be observed that the as deposited and the melt quenched state are both glassy states deviating at different points from the expected viscosity curve of a super cooled liquid. The as deposited AIST is in a glassy state that has a higher viscosity than the melt quenched state of AIST. That means the as deposited state is a more relaxed glass than the melt quenched state.

J. Benke and J. Pries also did an analysis on the data of the growth velocities of GeTe gathered by TEM and by the optical tester (Pries, 2015; Benke, 2017). **Figure 91** shows the measurements of growth velocities of GeTe by different methods. At the temperatures, which were used in the optical tester setup, nucleation events were encountered. These nucleation events were observed in the reflectivity data of the optical tester and in TEM investigation of recrystallized amorphous regions of the optical tester measurements. This means, GeTe shows nucleation dominated behaviour in the measured temperature range of the optical tester. J. Benke accounted for these deviations by the assumed upper and lower limits shown by orange lines in the graph (Benke, 2017). The growth velocity data of melt quenched

GeTe measured by TEM (Pries, 2015) vary from the originally measured optical tester data quite significantly. It fits better to the assumed upper limit of the growth velocity data acquired by the optical tester. This shows that the optical tester setup needs phase change material samples that are growth dominated in the measured temperature range, like AIST is, to measure growth velocities accurately. Furthermore, our TEM measurements prove to be essential references to confirm the acquired optical tester data. The in situ TEM growth velocity data of melt quenched GeTe acquired by Bastard and co-workers are in good agreement with our melt quenched GeTe TEM ex situ data of the growth velocities (Bastard et al., 2011). It has to be noted that Bastards data and our data are gathered at relatively low temperatures. At these temperatures GeTe shows mainly growth dominated behaviour (Bastard et al., 2011; Pries, 2015). This means that both methods have measured the pure growth velocities excluding effects of nucleation. The growth velocity data of as deposited GeTe measured by M. Klein by AFM (Klein, 2009) are in good agreement with our growth velocity data of as deposited GeTe. This is surprising because he uses a slightly different stoichiometry and no capping. Perhaps it is coincidence that the effects of both changes bring them close to our data. The growth velocity values of as deposited GeTe data measured by light microscopy by A. M. Mio (Mio et al., 2011) is increased compared to our data. Their films were not capped which could lead to oxidation influences. In light microscopy it is also difficult to separate grains, like it is possible in a TEM. Bigger length scales (few to tenth of micrometer) are used for the light microscope measurements. This makes it more difficult to exclude all unwanted nucleation effects in the measurements. It is referred to the thesis of J. Benke for an even more detailed comparison of the different data sets which also includes the simulation of G. C. Sosso and co-workers (Sosso et al., 2013b; Sosso et al., 2015; Benke, 2017).

The data sets of the growth velocity of GeTe show that it grows faster in the as deposited state than in the melt quenched state. That means, the melt quenched state has to be closer to the super cooled liquid state because of its higher viscosities (**Figure 93**). By the application of the Stokes-Einstein relation, J. Benke calculated the viscosities from the growth velocities of GeTe. The viscosities were calculated for the measured data of the optical tester and the TEM.

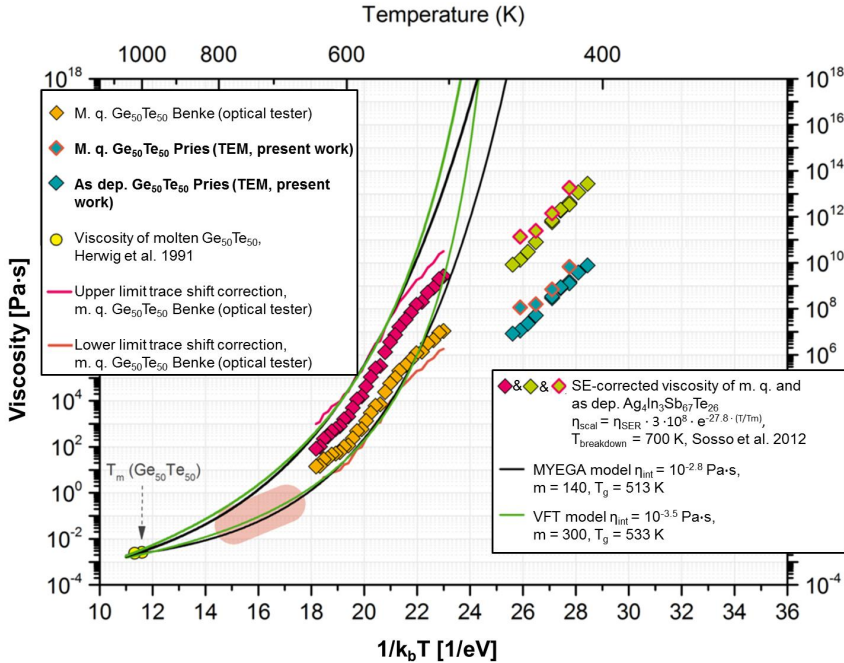


Figure 92: Shown are the calculated viscosities for as deposited and melt quenched GeTe from the data of the optical tester and TEM (Pries, 2015; Benke, 2017). Also shown are the calculated viscosity curves of GeTe as a supercooled liquid on the basis of two different theoretical models. Image reprinted and amended with permission from the thesis of J. Benke (Benke, 2017).

Figure 92 shows the viscosity data for as deposited and melt quenched GeTe and the viscosity calculated for the super cooled liquid of GeTe according to the MYEGA model (Mauro et al., 2009) and the VFT model (Vogel, 1921; Fulcher, 1925; Tamman & Hesse, 1926). The models were fitted for the assumed upper and lower limit of the optical tester data set. In **Figure 92**, the as deposited and the melt quenched state can be identified as different glassy states because of their Arrhenius like behavior and their differences in viscosity. J. Benke plotted the data using a correction for a temperature independent factor according to Sosso and co-workers (Sosso et al., 2013a). In the case of GeTe the melt quenched state is the more relaxed glass in contrast to AIST, where it is the as deposited state.

Another perspective to understand the growth velocities is the MRO of the different amorphous states of phase change materials. In the FEM measurements the corrected variance is always lower in the amorphous state that grows faster and is therefore the less relaxed glass. In the work of J. Benke und J. Pries the growth velocities and the variances of as deposited and melt quenched Sb₂Te were

measured and discussed (Pries, 2015; Benke, 2017). Here the same connection is observed. Higher variance means slower growth velocity which means higher glass relaxation. Lee and co-workers showed the connection between the MRO and the nucleation of AIST and GST 225 (Lee et al., 2014). In their work they reasoned that higher MRO lead to an increase in nucleation caused by a higher amount of subcritical nuclei. Light microscope measurements by J. Pries of the nucleation of GeTe and Sb₂Te in the as deposited and in the melt quenched state and the variance measurements of these materials come to similar results (Pries, 2015; Benke, 2017). Higher amounts of subcritical nuclei or preordered clusters could be a reason for a decrease of the growth velocity. The ordered regions have to be oriented in line with the growth direction or have to be dissolved. Both processes need energy. The peaks in the variance plots of the as deposited and melt quenched state of AIST in Lee and co-workers publication are comparable to the features of the melt quenched state of AIST in this work (Lee et al., 2009a). Both peaks in variance are at similar location in reciprocal space. In both cases, the first peak is the highest peak. Our absolute variance values are hardly comparable to Lee's work because of differences in specimen design, experimental conditions and also because of our correction procedure. Lee called amorphous regions of phase change material primed, which were laser irradiated but neither molten nor crystallized in this process (Lee et al., 2009a). The primed regions were adjacent to laser molten regions but the heating was not sufficient or long enough to melt the material or crystallize it. Our melt quenched state of AIST is very similar to the so called prime state of Lee with all variance peaks at similar locations in reciprocal space. In our melt quenched AIST, the second variance peak is the highest. In Lee's primed AIST the first peak is the highest. This is an indication for a slightly different number and distribution of the ordered clusters. Lee's as deposited and melt quenched state of AIST are very similar in regard of variance signal. The results of this work suggest that the growth velocities of Lee's as deposited and melt quenched state would be more similar to each other than in our case. Our as deposited state of AIST is very different to the melt quenched state regarding growth velocity and MRO. One reason for this could be differences in the production process of the layers. Differences in the high energetic sputter processes can lead to different amounts of MRO in the layer of as deposited AIST. That means that there is not only one defined as deposited state but the as deposited state is dependent on its deposition process. Also the layer

stacks are different. While Lee deposited the 30 nm thick AIST layer on a 40 nm thick Al_2O_3 layer, we used a 10 nm thick $(\text{ZnS})_{80}:(\text{SiO}_2)_{20}$ layer beneath our 30 nm thick AIST layer. Moreover, Lee has no capping layer. Perhaps the confinement of the capping layer could also influence the MRO, but the atom movement inside the AIST layer after the deposition process should be low at room temperature. An in depth study of the influence of a substrate or capping to the MRO does not exist so far. Lee does not mention the exact stoichiometry of his AIST layer. The stoichiometry is probably comparable to ours, because of the good match of the positions of the variance peaks in the FEM data. It is remarkable that Lee could reach a very similar state, compared to our as deposited AIST, by laser irradiation of his as deposited AIST. It seems to be possible to reach similar states of MRO by different deposition and treatment histories. Relaxation of glasses in direction of the super cooled liquid could be such a process. The exact glassy state is defined by the amount of relaxation. The results of the FEM data and the growth velocity measurements show that the MRO is coupled to the relaxation of the glassy state of phase change materials. **Figure 93** and **Figure 94** show schematically the connection between the glassy states of AIST and GeTe, their viscosities, their crystal growth velocities and their MRO. **Figure 93** summarizes that the melt quenched state of AIST is the state with the higher growth velocity, has less amount of MRO, and is a less relaxed glassy state with lower viscosity. Our as deposited state of AIST has lower growth velocities, higher amounts of MRO and is a more relaxed glass with higher viscosities. **Figure 94** summarizes that our as deposited state of GeTe is the state with the higher growth velocity, has a lower amount of MRO, and is a less relaxed glassy state with lower viscosity. The melt quenched state of GeTe has lower growth velocities, higher amounts of MRO and is a more relaxed glass with higher viscosities.

Medium range order influence on glassy state of AIST

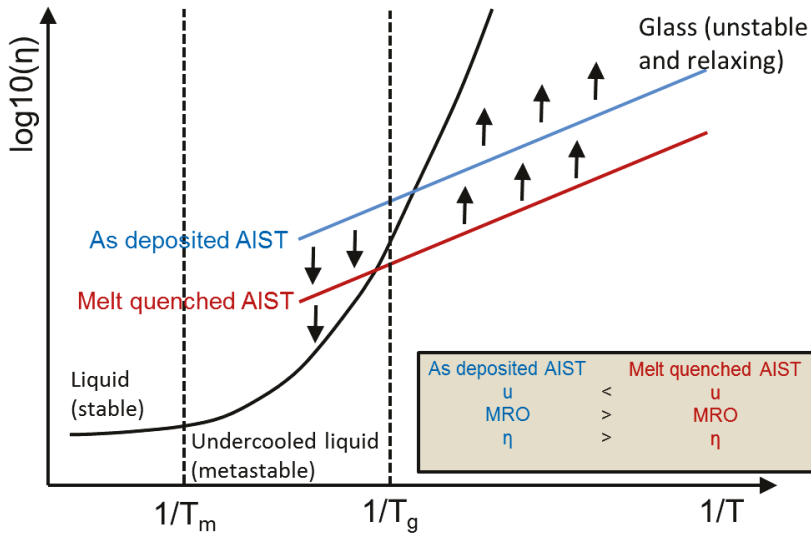


Figure 93: For AIST the melt quenched state is the state with the higher growth velocity u , has less amount of MRO, and is a less relaxed glassy state with lower viscosity η . Our as deposited state has a lower growth velocity u , higher amounts of MRO and is a more relaxed glass with a higher viscosity η .

Medium range order influence on glassy state of GeTe

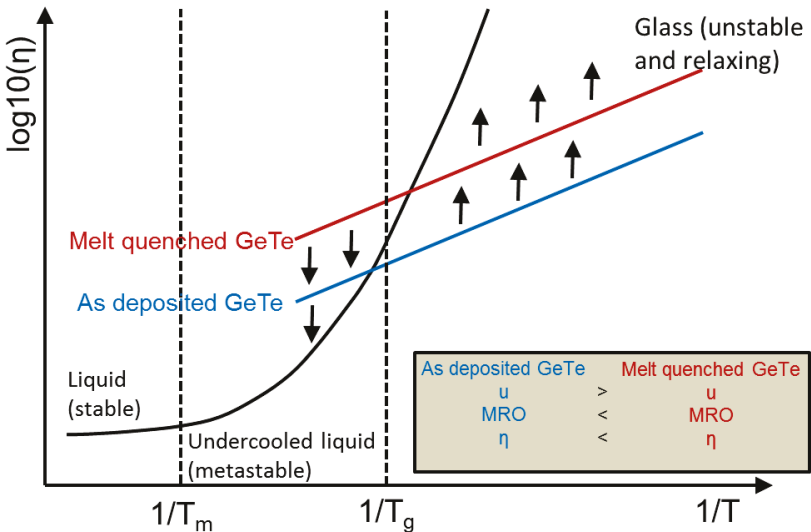


Figure 94: For GeTe our as deposited state is the state with the higher growth velocity u , has less amount of MRO, and is a less relaxed glassy state with lower viscosity η . The melt quenched glass state has a lower growth velocity u , higher amounts of MRO and is a more relaxed glass with a higher viscosity η .

Glasses are relaxing their viscosity value in direction of the viscosity value of the super cooled liquid (Raoux, 2009). From **Figure 90** and **Figure 92** it can be seen that this means higher viscosity values of AIST and GeTe for more relaxed states. From **Figure 93** it can be concluded that our melt quenched AIST, Lee's as deposited AIST and Lee's melt quenched AIST are less relaxed glassy states than our as deposited and Lee's primed state. Lee reached his primed state by laser heating and has shown that annealing also increases the variance signal of AIST. This is another strong indication that an increase in MRO through heating of the glassy AIST is a relaxation process towards the super cooled liquid state.

The investigation of AIST and GeTe in this work has shown that the growth velocity and the MRO are connected. Therefore we found a connection between the amount of relaxation in the phase change materials as glasses and the amount of their MRO. The amount of relaxation of phase change materials after deposition or melt quenching is found to be dependent on the composition of the phase change material. This explains the contradictory observations of the crystallization kinetics and MRO of AIST and GeTe in the as deposited and melt quenched state. AIST is relaxed more after the high energetic sputter process, while GeTe is relaxed more after quenching from the melt. The reason behind this is not completely clear yet. High amount of relaxation is coupled with high amount of MRO. This connection is valid for AIST, GeTe and was also found to be true for Sb_2Te (Pries, 2015; Benke, 2017). This could be a connection that is true for all phase change materials in glassy states or glasses in general.

FEM proves to be a powerful tool to investigate phase change materials and other materials in the amorphous phase. It gives information about the MRO of different amorphous states. With FEM it is possible to make profound assumptions over the behaviour of different amorphous states. FEM gives direct information if a change in nucleation or growth velocity of different amorphous state of phase change materials can be expected. FEM enables furthermore a comparison of the glass relaxation of amorphous states of phase change materials.

8.2 TEM investigations of AIST line-cell cross sections

By bright field TEM investigations of an as produced crystalline AIST reference cell and an electrically switched AIST line cell, the physical switching mechanisms of the line cells were demonstrated. A switching current with a pulse width of 10 ns and an

amplitude of 9 V was applied. This current heated part of the AIST layer high enough to melt it. The molten part is then quenched in the amorphous state. The amorphous part is not located at the center beneath the gap between the contacts. It is actually closer to the anode. This is a sign of horizontally inhomogeneous heat distribution between the electrodes. This is caused by the Thompson-Seebeck effect. The shift of the amorphous part to the anode is associated with p-type conduction. The same effect was reported in AIST phase change line cells by Castro and co-workers (Castro et al., 2007). In his thesis, J. Oosthoek observed the Thompson-Seebeck effect on his line cells, too (Oosthoek, 2014a). In both cases the line cells were significantly bigger compared to the line cell observed in this work. So their observations are also true for smaller scales. The layer of the investigated line cell has switched over the whole thickness. A sharp vertical boundary exists between the switched and the remaining crystalline part of the AIST layer beneath the electrode gap. This work demonstrates that bright field TEM combined with tilting of specimens of phase change material devices can detect switched regions of phase change material down to a few nm. It can also divide the amorphous from the crystalline phase based on the Bragg contrast. This is a tool very easy to use in almost every TEM for the analysis of electronic phase change memory devices to help understand switching properties.

8.3 Nano area electron diffraction of Sb_2Te_3 platelet intermediates

In the publication of T. Saltzmann and co-workers and in the thesis of T. Saltzmann, the formation mechanism of Sb_2Te_3 hexagonal platelets out of a solvothermal synthesis were revealed (Saltzmann, 2014; Saltzmann et al., 2015). T. Saltzmann identified four intermediates by SEM. These intermediates lead to the formation of Sb_2Te_3 hexagonal platelets. **Figure 95** shows the formation path of the hexagonal platelets. The spherical intermediate 1 could be produced without side products. T. Saltzmann proved by X-Ray diffraction (XRD) that this intermediate is still amorphous. By XRD the crystalline state of the final hexagonal platelets was also shown. The intermediates 2, 3 and 4 are the main but not the exclusive products of the reaction, quenched to room temperature, at the chosen reaction time. So the spatial resolution of XRD was not suitable to analyse their phases.

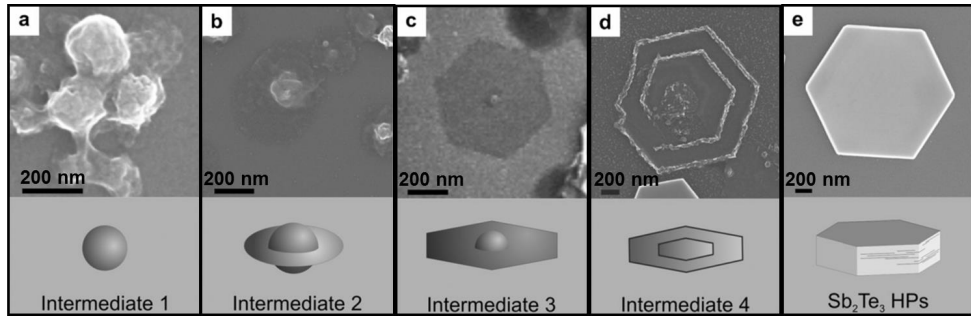


Figure 95: Shown are SEM images and schemes of the different intermediates ((a)-(b)) in the solvothermal synthesis on the formation path to crystalline hexagonal Sb_2Te_3 platelets (e). Image reprinted and amended with acknowledgment from the publication of T. Saltzmann (Saltzmann et al., 2015).

Scanning of the intermediates by NAED gives information about the phase composition with a spatial resolution of the adjusted electron beam probe size. In our case, a probe size of around 2 nm was used. It was possible to show that in the intermediate 2 only parts of the core are crystalline. The surrounding around the core consist of amorphous material. From the vague hexagonal shape of the layer, which surrounds the core of intermediate 3, the assumption can be made, that the surrounding layer has to be crystalline. This assumption takes into account that the growth directions of crystal lattices influence the shape of the resulting crystals. NAED proves that intermediate 3 is only crystalline in the core and that the vague hexagon-like shaped surrounding layer of intermediate 3 is completely amorphous. The reason for the shape influence of the core surrounding layer is still not understood. Intermediate 4 is a thin hexagonal crystalline platelet of Sb_2Te_3 . The layer is surrounded by a rim of thicker material. The single crystalline nature of the thin Sb_2Te_3 platelet was proven by NAED. The intermediate 4 of Sb_2Te_3 is viewed along the [111] direction. In **Figure 78** additional amounts of material can be seen on top of the intermediate 4 probably leading to growth of additional crystalline Sb_2Te_3 layers or rest products of the stopped reaction. At the end of a completed solvothermal synthesis this leads to the production of the single crystalline Sb_2Te_3 hexagonal platelets described in the beginning. T. Saltzmann demonstrated in his thesis that the produced hexagonal platelets can be switched electrically. A two micromanipulator setup in a SEM was used for contacting the hexagonal platelets from two different orientations. They show typical phase change switching behavior. He could demonstrate that the orientation of the hexagonal platelets to the induced current influences the measured switching curves (Saltzmann, 2014). In this work, it

was demonstrated that NAED is a tool to differentiate between the amorphous and the crystalline phase of phase change materials with the spatial resolution of the probe size (2 nm). The phases of the components of the intermediates 2, 3 and 4 were investigated and the steps of an interesting reaction path of hexagonal Sb_2Te_3 platelets were revealed.

8.4 TEM/STEM investigations of a Ge₁Sb₂Te₄ layer grown by MOVPE

The TEM and HRSTEM images in this work demonstrate that the GST 124 layer deposited by MOVPE is completely single crystalline with the exception of an observed lamellar defect. The lamellar defect is clearly visible in TEM (**Figure 83**). The lamellar defect is not visible in HAADF HRSTEM imaging viewed in [210] direction. This is a strong indication that the lamellar defect has to be a twin because the atomic arrangement of the structure viewed in [210] direction and its 60° around the c axis tilted twin structure counterpart looks similar viewed in this direction. Also electron backscatter diffraction analysis results performed by A. Schwedt support the twin assumption (Hardtdegen et al., 2016). The overall quality of the MOVPE deposited layer is very good over the length of the lamella except some minor gaps at the surface (**Figure 84**). The MOVPE method clearly deposited an epitaxial layer of GST 124.

The TEM and STEM analysis proof that the GST 124 layers deposited by MOVPE are in the hexagonal stable phase of GST 124. The investigated structure is in very good agreement with the stable phase of GST 124 investigated by Matsunaga and co-workers by X-ray powder diffraction (Matsunaga & Yamada, 2004). The space group is $R\bar{3}m$. The stacking sequence of one seven atom layer band framed by van der Waals gaps is supported by Matsunagas proposed structure gap-Te-Ge₂₅Sb₇₅-Te-Ge₅Sb₅-Te-Ge₂₅Sb₇₅-Te-gap. The Te atom rows are the brightest features in the HAADF images caused by Z-contrast (**Figure 87**). That the Te atom rows show the strongest Z-contrast in HAADF HRSTEM images can be seen in other HAADF HRSTEM pictures of different GST compositions or GeTe-Sb₂Te₃ super lattice structures in literature (Thelanger, 2015; Tominaga et al., 2015). The occupation of the anion sites by Te atoms is an agreed fact in literature (Matsunaga & Yamada, 2004; Da Silva et al., 2008). The exact determination of the distribution of Ge, Sb or vacancies in the cation layers proved to be challenging in the past (Kuypers et al., 1989). This caused an ongoing discussion in literature. One side believes in ordered layers of one atom species for the Ge/Sb layers. This means there are pure Ge or Sb layers, with additional distributed vacancies (Da Silva et al., 2008). The other side believes in mixed Ge, Sb and vacancies cation layers (Matsunaga & Yamada, 2004). We simulated the structure proposed by Matsunaga and co-workers by Dr. Probe. Dr. Probe simulates the electron beam propagation

through a crystal by a multi-slice approach (Barthel, 2012). The structure from Matsunaga promotes mixed cation layers and fits very well to our results (**Figure 87**). For comparison in **Figure 96** both structures discussed in literature are shown viewed in [210] direction. The rendered images are built by the 3D visualization software VESTA (Momma & Izumi, 2011).

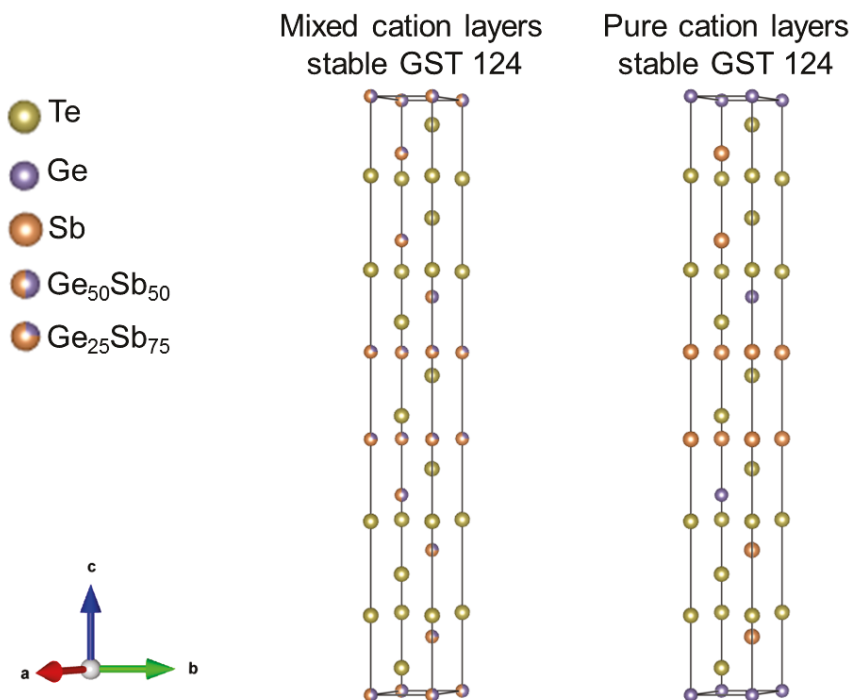


Figure 96: Shown are the both most commonly assumed stable hexagonal GST 124 structures (Matsunaga & Yamada, 2004; Da Silva et al., 2008) visualized by the 3D software VESTA (Momma & Izumi, 2011).

H. Du also analyzed the electron count distribution of the HAADF HRSTEM signal presented in this work and the publication of H. Hardtdegen and co-workers. **Figure 97** shows the intensity profile of the electron counts in relation of electron probe position over the GST 124 structure. The intensity profile also supports the structure supported by Matsunaga and co-workers. A comparison of X-RAY diffraction data and simulated X-RAY diffraction patterns for the ordered and mixed case presented in the publication of H. Hardtdegen and co-workers also supports the mixed structure hypothesis (Hardtdegen et al., 2016).

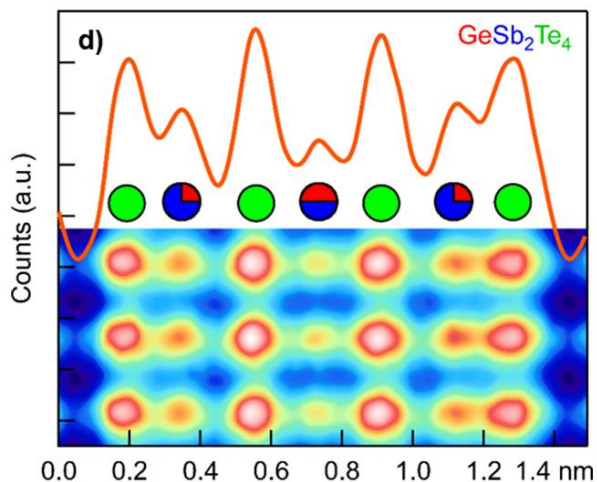


Figure 97: Shown is the intensity profile of the HAADF signal in relation to scanning position of the electron probe. The highest HAADF signal is produced by the Te atoms. A slightly decrease in HAADF signal at the atom row in the middle suggests higher amount of Ge producing less scattering. Image reprinted with permission from the publication of H. Hardtdegen and co-workers (Hardtdegen et al., 2016).

Further proof of the structure could be given by a detailed EDX or EELS investigation in STEM at atomic resolution. This was for example done for GST 225 in the metastable rocksalt configuration (Zhang et al., 2016). First attempts in this direction have been initiated, but the challenges of specimen drift, carbon contamination and the stability of the specimen under influence of the electron beam have to be overcome for the stable phase of GST 124.

The lattice constants a and c were derived from the Fourier transform of the HAADF HRSTEM picture (**Figure 86**). The measured constants are $a = 0.42$ nm and $c = 4.04$ nm with an error of 0.1 nm. By X-RAY diffraction, lattice constants of $a = 0.43$ nm and $c = 4.10$ nm were derived from the same sample as the investigated TEM lamella was prepared from. These values are in good agreement to each other and to the values reported by Matsunaga for X-RAY powder diffraction measurements of GST 124 in the stable phase (Matsunaga & Yamada, 2004). By HAADF HRSTEM the mismatch region is imaged where the GST 124 needs to fit its lattice parameters to the lattice parameters of the Si viewed in [210] direction. The adaption zone is 2.04 nm thick and followed by perfectly grown GST 124 in the stable phase (**Figure 88**). This indicates that the GST 124 is not grown by van der Waals epitaxy on the Si substrate. Probably dangling bonds of the Si substrate are therefore not terminated. The adaption zone is than a result of a mixture of intermediate layers

gradually adapting to the lattice mismatch between Si and GST 124 and layers with built-in point defects compensating dangling bonds that found no bonding, because of the lattice mismatch (Koma, 1992).

Direct epitaxial deposition of GST layers is presented in literature by molecular beam epitaxy (MBE) (Perumal, 2013) and pulsed laser deposition (PLD) (Thelanger, 2015). The reported MBE deposition methods mostly focus on the material GST 225. They claim to deposit GST in the rocksalt structure. This would mean they deposited the metastable phase of GST. In the thesis of R. Thelanger epitaxial layers of GST by PLD were produced (Thelanger, 2015). His main focus was also to produce GST 225 layers. He noted that on various occasions the GST decomposes to GST 124. Deposited pure high quality stable phase GST 124 layers are not demonstrated in his work. To our knowledge the direct epitaxially deposited GST 124 layers of the stable hexagonal phase produced at the Peter Grünberg Institut 9 which are investigated in this thesis are the first of its kind. The SEM images (**Figure 80**) show that the MOVPE process has to be optimized to produce completely closed homogenous layers over larger areas. Nonetheless TEM/STEM proved the direct epitaxially deposition of high quality GST 124 layers in the stable phase by MOVPE (Schuck et al., 2015; Hardtdegen et al., 2016; Riess, 2017).

9 Outlook

In this work TEM and its related techniques were used to investigate various aspects of phase change materials. TEM proves to be an indispensable technique for material characterization and there are many possible ways to build on or expand the results from this work in the future.

The most obvious way would be to increase the amount of different phase change materials analyzed. This would allow a comparison of the results for different materials and compositions. An identification of links between properties for all phase change materials would then be possible. These links could then be related to the treasure map of Lencer and co-workers (Lencer et al., 2008). This would be especially interesting for our results of the crystallization kinetics that are linked to the MRO.

By the variation of electron beam probe sizes used for FEM, the cluster sizes of the MRO can be narrowed down (Hwang & Voyles, 2011). A significant amount of preparation and microscope time and especially high amounts of specimens would be required. This can be very problematic for the melt quenched amorphous phase. A comparison to other glasses, which are not phase change materials and their relation of crystallization kinetics to the MRO could reveal unknown properties of all glasses in general. Further attempts to understand the MRO by a comparison between measured FEM data and FEM data produced by structural simulations would also be in demand. They would provide information about the real atomic arrangements of the amorphous phase states.

More detailed TEM investigations of electrically switched phase change devices could reveal correlations of switching parameters and structural changes. Especially for electronic phase change devices, in situ TEM imaging would be a good method to reveal the switching dynamics. For this, the challenges of time scales, influence of the electron beam and the development of electron transparent switchable specimens have to be overcome. J.Oosthoek tried to switch phase change line cells in situ in the TEM already, but his cells were very large (line width 250 nm) and he encountered several challenges with contacting the very thin electron transparent membranes (Oosthoek, 2014b). Comparisons between FEM data of switched amorphous material from electronic devices and the data of the FEM data of this work would reveal further insides of the behaviour of the MRO. Unfortunately

electronic devices are very small, so several devices of the same type would be needed for one FEM measurement.

Further insights into the structure of IPCMs and layered phase change materials like the investigated GST 124 in the stable phase could be gathered by chemical analysis at atomic resolution. This is very challenging, because of sample drift, contamination and stability under the influence of the electron beam. Successful attempts were already performed for metastable rocksalt GST 225 (Zhang et al., 2016). An electrically switched IPCM or layered phase change material sample compared to a reference, that is not switched, could reveal the detailed switching mechanism on the atomic level. This would be a very valuable insight, because of the promising enhanced switching behaviours of IPCM.

10 List of abbreviations

$2\cdot\theta_B$ *Bragg angle*

a *lattice constant, diameter of the (000) diffraction spot*

ADF *annular dark field*

AFM *atomic force microscopy*

Ag *Silver*

AIST *$Ag_4In_3Sb_{67}Te_{26}$*

as deposited *state after deposition*

b *distance of the (000) spot to the next diffraction spot of the chosen (hkl) lattice plane*

Blue-ray discs *brand name of optical media carrier*

c *lattice constant*

C *carbon*

C2 *condenser lens 2*

C3 *condenser lens 3*

CCD *charged-coupled device*

CNR *National Research Council of Italy*

d^*_{lit} *reciprocal lattice plane spacing from literature*

d^*_{meas} *reciprocal lattice plane spacing measured*

DFG *Deutsche Forschungsgemeinschaft*

d_{lit} *lattice plane spacing from literature*

d_{meas} *lattice plane spacing measured*

DRAM *dynamic random access memory*

DSC *differential scanning calorimeter*

dual beam FIB/SEM *combination of SEM and FIB in one system*

E_a *activation energy*

EDX *Energy-dispersive X-ray spectroscopy*

EELS *electron energy loss spectroscopy*

ER-C *Ernst Ruska Centre*

ETD *Everhart Thornley detector*

$f(\theta)$ *volume fraction*

FEM *FEM in STEM, fluctuation electron microscopy*

FIB *focused ion beam*

flash *non-volatile computer memory*

F_{real} *calibration factor real space*

F_{rec} *calibration factor reciprocal space*

FWHM *full width half maximum*

G *Gibbs free energy*

G^* *maximum of the Gibbs free energy*

G^*_{het} *maximum of the Gibbs free energy of heterogenous nucleation*

G^*_{hom} *maximum of the Gibbs free energy of homogeneous nucleation*

- Ge *germanium*
GFE *Central Facility for Electron Microscopy*
GST *alloy of Ge, Sb and Te*
GST 124 $Ge_1Sb_2Te_4$
GST 225 $Ge_2Sb_2Te_5$
H *hydrogen*
HRSTEM *high resolution scanning transmission electron microscopy*
HRTEM *high resolution transmission electron microscopy*
i *index number of map*
I(k,Q) *measured intensity*
 $I_{z,i,j}(k)$ *intensities of a single NAED pattern*
 $I_{int,z,i,j}$ *integrated intensity of a single NAED pattern*
 $I_{avg,z,i}$ *averaged intensity of single map*
 $I_{avg,z}$ *average intensity of specimen*
 $I_{vac,z}$ *beam intensity in vacuum*
 $I_{vac,avg}$ *average beam intensity in vacuum*
 i_{crit} *number of atoms in the critical nucleus*
 I_{equ} *nucleation rate at the equilibrium*
In *indium*
IPCM *interfacial phase change memory*
 I_{ss} *steady state nucleation rate*
 $I_{ss,het}$ *steady state nucleation rate for diffusion limited heterogeneous nucleation*
j *index number of NAED pattern*
k *scattering vector, arrival rate*
 k_B *Boltzmann constant*
KOH *potassium hydroxide*
M *number of maps*
melt quenched *state after quenching melt in the amorphous phase*
MOVPE *metal organic vapor phase epitaxy*
MRO *medium range order*
N *nitrogen, number of NAED patterns in map*
N(r) *amount of nuclei forming following the Boltzmann distribution*
 $N(r_{crit})$ *the number of nuclei with the critical radius*
 N_0 *the total amount of atoms in the liquid*
NAED *nano area electron diffraction*
 $N_{ss(r)}$ *distribution of nuclei in steady state*
 $N_{ss(rcrit)}$ *number of nuclei with the radius r_{crit} in the steady state model*
PGI-9 *Peter Grünberg Institute 9*
PVP *polyvinylpyrrolidone*
Q *reciprocal space resolution*
r *radius*
 r_{crit} *critical radius*

reset pulse *short heat pulse of high intensity*
RWTH Aachen University *Rheinisch-Westfälische Technische Hochschule Aachen*
Sb *antimony*
 s_{crit} number of surface atoms of the critical nucleus
SEM *scanning electron microscope*
set pulse *longer heat pulse of lower intensity*
SFB 917 *Sonderforschungsbereich 917 Nanoswitches*
SRO *short range order*
SSD *solid state disc*
STEM *scanning transmission electron microscopy/microscope*
T *temperature*
TDS *thermal diffuse scattering*
Te *tellurium*
TEM *transmission electron microscopy/microscope*
 T_g *glass transition temperature*
TLD *through the lens detector*
 T_m *melting temperature*
u *growth velocity*
USB *universal serial bus*
 u_{sound} *velocity of sound*
V *normalized variance, volume*
 $\hat{V}_{z,i}(k)$ *variance of map normalized to average map intensity*
 $\hat{V}_{z,i}(k)$ *variance of map normalized to average specimen intensity*
 $\tilde{V}_z(k)$ *average variance of a specimen normalized to average specimen intensity*
 $\hat{V}_z(k)$ *average variance of specimen normalized to the intensity of reference specimen*
 $V_z(k)$ *final normalized variance of a specimen*
XRD *X-Ray diffraction*
z *index number of specimen*
Z *Zeldovich factor*
 α *semi convergence angle*
 ΔG *the total change of the Gibbs free energy*
 $\Delta G_{\text{ac,atom}}$ *energy difference between the amorphous parent phase and crystalline phase per atom*
 ΔG_V *the change of the Gibbs free energy per unit volume*
 ΔH_V *the change in enthalpy per unit volume*
 ΔS_V *the change in entropy per unit volume*
 ϵ *amount of atoms of the amorphous phase in contact with the substrate*
 η *viscosity*
 θ *contact angle*
 λ *wavelength of the electrons, average interatomic distance*
 σ *resolution*

List of abbreviations

ζ_s *amount of possible sites an atom can attach to the nucleus*

γ_{ac} *interfacial energy of the amorphous to crystalline interface*

γ_{as} *interfacial energy of the amorphous to substrate interface*

γ_{cs} *interfacial energy of the crystal to substrate interface*

11 Bibliography

1. Abbe, E. 1873.
2. Agaev, K. A. & Semiletov, S. A. 1965 *Sov Phys Crystallogr*, **10**, 86.
3. Amazon 2016, www.amazon.com
4. Anderson, R. M. & Walck, S. D. 1997, Pittsburgh, Pa.: Materials Research Society.
5. Anderson, T. L. & Krause, H. B. 1974 *Acta Crystallographica Section B*, **30**, 1307.
6. Apple 2016, www.apple.com/de/itunes/
7. Barthel, J. 2012, 15th Euro. Microsc. Cong. Manchester.
8. Barthel, J., Houben, L. & Tillmann, K. 2015 *Journal of large-scale research facilities JLSRF; Vol 1 (2015); A34*.
9. Bastard, A., Bastien, J. C., Hyot, B., Lhostis, S., Momprou, F., Bonafos, C., Servanton, G., Borowiak, C., Lorut, F., Bicaïs-Lepinay, N., Toffoli, A., Sandhya, C., Fantini, A., Perniola, L., Gourvest, E., Maitrejean, S., Roule, A., Sousa, V., Bensahel, D. & André, B. 2011 *Appl Phys Lett*, **99**, 243103.
10. Becker, R. & Döring, W. 1935 *Annalen der Physik* **24**, 719.
11. Benke, J. 2017, Doctoral thesis (unpublished), RWTH Aachen University
12. Bernal, J. D. 1964 *Proceedings of the Royal Society of London. Series A, Mathematical and Physical Sciences*, **280**, 299.
13. Bez, R., Camerlenghi, E., Modelli, A. & Visconti, A. 2003 *Proceedings of the IEEE*, **91**, 489.
14. Bogle, S. N., Nittala, L. N., Twesten, R. D., Voyles, P. M. & Abelson, J. R. 2010 *Ultramicroscopy*, **110**, 1273.
15. Bornhöfft, M. 2012, Master thesis (unpublished), RWTH Aachen University
16. Castro, D. T., Goux, L., Hurkx, G. A. M., Attenborough, K., Delhougne, R., Lisoni, J., Jedema, F. J., t Zandt, M. A. A., Wolters, R. A. M., Gravesteijn, D. J., Verheijen, M., Kaiser, M. & Weemaes, R. G. R. 2007, Electron Devices Meeting, 2007. IEDM 2007. IEEE International.
17. Cavagna, A. 2009 *Physics Reports*, **476**, 51.
18. Christian, J. W. 1965, Oxford: Pergamon Pr.
19. Coombs, J. H., Jongenelis, A. P. J. M., van Es-Spiekman, W. & Jacobs, B. A. J. 1995 *J Appl Phys*, **78**, 4906.
20. Cox, D. C. 2015: Morgan & Claypool Publishers.
21. Da Silva, J. L. F., Walsh, A. & Lee, H. 2008 *Phys Rev B*, **78**.
22. Day, C. 2009 *Physics Today*, **62**, 17.

23. De Graef, M. 2003, Cambridge: Cambridge University Press.
24. Egami, T. & Billinge, S. J. L. 2012, [S.I.]: Pergamon.
25. Elliott, S. R. 1990, Harlow: Longman.
26. Feinleib, J., deNeufville, J., Moss, S. C. & Ovshinsky, S. R. 1971 *Appl Phys Lett*, **18**, 254.
27. Friedrich, I. 2000: Germany, Europe Forschungszentrum Jülich, Zentralbibl, 2000.
28. Fulcher, G. S. 1925 *J Am Ceram Soc*, **8**, 789.
29. Giannuzzi, L. A. 2005, Berlin: Springer.
30. Gibbs, J. W. 1906: Longmans, Green and co.
31. Goldstein, J. 2007, New York: Springer.
32. Gottstein, G. 2007: Springer.
33. Gross, D. 2012 CNN.
34. Haider, M., Uhlemann, S., Schwan, E., Rose, H., Kabius, B. & Urban, K. 1998 *Nature*, **392**, 768.
35. Hardtdegen, H., Rieß, S., Schuck, M., Keller, K., Jost, P., Du, H., Bornhöfft, M., Schwedt, A., Mussler, G., v.d. Ahe, M., Mayer, J., Roth, G., Grützmacher, D. & Mikulics, M. 2016 *J Alloy Compd*, **679**, 285.
36. Hawkes, P. W. 2009 *Philosophical Transactions of the Royal Society of London A: Mathematical, Physical and Engineering Sciences*, **367**, 3637.
37. Heggen, M., Luysberg, M. & Tillmann, K. 2016 *Journal of large-scale research facilities JLSRF*, **2**.
38. Herlach, D. M. 2007 *Thermec 2006, Pts 1-5*, **539-543**, 1977.
39. Hwang, J. & Voyles, P. M. 2011 *Microsc Microanal*, **17**, 67.
40. Ielmini, D., Sharma, D., Lavizzari, S. & Lacaita, A. L. 2009 *Electron Devices, IEEE Transactions on*, **56**, 1070.
41. Jeol 2016, <http://www.jeol.de/electronoptics/produktuebersicht/elektronen-ionenoptische-systeme/transmissionselektronenmikroskope/200-kv-tem-feg-tem/jem-2100f.php>
42. Kalb, J. 2006: Germany, Europe Publikationsserver der RWTH Aachen University, 2006.
43. Kalb, J. A., Wuttig, M. & Spaepen, F. 2007 *J Mater Res*, **22**, 748.
44. Kaldenbach, A. 2012,
45. Karpov, I. V. & Kostylev, S. A. 2006 *Electron Device Letters, IEEE*, **27**, 808.
46. Kau, D., Tang, S., Karpov, I. V., Dodge, R., Klehn, B., Kalb, J. A., Strand, J., Diaz, A., Leung, N., Wu, J., Lee, S., Langtry, T., Chang, K., Papagianni, C., Lee, j., Hirst, J., Erra, S., Flores, E., Righos, N., Castro,

- H. & Spadini, G. 2009, Electron Devices Meeting (IEDM), 2009 IEEE International.
47. Kelton, k. 1991 *Solid State Physics*, **45**, 75.
48. Kivelson, D., Kivelson, S. A., Zhao, X., Nussinov, Z. & Tarjus, G. 1995 *Physica A: Statistical Mechanics and its Applications*, **219**, 27.
49. Klein, M. 2009, http://publications.rwth-aachen.de/record/51433/files/Klein_Michael.pdf
50. Knoll, M. & Ruska, E. 1932 *ZEITSCHRIFT FUR PHYSIK; SEP, 1932, 79 9-10, p699-p699, 1p.*, **79**, Start Page: 699.
51. Kolosov, V. Y. 2008 *EMC 2008 14th European Microscopy Congress 1–5 September 2008, Aachen, Germany*, Vol. 2 (eds. Richter, S. & Schwedt, A.): Springer Berlin Heidelberg, pp. 657-658.
52. Koma, A. 1992 *Thin Solid Films*, **216**, 72.
53. Kooi, B. J. & De Hosson, J. T. M. 2002 *J Appl Phys*, **92**, 3584.
54. Kovacs, A., Schierholz, R. & Tillmann, K. 2016 *Journal of large-scale research facilities*, **2**.
55. Kuypers, S., Frangis, N., Vanlanduyt, J. & Amelinckx, S. 1989 *Institute of Physics Conference Series*, 45.
56. Kuypers, S., Van Tendeloo, G., Van Landuyt & Amelinckx, S. 1988 *JOURNAL OF SOLID STATE CHEMISTRY*, **76**, 102.
57. Lankhorst, M. H. R., Ketelaars, B. W. S. M. M. & Wolters, R. A. M. 2005 *Nat Mater*, **4**, 347.
58. Lavizzari, S., Ielmini, D., Sharma, D. & Lacaita, A. L. 2009 *Electron Devices, IEEE Transactions on*, **56**, 1078.
59. Lee, B.-S., Burr, G. W., Shelby, R. M., Raoux, S., Rettner, C. T., Bogle, S. N., Darmawikarta, K., Bishop, S. G. & Abelson, J. R. 2009a *Science*, **326**, 980.
60. Lee, B.-S., Shelby, R. M., Raoux, S., Retter, C. T., Burr, G. W., Bogle, S. N., Darmawikarta, K., Bishop, S. G. & Abelson, J. R. 2014 *J Appl Phys*, **115**, 063506.
61. Lee, B., Burr, G. W., Shelby, R. M., Raoux, S., Rettner, C. T., Bogle, S. N., Darmawikarta, K., Bishop, S. G. & Abelson, J. R. 2009b *Science*, **326**, 980.
62. Lencer, D., Salinga, M., Grabowski, B., Hickel, T., Neugebauer, J. & Wuttig, M. 2008 *Nat Mater*, **7**, 972.
63. Lowe, S. D. 2015 *Flashstorage.com*.
64. Matsunaga, T., Umetani, Y. & Yamada, N. 2001 *Phys Rev B*, **64**.
65. Matsunaga, T. & Yamada, N. 2004 *Phys Rev B*, **69**.
66. Matsunaga, T., Yamada, N. & Kubota, Y. 2004 *Acta Crystallographica B* **60**, 685.

67. Mauro, J. C., Yue, Y., Ellison, A. J., Gupta, P. K. & Allan, D. C. 2009 *Proceedings of the National Academy of Sciences*, **106**, 19780.
68. Meinders, E. R., Mijiritskii, A. V., Pieterse, L. & Wuttig, M. 2006, Dordrecht: Springer.
69. Meister, S., Peng, H., McIlwrath, K., Jarausch, K., Zhang, X. F. & Cui, Y. 2006 *Nano Lett*, **6**, 1514.
70. Mijiritskii, A. V., Hellmig, J., Borg, H. J., Vromans, P. H., Musialkova, K. & Van Haaren, J. A. 2003.
71. Mio, A. M., Carria, E., D'Arrigo, G., Gibilisco, S., Miritello, M., Grimaldi, M. G. & Rimini, E. 2011 *J Non-Cryst Solids*, **357**, 2197.
72. Momma, K. & Izumi, F. 2011 *Journal of Applied Crystallography*, **44**, 1272.
73. Netflix 2016, www.netflix.com
74. Ohyanagi, T., Kitamura, M., Araidai, M., Kato, S., Takaura, N. & Shiraishi, K. 2014 *Appl Phys Lett*, **104**, 252106.
75. Oosthoek, J. L. M. 2014a: Netherlands, Europe s.n, 2014.
76. Oosthoek, J. L. M. 2014b,
77. Orava, J., Greer, A. L., Gholipour, B., Hewak, D. W. & Smith, C. E. 2012 *Nat Mater*, **11**, 279.
78. Orloff, J. 1997, Boca Raton, Fla.: CRC Pr.
79. Ovshinsky, S. R. 1968 *Phys Rev Lett*, **21**, 1450.
80. Pan, Y., Inam, F., Zhang, M. & Drabold, D. A. 2008 *Phys Rev Lett*, **100**, 206403.
81. Pandian, R., Kooi, B. J., De Hosson, J. T. M. & Pauza, A. 2007 *J Appl Phys*, **101**, 053529.
82. Pennycook, S. J. & Nellist, P. D. 2011, New York, NY: Springer Science+Business Media, LLC.
83. Perumal, K. 2013, <http://edoc.hu-berlin.de/dissertationen/perumal-karthick-2013-07-30/PDF/perumal.pdf>
84. Porter, D. A. & Easterling, K. E. 1992: Springer-Science+Business Media, B.Y.
85. Pries, J. 2013, Bachelor thesis (unpublished), RWTH Aachen University
86. Pries, J. 2015, Master thesis (unpublished), RWTH Aachen University
87. Raoux, S. 2009, New York, NY: Springer.
88. Raoux, S., Welnic, W. & Ielmini, D. 2010 *Chemical Reviews*, **110**, 240.
89. Reimer, L. 1998, Berlin: Springer.
90. Reimer, L. & Kohl, H. 2008, New York, NY: Springer.

91. Riess, S. 2017, Doctoral thesis (unpublished), Forschungszentrum Jülich
92. Salinga, M. 2008: Germany, Europe Publikationsserver der RWTH Aachen University, 2008.
93. Salinga, M., Carria, E., Kaldenbach, A., Bornhöfft, M., Benke, J., Mayer, J. & Wuttig, M. 2013 *Nat Commun*, **4**.
94. Saltzmann, T. 2014, <http://publications.rwth-aachen.de/record/481279>
95. Saltzmann, T., Bornhofft, M., Mayer, J. & Simon, U. 2015 *Angewandte Chemie*, **54**, 6632.
96. Samsung Electronics Co. Ltd. 2006, <http://www.samsung.com/semiconductor/insights/news/4219>
97. Santala, M. K., Reed, B. W., Raoux, S., Topuria, T., LaGrange, T. & Campbell, G. H. 2012 *physica status solidi (b)*, **249**, 1907.
98. Scheifers, J. P. 2011, Bachelor thesis (unpublished), RWTH Aachen University
99. Scherzer, O. 1936 *Zeitschrift für Physik*, **101**, 593.
100. Schmidt, B. & Wetzig, K. 2013, Vienna: Springer.
101. Schuck, M., Riess, S., Schreiber, M., Mussler, G., Grutzmacher, D. & Hardtdegen, H. 2015 *J Cryst Growth*, **420**, 37.
102. Shelimova, L. E., Karpinskii, O. G., Kretova, M. A., Kosyakov, V. I., Shetakov, V. A., Zemskov, V. S. & Kuznetsov, F. A. 1998 *Neorganicheskie Materialy*, **36**, 928.
103. Shintani, T. & Saiki, T. 2013 *Applied Physics Express*, **6**, 111401.
104. Shportko, K., Kremers, S., Woda, M., Lencer, D., Robertson, J. & Wuttig, M. 2008 *Nat Mater*, **7**, 653.
105. Simpson, R. E., Fons, P., Kolobov, A. V., Fukaya, T., Krbal, M., Yagi, T. & Tominaga, J. 2011 *Nat Nanotechnol*, **6**, 501.
106. Smith, A. W. 1974 *Appl Optics*, **13**, 795.
107. Sokolov, A. P., Shebanin, A. P., Golikova, O. A. & Mezdrogina, M. M. 1991 *Journal of Physics: Condensed Matter*, **3**, 9887.
108. Sosso, G. C., Behler, J. & Bernasconi, M. 2013a *physica status solidi (b)*, **250**, 1453.
109. Sosso, G. C., Miceli, G., Caravati, S., Giberti, F., Behler, J. & Bernasconi, M. 2013b *The Journal of Physical Chemistry Letters*, **4**, 4241.
110. Sosso, G. C., Salvalaglio, M., Behler, J., Bernasconi, M. & Parrinello, M. 2015 *The Journal of Physical Chemistry C*, **119**, 6428.
111. Stadelmann, P. 2016, <http://www.jems-saas.ch/>

112. Stanisavljevic, M., Athmanathan, A., Papandreou, N., Pozidis, H. & Eleftheriou, E. 2015, Reliability Physics Symposium (IRPS), 2015 IEEE International.
113. Tamman, G. & Hesse, W. 1926 *Z Anorg Allg Chem*, **156**, 245.
114. Thelanger, R. 2015, ISBN: 978-94-91909-80-5 (printed version)
115. Thompson, A. G. 1997 *Materials Letters*, **30**, 255.
116. Tominaga, j., Fons, P., Kolobov, A., Shima, T., Chong, T., Zhao, R., Lee, H. K. & Shi, L. 2008 *Jpn J Appl Phys*, **47**, 5763.
117. Tominaga, J., Kolobov, A. V., Fons, P. J., Wang, X. M., Saito, Y., Nakano, T., Hase, M., Murakami, S., Herfort, J. & Takagaki, Y. 2015 *Sci Technol Adv Mat*, **16**.
118. Treacy, M. M. J. & Gibson, J. M. 1996 *Acta Crystallographica Section A*, **52**, 212.
119. Treacy, M. M. J., Gibson, J. M., Fan, L., Paterson, D. J. & McNulty, I. 2005 *Rep Prog Phys*, **68**, 2899.
120. Turnbull, D. & Fisher, J. C. 1949 *The Journal of Chemical Physics*, **17**, 71.
121. Vogel, H. 1921 *Physikalische Zeitschrift*, **22**, 645.
122. Volmer, M. 1929 *Zeitschrift für Elektrochemie und angewandte physikalische Chemie*, **35**, 555.
123. Volmer, M. & Weber, A. 1926 *Zeitschrift für Physikalische Chemie*, **119**, 277.
124. Voyles, P. & Burton, M. 2014, <https://github.com/paul-voyles/Fluctuation-Microscopy>
125. Voyles, P. M. & Abelson, J. R. 2003 *Sol Energ Mat Sol C*, **78**, 85.
126. Voyles, P. M. & Muller, D. A. 2002 *Ultramicroscopy*, **93**, 147.
127. Wasa, K. 2012 *Handbook of Sputtering Technology (Second Edition)*Oxford: William Andrew Publishing, pp. xi-xii.
128. Weidenhof, V., Friedrich, I., Ziegler, S. & Wuttig, M. 2001 *J Appl Phys*, **89**, 3168.
129. Williams, D. B. & Carter, C. B. 2009, New York, NY: Springer.
130. Wimmer, M. 2015, <http://publications.rwth-aachen.de/record/464593/files/464593.pdf>
131. Wimmer, M., Kaes, M., Dellen, C. & Salinga, M. 2014 *Frontiers in Physics*, **2**.
132. Wuttig, M. & Yamada, N. 2007 *Nat Mater*, **6**, 824.
133. Yamada, N. 1996 *Mrs Bull*, **21**, 48.
134. Yamada, N., Ohno, E., Akahira, N., Nishiuchi, K., Nagata, K. & Takao, M. 1987 *Jpn J Appl Phys*, **26**, 61.

135. Yamada, N., Ohno, E., Nishiuchi, K., Akahira, N. & Takao, M. 1991 *J Appl Phys*, **69**, 2849.
136. Yi, F., Tiemeijer, P. & Voyles, P. M. 2010 *J Electron Microsc*, **59 Suppl 1**, S15.
137. Young, T. 1805 *Philosophical Transactions of the Royal Society of London*, **95**, 65.
138. Zach, J. & Haider, M. 1995 *Nuclear Instruments and Methods in Physics Research Section A: Accelerators, Spectrometers, Detectors and Associated Equipment*, **363**, 316.
139. Zachariasen, W. H. 1932 *Journal of the American Chemical Society*, **54**, 3841.
140. Zallen, R. 1983, New York: Wiley.
141. Zhang, B., Zhang, W., Shen, Z., Chen, Y., Li, J., Zhang, S., Zhang, Z., Wuttig, M., Mazzarello, R., Ma, E. & Han, X. 2016 *Appl Phys Lett*, **108**, 191902.
142. Zhong, K., Wang, T., Zhu, X., Long, L., Liu, D., Liu, W., Shao, Z. & Sha, E. H. M. 2014, Embedded Software (EMSOFT), 2014 International Conference on.
143. Zhou, G. 2001 *Materials Science and Engineering: A*, **304–306**, 73.
144. Ziegler, S. 2005, http://publications.rwth-aachen.de/record/59673/files/Ziegler_Stefan.pdf

Band / Volume 34

Structure, electronic properties, and interactions of defects in epitaxial GaN layers

P. H. Weidlich (2014), 139 pp

ISBN: 978-3-89336-951-5

Band / Volume 35

Defect Engineering of SrTiO₃ thin films for resistive switching applications

S. Wicklein (2014), xi, 144 pp

ISBN: 978-3-89336-963-8

Band / Volume 36

Integration and Characterization of Atomic Layer Deposited TiO₂ Thin Films for Resistive Switching Applications

M. Reiners (2014), xiv, 166 pp

ISBN: 978-3-89336-970-6

Band / Volume 37

Resistive switching in ZrO₂ based metal-oxide-metal structures

I. Kärkkäinen (2014), xviii, 125 pp

ISBN: 978-3-89336-971-3

Band / Volume 38

Resistive switching phenomena of extended defects in Nb-doped SrTiO₃ under influence of external gradients

C. Rodenbücher (2014), xiii, 200 pp

ISBN: 978-3-89336-980-5

Band / Volume 39

Micro-spectroscopic investigation of valence change processes in resistive switching SrTiO₃ thin films

A. Köhl (2014), viii, 166 pp

ISBN: 978-3-89336-988-1

Band / Volume 40

Strained Silicon and Silicon-Germanium Nanowire Tunnel FETs and Inverters

S. Richter (2014), iii, 117 pp

ISBN: 978-3-95806-002-9

Band / Volume 41

Integration of Redox-Based Resistive Switching Memory Devices

F. Lentz (2014), i, 166 pp

ISBN: 978-3-95806-019-7

Band / Volume 42

Ladungstransportuntersuchungen an nanofunktionalen Bauelementen mit Diodencharakteristik basierend auf funktionalisierten Nanopartikeln

N. Babajani (2015), iv, 138, XLVII

ISBN: 978-3-95806-026-5

Band / Volume 43

Transport and Noise Properties of Nanostructure Transistors for Biosensor Applications

J. Li (2015), vii, 175 pp

ISBN: 978-3-95806-034-0

Band / Volume 44

Quantitative scanning tunneling spectroscopy of non-polar III-V compound semiconductor surfaces

M. Schnedler (2015), 122 pp

ISBN: 978-3-95806-075-3

Band / Volume 45

Model-based Algorithm Development with Focus on Biosignal Processing

Y. Yao (2015), x, 169 pp

ISBN: 978-3-95806-080-7

Band / Volume 46

Growth and characterization of crystalline rare-earth based thin oxide films for the application as gate dielectric in nanotechnology

A. B. Schäfer (2015), xiii, 157 pp

ISBN: 978-3-95806-111-8

Band / Volume 47

TEM/STEM Investigations of Phase Change Materials for Non-volatile Memory Applications

M. Bornhöfft (2017), viii, 135 pp

ISBN: 978-3-95806-221-4

Information
Band / Volume 47
ISBN 978-3-95806-221-4

